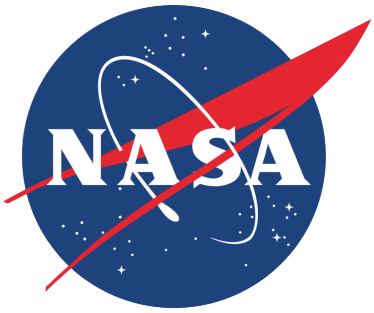

The Standard Definitions and Evaluation Team Final Report

A common comparison of exoplanet yield

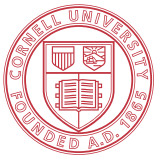

Cornell University

National Aeronautics and
Space Administration

Jet Propulsion Laboratory
California Institute of Technology
Pasadena, California

A portion of this research was carried out at the Jet Propulsion Laboratory, California Institute of Technology, under a contract with the National Aeronautics and Space Administration.

THE STANDARD DEFINITIONS AND EVALUATION TEAM FINAL REPORT: A COMMON COMPARISON OF EXOPLANET YIELD.

Authors

Rhonda Morgan (JPL[1])
Dmitry Savransky (Cornell University)
Chris Stark (Space Telescope Science Institute)
Eric Nielsen (Stanford University)

Contributors

Eric Cady (JPL[1])
Walker Dula (JPL[1])
Shannon Dulz (University of Notre Dame)
Andrew Horning (Cornell University)
Eric Mamajek (JPL[1])
Bertrand Mennesson (JPL[1])
Peter Plavchan (George Mason University)
Ty Robinson (Northern Arizona University)
Garreth Ruane (JPL[1])
Dan Sirbu (NASA Ames Research Center)
Gabriel J. Soto (Cornell University)
Michael Turmon (JPL[1])
Margaret Turnbull (SETI Institute)

Standard Definitions and Evaluation Team Members

Rhonda Morgan (JPL[1]), **Lead**
Dmitry Savransky (Cornell University)
Chris Stark (Space Telescope Science Institute)
Avi Mandell (NASA Goddard)
Ruslan Belikov (NASA Ames Research Center)
John Krist (JPL[1])
Eric Nielsen (Stanford University)

STDT Liasons

Courtney Dressing (Univsersity of California, Berkeley) LUVOIR
Karl Stapelfeldt (ExEP, JPL[1]) HabEx
Klaus Pontoppidan (Space Telescope Science Institute) OST [1]Jet Propulsion Laboratory, California Institute of Technology

Contents

1. PREFACE

Two of the four large mission concept studies for the Astrophysics Decadal Survey were designed to directly image and spectrally characterize earth-like exoplanets (HabEx[1] and LUVOIR[2]). In 2016, the Astrophysics Division chartered[3] an *Exoplanet Standard Definition and Evaluation Team* (ExSDET) for the purpose of providing an unbiased science yield analysis of the multiple large mission concepts using a transparent and documented set of common inputs, assumptions and methodologies. Over the course of the past three years, the ExSDET has responded to the direction provided in the charter and the required deliverables by performing the following tasks:

- Develop analysis tools that will allow quantification of the science metrics of the mission studies,
- Incorporate physics-based instrument models to evaluate both internal and external occulter designs,
- Establish the science metrics that define the yield criteria,
- Cross validate the various analytical methodologies and tools,
- Provide complete evaluations using common assumptions and inputs of the exoplanet yields for each mission concept.

2. INTRODUCTION

The primary goal of this report is to present our best understanding of the exoplanet imaging and characterization capabilities of the current STDT observatory and instrument designs, along with their nominal operating plans, using common input assumptions and analysis methodologies. This report is explicitly **not** intended to present an exploration of the capabilities of the full design spaces available to the various mission concepts. Such explorations are available elsewhere, most recently in the series of papers by Stark et al. (2016a, 2019, 2015). Similarly, this report does not explore the full extent of possible exoplanet science outcomes associated with different operating rules and decisions for a particular observatory and instrument design. Such studies are available in the literature (see, e.g., Savransky and Garrett, 2015). Rather, we seek only to present an unbiased estimation of science yield for these missions, using a clearly stated definition of this yield, clearly stated input assumptions, and multiple different modeling approaches in order to cross-validate our results.

This report is structured as follows:

- §3 (*Common Assumptions and Definitions*) provides the rationale for, and derivation of, the input parameters and assumptions necessary to feed the analytical models and decision logic of the tools. This consists of astrophysical parameters, input target lists, and instrument design parameters. It is noted where there are necessary differences in the input parameters for the two tools used (EXOSIMS and AYO) and the impact of those difference.
- §4 (*Yield Definition*) establishes the scientific metrics which define a successful detection and characterization observation and thereby what counts in the yield calculations.
- §5 (*Yield Modeling*) describes the two primary analysis tools used in calculating scientific yield, compares the approaches and discusses the pros and cons of each method. The two tools are the EXOSIMS program (based on Dmitri Savransky's open source tool initiated under the WFIRST Preparatory Science program) and the Altruistic Yield Optimization tool (AYO; developed by Chris Stark). It is noted that a significant effort under the ExSDET activity involved the development and maturation of the EXOSIMS tool and so specific treatment of its capabilities, specifically the schedulers, is provided here.
- §6 (*Results*) provides a summary of key results of end to end mission yield estimates for the various study configurations: LUVOIR B, HabEx coronagraph only ("HabEx 4C"), HabEx coronagraph plus starshade (hybrid; "HabEx 4H")), HabEx starshade only ("HabEx 4S"). The results allow a quantitative comparison between the yield estimates of each configuration for the different analytic tools as well as a comparison between the use of the various occulter designs. Various Appendices provide additional information.

[1] The HabEx final report can be accessed at: https://www.jpl.nasa.gov/habex/.

[2] The LUVOIR final report can be accessed at: https://asd.gsfc.nasa.gov/luvoir/reports/.

[3] The full charter, purpose and deliverables for the ExSDET can be found at https://exoplanets.nasa.gov/system/internal_resources/details/original/562_ExSDET_Charter.pdf.

• Appendix A allows the reader to dive deeper into the comparison between the approaches and results from the two tools.

• Appendix B provides supplemental parameters of the input target star lists.

• Appendix C discusses the exoplanet case for Origins Space Telescope (OST)[4], another large Decadal mission study, and why the yield calculation/comparison is not applicable to this mission concept.

3. COMMON ASSUMPTIONS AND DEFINITIONS

3.a. **Astrophysical parameters.**

3.a.i. *The SAG13 and Dulz/Plavchan Planet Population.*

3.a.i.1. **SAG13.** NASA's Exoplanet Program Analysis Group (ExoPAG) facilitated a science analysis group (SAG) denoted SAG13 to determine the occurrence rates to use for exoplanet yield modeling. SAG13 performed a meta-analysis on occurrence data and models from peer reviewed papers and the 2015 Kepler "hack week." SAG13 placed the occurrence rates on a common grid of planet radius and period, calculated the mean and standard deviation of the crowd-sourced occurrence rates, and fit a broken power law model to the mean occurrence rates over the grid. Piece-wise power law coefficients were also fit to the $+1\sigma$ "optimistic" and -1σ "pessimistic" cases. These do not represent a formal mean and standard deviation of the occurrence rates, but rather express the state of knowledge and disagreement (more formally, epistemic uncertainty) regarding the occurrence rates in the community. The SAG13 process and results are detailed in Belikov et al. (2016) and Kopparapu et al. (2018). The SAG13 occurrence rate model is a function of the log of planet radius R and the log of period P:

$$\frac{\partial^2 N(R,P)}{\partial \ln R \, \partial \ln P} = \Gamma_i R^{\alpha_i} P^{\beta_i} , \quad (1)$$

The power law break at $3.4R_\oplus$ follows Burke et al. (2015). The coefficients are given in Table 1.

The SAG13 power law model forms the basis of the ExSDET occurrence rates. However, the validity region for the SAG13 model does not extend to periods that are much greater than the limits of the Kepler data, such as small planets on orbits of many hundreds of days. Extrapolating the SAG13 model to those periods leads to what appears to be higher occurrence rate than is currently observed from, e.g., direct imaging surveys. Therefore, Dulz et al. (2019, *in prep.*) modified the SAG13 occurrence rates in the region of extrapolation beyond the SAG13 Kepler grid. We present here a summary of their work.

TABLE 1. *Coefficients for the nominal, optimistic, and pessimistic SAG13 piece-wise power law occurrence rate models above and below the break at* $3.4R_\oplus$.

Coefficient	Optimistic	Nominal	Pessimistic
$\Gamma(< 3.4R_\oplus)$	0.138	0.38	1.06
$\alpha(< 3.4R_\oplus)$	0.277	−0.19	−0.68
$\beta(< 3.4R_\oplus)$	0.204	0.26	0.32
$\Gamma(> 3.4R_\oplus)$	0.72	0.73	0.78
$\alpha(> 3.4R_\oplus)$	−1.56	−1.18	−0.82
$\beta(> 3.4R_\oplus)$	0.51	0.59	0.67

3.a.i.2. **Inputs.** SAG13 occurrence rates are limited based on Kepler sensitivity to planets of 640 days orbital period or less. Due to a lack studies which cover relatively small planets at longer orbital periods for solar-type stars, one can extrapolate the SAG13 power law to much longer orbital periods; however, this produces an unreasonably high amount of planets at the Radius break point at long periods (Cold Neptunes). As a correction for this, Dulz et al. (2019, *in prep.*) introduced an occurrence rate limit at large semi-major axes based on the long term stability of planets generated.

Additionally the Dulz et al. (2019, *in prep.*) occurrence rates differ from SAG13 in the treatment of Jupiters. Three options were investigated for the Jupiter distribution: using SAG13 only, applying a combination of Bryan 2016 and Cumming 2008, and applying the Fernandes et al. 2019 two-part power law.

Bryan et al. (2016) derived an occurrence rate power law for additional cold Jupiters in known exoplanet systems detected with a NIRC2 RV survey. While Bryan et al. derived several occurrence rates for different mass-semimajor axis ranges, Dulz et al. (2019, *in prep.*) analyzed the power law valid for $0.5 - 13 M_{Jup}$ and $5 - 50$ AU. This occurrence rate was extended down to apply for Jupiters $M_p > 0.225 M_{Jup}$ at $a > 5$ AU. Cumming et al. 2008, based on Keck Planet Search radial velocity data, derived an occurrence rate of Jupiters valid for $0.3 - 10 M_{Jup}$ and $P < 2000$ days. Dulz et al. (2019,

[4]The final report for the Origins Space Telescope can be accessed at: https://asd.gsfc.nasa.gov/firs/.

in prep.) extended this power law in both mass and semimajor axis space to cover $M_p > 0.225 M_{Jup}$ and $a < 5$ AU.

Fernandes et al. (2019a), a meta-analysis of Kepler and RV studies, found a turnover in RV Jupiters occurrence rates at the snow line. Fernandes et al. (2019a) derived a two part power law model from several methods, one of which was the Exoplanet Population Observation Simulator (EPOS) which had asymmetric results with a turnover at 2075 days and was valid for $0.1 - 20 M_{Jup}$ and $0.1 - 100$ AU. Dulz et al. (2019, *in prep.*) used the EPOS derived model for $M_p > 0.225 M_{Jup}$.

3.a.i.3. **Methods.** SAG13, originally formulated in Radius/Period parameter space, was translated to Mass/Semi-major axis space using the Mass-Radius relation of Chen and Kipping (2016). This mass radius relation was broken into 4 regions: Terran, Neptunian, Jovian, and Stellar worlds. Due to the negative exponent on the mass-radius relation for Jovian worlds, there was a degeneracy for the mass of planets between $11.3 - 14.3 R_\oplus$. For this reason, when translating radius to mass Dulz et al. (2019, *in prep.*) used the Neptunian power law to cover all SAG13 regions beyond the Terran-Neptune divide.

To avoid this degeneracy for the two additional Jupiter distributions, Dulz et al. (2019, *in prep.*) applied SAG13 rates only up to $0.225 M_{Jup} = 10 R_\odot$ and used the RV-derived rates of Bryan et al. (2016) and Cumming et al. (2008) or Fernandes et al. (2019a) above $0.225 M_{Jup}$. Figure 1 compares the Jupiter occurrence rates as a function of semi-major axis for these variations with SAG13 nominal rates. After comparison of these occurrence rates, Dulz et al. (2019, *in prep.*) chose to utilize the Fernandes et al. (2019a) distribution which covers a wide range of planetary parameters.

From an occurrence rate distribution over the entire parameter space, Dulz et al. (2019, *in prep.*) drew randomly from this continuous distribution via inverse transform sampling to create a set of synthetic systems for 100,000 stars of 1 solar mass.

For each star, the long term stability of each planet pair was determined based on the Hill radius separation criteria of Kane et al. (2016); in any unstable pairs, the more massive planet was kept. If the initial stability check resulted in the removal of any planets within 0.5 AU, where Kepler occurrence rates were solidly reliable, the entire system was redrawn for that star until the stability condition was met. The planets for all 100,000 stars form the "initial" occurrence rates. Some of the planets outside of 0.5 AU were unstable.

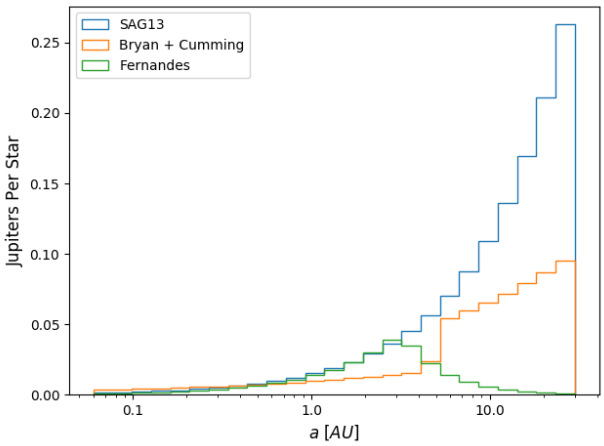

Figure 1. *A comparison of the number of Jupiters ($M_P > 0.225\, M_{Jup}$) from SAG13, a combination of Bryan et al. (2016), Cumming et al. (2008), and Fernandes et al. (2019b).*

A "maximally packed" planet population was also computed. Starting with the "initial" population, all unstable planets were removed. Then an entire new set of planets were drawn for the parameter space outside of the 0.5 AU trusted region. The only retained planets were those which were stable with both the stable "initial" planets and any planets previously found stable from this "maximally packed" procedure. Then planets were randomly drawn again in the same fashion. This process was repeated 175 times, to the limit at which the last draw would add another stable planet for less than 1% of the systems for optimistic, nominal and pessimistic cases. At the end of this process, the distribution for these planets formed the "maximally packed" planet population.

Finally, to limit edge effects resulting from definite semi-major axis bounds which resulted in a high count due to a lack of planets outside 35 AU, planets at further than 30 AU were removed from both the "initial" and "maximally packed" populations. For all planets, the radius was calculated based on the Chen and Kipping (2017) mass relation. Because there is no degeneracy in translating mass to radius, all three planet type regions of Chen and Kipping (2017) were used. For both "initial" and "maximally packed" populations, the occurrence rate histograms were calculated as the total number of

planets in each cell of a 25x25 grid, evenly spaced in log(radius)-log(period) space, divided by the 100,000 stars in the simulation ensemble.

The occurrence distributions for the "initial" and "maximally packed" populations are shown in Figure 2. For the nominal and optimistic cases, the "initial" populations greatly exceed the "maximally packed" populations at large semi-major axis. For the pessimistic case, the "initial" population never exceeded the "maximally packed" population. The point at which maximal packing was exceeded also depends on radius. The final occurrence rate was determined by taking the cell-by-cell minimum of the "initial" and "maximally packed" populations. The result was a set of occurrence rates consistent with SAG13 except in the regions where the population would become nonphysically over-packed which were then replaced by the maximum possible occurrence rate.

3.a.i.4. **Results.** Figure 3 shows the occurrence rates, as a function of radius and period, of a combination of SAG13 (optimistic, nominal and pessimistic) with Fernandes et al. (2019a) occurrence rates constrained by long-term dynamic stability. These were implemented in EXOSIMS and available at https://github.com/dsavransky/EXOSIMS/tree/master/EXOSIMS/PlanetPopulation.

Table 2 compares the SAG13 model to the Dulz et al. (2019, *in prep.*) occurrence rates, binned according to the planet types defined in Kopparapu et al. (2018) (described in the next section). For some planet types, the optimistic case produced a lower occurrence rate than the nominal case. For example, the optimistic case predicted 1.19 cold sub-Neptunes per star while the nominal case predicted 1.38 cold sub-Neptunes per star. In the nominal case, occurrence rates of cold Jovians and sub-Jovians were higher than the optimistic case, and the higher occurrence rates of cold Jovians and sub-Jovians ejected sub-Neptunes under the dynamic stability criteria at a higher rate than the optimistic case.

In most cases, the nominal occurrence rates were comparable to those calculated directly from the SAG13 model. In the region of the original SAG13 analysis, the SAG13 model was preserved. However, for cold planets, the nominal occurrence rates were lower than the SAG13 model because occurrence rates were constrained by dynamic stability. This dynamic stability provided a reasonable theoretical

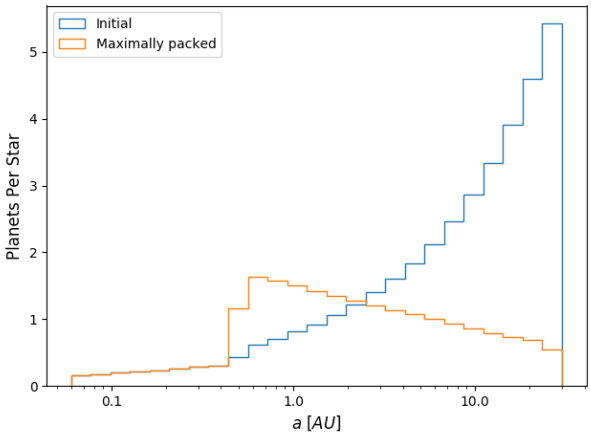

(a) *Optimistic*

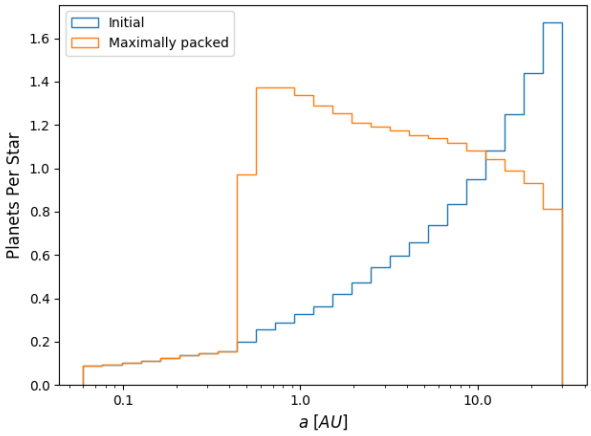

(b) *Nominal*

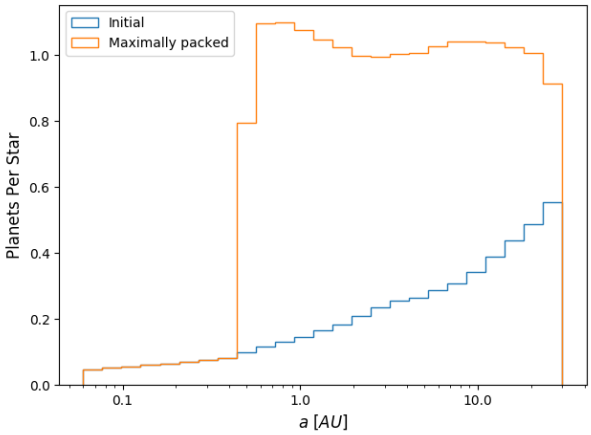

(c) *Pessimistic*

FIGURE 2. *Distribution summed over Mass ($0.08M_{\oplus} - 15M_{Jup}$) of "Initial" and "Maximally packed" populations for Optimistic, Nominal, Pessimistic SAG13 combined with Fernandes et al. (2019b)*

constraint to the occurrence rates in the extrapolated regions of the SAG13 model.

3.a.ii. *Planet Bins.* While the distribution of exoplanets is a continuous function of radius and period, when *reporting* exoplanet yields, it is convenient to categorize the exoplanets. For this reason, the ExSDET adopted the planet categorization scheme of Kopparapu et al., 2018, in which exoplanets are divided into 5 radius bins ("rocky planets" from 0.5–1.0 $R_\oplus$, "Super Earths" from 1.0–1.75 $R_\oplus$, "sub-Neptunes" from 1.75–3.5 $R_\oplus$, "Neptunes" from 3.5–6 $R_\oplus$, and "Jupiters" from 6–14.3 $R_\oplus$), and 3 temperature bins ("hot," "warm," and "cold") defined by the condensation temperatures of ZnS, H_2O, CO_2, and CH_4. Figure 4 shows this 5×3 grid of planet types. The occurrence rate of each planet type is shown, together with the range of uncertainty given by the optimistic and pessimistic cases, all calculated by integrating the continuous occurrence rates of Dulz et al. (2019, *in prep.*) over each bin. Each planet type was assigned a geometric albedo (shown in Figure 4) and a Lambertian scattering phase function. All planets were assumed to be on circular orbits. The semi-major axis boundaries that define the temperature bins of each planet type are assumed to scale with the bolometric stellar insolation; that is, they scale with the square root of the bolometric stellar luminosity.

The green outline in Figure 4 shows the adopted definition of an exo-earth candidate. Exo-earth candidates are assumed to be on circular orbits and to reside within the conservative HZ, spanning 0.95–1.67 AU for a solar twin (Kopparapu et al., 2013). Exo-earth candidates span radii ranging from $0.8a^{-0.5}$ to 1.4 $R_\oplus$, where a is the semi-major axis for a solar twin. The lower radius limit comes from an empirical atmospheric loss relationship derived from solar system bodies (Zahnle and Catling, 2017). The upper limit on planet radius is a conservative interpretation of an empirically-measured transition between rocky and gaseous planets at smaller semi-major axes (Rogers, 2015). All exo-Earth candidates were assigned Earth's visible geometric albedo of 0.2, assumed to be wavelength-independent.

3.a.iii. *Binary Stars and Close Companions.* Detecting exoplanets in binary star systems presents additional challenges. Light from companion stars outside of the coronagraph's field of view, but within that of the telescope, will diffract off of particulate contaminants and surface figure errors

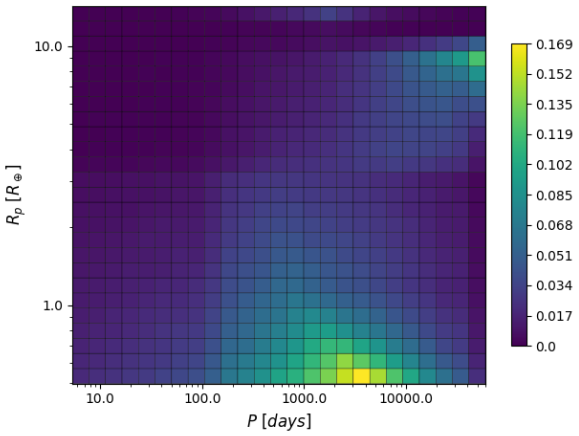

(a) *Optimistic*

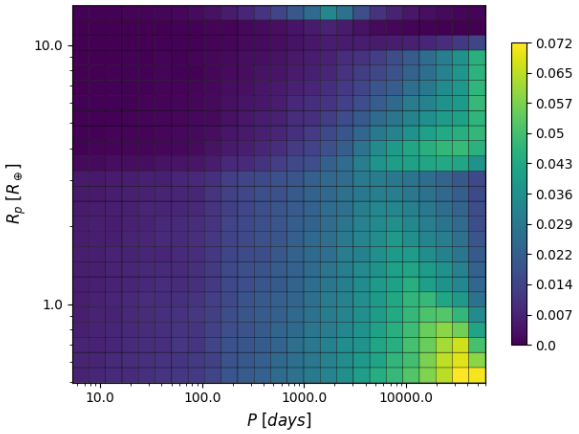

(b) *Nominal*

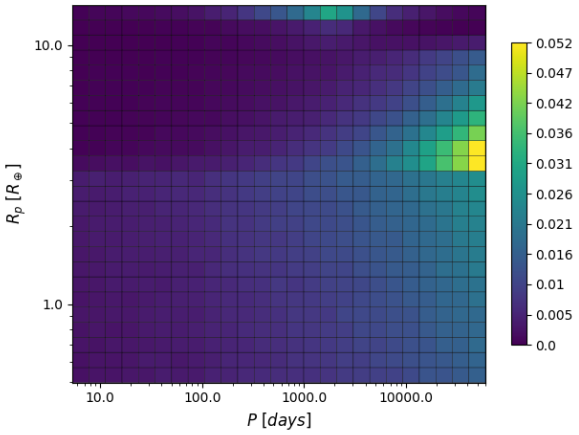

(c) *Pessimistic*

FIGURE 3. *Final occurrence rates with Fernandes et al. (2019b) and SAG13 distributions constrained by dynamic stability. The color scale, which varies between the cases, indicates planets per star.*

Table 2. *A comparison of SDET occurrence rate distributions with Kopparapu et al. 2018 planet type definitions and η_{planet} SAG13 nominal occurrence rates. Earthlike planets use limits of $0.95 < a < 1.67$ AU and $0.8/\sqrt{a} < R_p < 1.4R_\oplus$.*

Planet Type	SAG13	Optimistic	Nominal	Pessimistic
Hot rocky	0.67	1.82	0.64	0.22
Warm rocky	0.30	1.07	0.31	0.09
Cold rocky	1.92	3.80	1.89	0.50
Hot super-Earths	0.47	0.88	0.43	0.21
Warm super-Earths	0.21	0.56	0.22	0.09
Cold super-Earths	1.42	1.36	1.33	0.51
Hot sub-Neptunes	0.48	0.66	0.44	0.28
Warm sub-Neptunes	0.22	0.41	0.23	0.12
Cold sub-Neptunes	1.63	1.19	1.38	0.78
Hot sub-Jovians	0.07	0.10	0.07	0.05
Warm sub-Jovians	0.07	0.13	0.07	0.04
Cold sub-Jovians	1.35	1.14	1.06	0.58
Hot Jovians	0.056	0.07	0.06	0.05
Warm Jovians	0.053	0.13	0.08	0.06
Cold Jovians	1.01	1.48	0.85	0.45
Earth	0.24*	0.71	0.24	0.09

*Not included inKopparapu et al. (2018), but calculated based on earthlike limits using original SAG13 nominal power law.

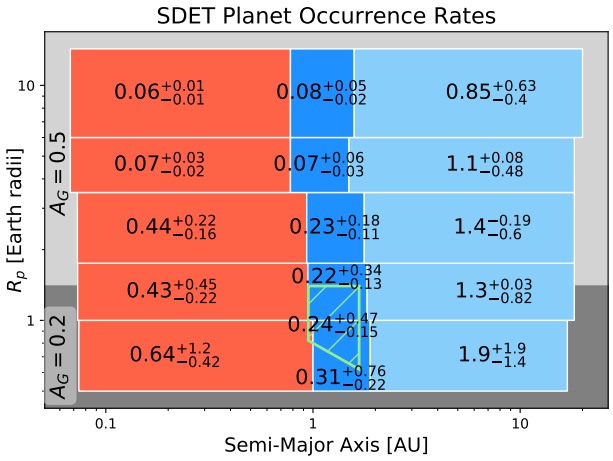

Figure 4. *Adopted planet classification scheme, per-class occurrence rates η, and their ranges. Geometric albedos, A_G, shown in background.*

on the primary and secondary mirrors. Some of this stray light is scattered into the coronagraph's field of view. For some binary systems, this stray light can become brighter than an exo-earth.

The stray light from binary stars in the final image plane was estimated and included as a noise source in exposure time calculations. The numerical stray light models of Sirbu et al. (in prep) were utilized. These models predict the power in the wings of the point spread function (PSF) at large separations assuming a $\lambda/20$ RMS surface roughness and an f^{-3} envelope, where f is the spatial frequency of optical aberrations/contamination. Stray light was assumed to be measurable or modelable, such that it could be subtracted off and contributed only Poisson noise. It should be noted that including the full amount of light scattered by the companion is actually conservative, as the companion scattered starlight could be actively reduced with multi-star wavefront control coronagraphic techniques (Belikov et al., 2017; Sirbu et al., 2018, 2017; Thomas, Belikov, and Bendek, 2015).

3.a.iii.1. **AYO.** When implementing the stray light model, the AYO yield code makes no artificial cuts to the target list based on binarity. The benefit-to-cost optimization in the AYO yield code determined whether or not stray light noise made a target unobservable. In practice, the AYO prioritization does reject a number of binary systems with contrast ratios close to unity and/or close separations.

3.a.iii.2. **EXOSIMS.** In EXOSIMS, the binary leak model is implemented via a pre-computed table of stary light contribution as a function of companion angular separation. For a particular target, the locations of the closest and brightest binaries are queried (as described in §3.b.i). In cases where the returned values are the same, it is assumed that they are describing the same source, and one of the entries is dropped. The input table is interpolated to the angular separation of the target companion stars. A

binary leak term is evaluated as the sum of the contributions of the closest and brightest companion stars, and this term is then added to the overall background flux term containing the zodi and exozodi contribution and the speckle residuals.

3.a.iv. *Zodiacal Light.* The solar system's zodiacal brightness varies with wavelength and the telescope's pointing; the closer one observes toward the Sun, the brighter the zodiacal cloud will appear. Zodiacal cloud brightness was estimated as a function of wavelength and ecliptic latitude and longitude by interpolating the tables of Leinert et al. (1998). EXOSIMS specifically schedules each observation, enabling it to compute the zodiacal brightness based on the target's ecliptic coordinates on the date of the observation. Because AYO does not directly schedule any observation, reasonable assumptions were made for the solar elongation of each target at the time of observation. AYO calculations adopted a solar elongation of 135° and 60° for the coronagraph and starshade instruments, respectively (consistent with their instantaneous fields of regard). AYO calculations then translated this solar elongation into an ecliptic latitude and longitude given the target star's equatorial coordinates, and adopted the corresponding zodiacal brightness.

3.a.v. *Exozodiacal Light.* The exozodiacal light level used in the yield simulations were taken from the recent results of the Large Binocular Telescope Interferometer (LBTI) survey of exozodiacal dust. This section discusses the survey approach, the data reduction method, and the resulting distribution of exozodiacal dust. Then the implementation of the exozodiacal light model in the yield codes is discussed.

3.a.v.1. **LBTI HOSTS Survey.** Observations for the HOSTS (Hunt for Observable Signatures of Terrestrial Systems) survey for warm dust around nearby stars (exozodiacal dust, i.e., dust in and near their habitable zones, HZs) were completed in the first half of 2018 (during observing semester 2018A). The goal of HOSTS was to constrain the occurrence rate and typical level of exozodiacal dust around a sample of nearby stars in order to assess the risk imposed by this dust to future space missions attempting to directly image habitable exoplanets. The HOSTS Report contains the immediate conclusions of the survey relevant to this goal (Ertal2018Report, 2018).

Detailed descriptions of the HOSTS observing strategy, data reduction, and analysis, together with detailed statistical results, were provided by Ertel et al. (2018). The HOSTS Report and this section provide only a brief summary of these points and updates where necessary. In particular, the Report provides the final null measurements and derived HZ dust levels (zodi levels) for all observed stars and final statistics derived from those measurements.

The observations were carried out with the Large Binocular Telescope Interferometer (LBTI). The HOSTS team used nulling interferometry in the N band to combine the two 8.4-m apertures, to suppress the light from the central star, and to reveal faint, circumstellar emission. The total flux transmitted in nulling mode was measured and calibrated using a photometric observation of the target star. Nodding was used to subtract the variable telescope and sky background. Each observation of a science target (SCI) was paired with an identical observation of a reference star (CAL) to determine the instrumental null depth (nulling transfer function, the instrumental response to a point source) and calibrate the science observations. Data reduction followed the strategy outlined by Defrère et al. (2016) with minor updates as described by Ertel et al. (2018).

The basic detection statistics for different subsamples of targets are summarized in Table 3. The HOSTS team found higher detection rates for stars with cold dust (dusty stars) compared to stars without (clean stars). For early type stars this correlation is strong, but the small number of dusty Sun-like stars in the HOSTS sample prohibits a definite conclusion. Such stars are relatively rare and observing them was not a priority of the HOSTS survey as stars with known cold dust are unlikely to be first choice targets for future exo-Earth imaging missions.

TABLE 3. *Subsamples, excess detections, and occurrence rates.*

	Cold dust	Clean	All
Early type	5 of 6 83^{+6}_{-23}%	1 of 9 11^{+18}_{-4}%	6 of 15 40^{+13}_{-11}%
Sun-like	1 of 2 50^{+25}_{-25}%	3 of 20 15^{+11}_{-5}%	4 of 23 17^{+10}_{-5}%
All	6 of 8 75^{+9}_{-19}%	4 of 29 13^{+9}_{-4}%	10 of 38 26^{+8}_{-6}%

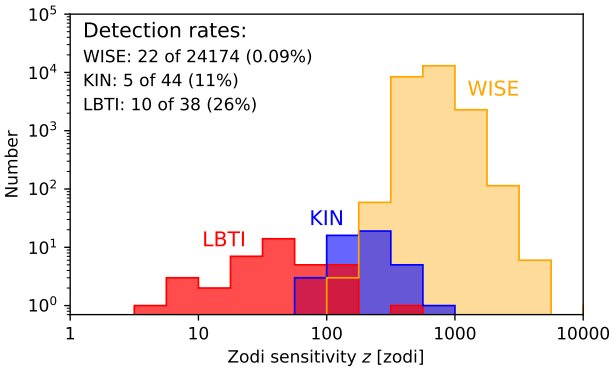

FIGURE 5. *Sensitivity of the HOSTS survey compared to previous surveys.*

Figure 5 compares the zodi sensitivities (1σ accuracy of the measurements) reached by the HOSTS survey to those of previous surveys, specifically the photometric measurements from WISE (Kennedy and Wyatt, 2013) and the Keck Interferometer Nuller (KIN; Mennesson et al. 2014). The shown HOSTS sensitivity is about a factor of five better than that of KIN for the observed samples; for the best targets, HOSTS has detected HZ dust levels that are a few times higher than in our Solar system.

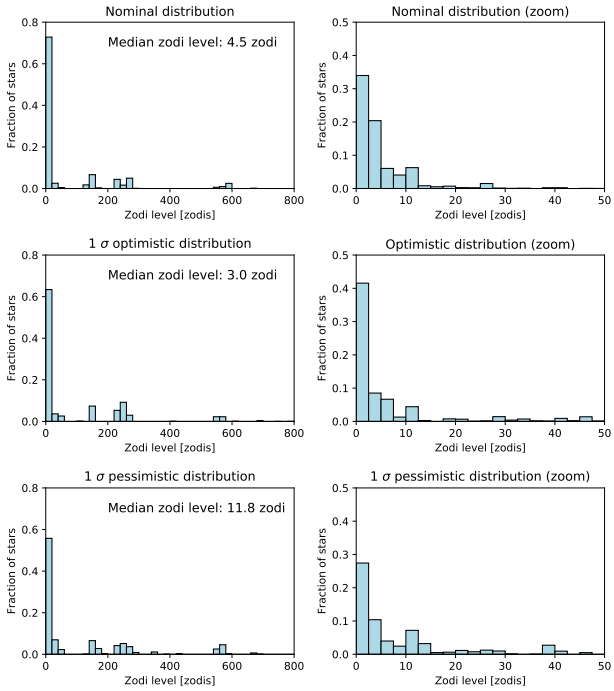

FIGURE 6. *Nominal, optimistic (low median, $m - \sigma_{lower}$), and pessimistic (high median, $m + \sigma_{upper}$) free form fits to the HOSTS data for Sun-like stars.*

3.a.v.2. **Sample constraints on habitable zone dust levels.** In addition to the basic statistics described in the previous section, the HOSTS team carried out a detailed statistical analysis to determine the typical HZ dust level for Sun-like stars. The HOSTS team followed the strategy described by Mennesson et al. (2014) and Ertel et al. (2018). In their previous analysis of an early subset of HOSTS observations, they assumed a log-normal probability distribution of the zodi level of a given star (luminosity function) and fitted it to their zodi measurements for different subsamples of stars to determine the median zodi levels of these samples and its uncertainties. They found that: (1) a lognormal luminosity function appears inadequate to reproduce well the observed distribution of excesses, instead a bimodal luminosity function is more likely in which most stars have low zodi levels and a few 'outliers' have relatively high levels; and (2) within the statistical uncertainties, the difference between stars with and without cold dust seen for early-type stars cannot be confirmed nor ruled out for Sun-like stars. The former is further supported by the complete HOSTS survey data, while the latter remains valid. Thus, the HOSTS team did not distinguish between dusty and clean Sun-like stars and use the 'free-form' iterative maximum likelihood algorithm described by Mennesson et al. (2014) instead of a lognormal luminosity function.

For the free-form method, the explored zodi levels are binned and the unknown luminosity function is parameterized through the probability that a given star has a zodi level in each of the bins. For the HOSTS analysis, the team selected bins of equal width of 1 zodi ranging from 0 zodis to 2000 zodis, an upper limit consistent with the LBTI measurements of Sun-like stars. The probability in each bin was then adjusted iteratively to maximize the likelihood of observing the data (Mennesson et al. 2014, Section 4.6). The median zodi level m was used to characterize the distribution. To determine the uncertainty of the derived distribution, the team randomly disturbed this 'nominal' distribution, creating 10^5 new distributions with small deviations from the nominal one. The likelihood of observing the data was computed for each of these distributions, and the profile likelihood theorem was then used to derive 1σ confidence intervals on m from its distribution among them. A median zodi level of Sun-like stars of $m = 4.5^{+7.3}_{-1.5}$ zodis was found. The nominal and 1σ optimistic (low median, $m - \sigma_{\rm lower}$) and pessimistic (high median, $m + \sigma_{\rm upper}$) free-form distributions are

shown in Figure 6. These statistics were adopted by the HabEx and LUVOIR mission study teams.

3.a.v.3. **Implementation in Yield Models.** Following Savransky, Kasdin, and Cady (2010), EXOSIMS models the contribution of exozodiacal light as $\mu f\,(\pi/2 - I)\,2.5^{M_\odot - M_s}/r^2$ where μ is the assumed number of exozodi in units of zodi, I is the target system inclination, r is the planet-star separation distance, and M_s is the absolute magnitude of the target star in the relevant observing band. The function f is the empirically derived variation of zodiacal light with viewing angle given by

$$f(\theta) = 2.44 - 0.0403\theta + 0.000269\theta^2 \quad (2)$$

with θ in degrees, in the range [0,90] (and is mirrored for $\theta \in [90, 180]$; D. Lindler, Personal Communication, 2008). This expression evaluates to a scaling factor that can be applied to the mean flux of the local zodi (typically given in magnitudes per square arcsecond), resulting in the total exozodiacal light flux. The inverse r^2 factor accounts for the decreasing exozodi contribution with planet separation, as discussed in Stark et al. (2014).

3.a.vi. *Orbit Determination.* Once a planet is detected by a space telescope, characterizing the planet requires an accurate assessment of the planet's orbit. Most immediately interesting are semi-major axis and eccentricity, which set what fraction of a planet's orbit it spends in the habitable zone. Additionally, models of reflected light spectra (Batalha et al., 2019) are given as a function of separation and phase angle, and so the full set of orbital parameters allows for directly determining the orientation of the star and planet in 3D space. Thus by observing the system at a variety of phase angles these models can be directly tested against data. Without precursor information such as RVs, the orbit must be determined from the astrometry measured by the spacecraft itself. The missions will measure relative astrometry, separation and position angle of the planet relative to the host star, as a function of time, at a series of discrete epochs. Such a visual orbit directly measures the orbital parameters semi-major axis, period, eccentricity, inclination angle, and epoch of periastron passage, as well as two parameters with a 180° ambiguity: position angle of nodes and argument of periastron.

The line of nodes can be directly measured from a visual orbit, with the planet and star at equal distances from the observer at the two nodes, the planet being further than the star as it moves from the ascending to the descending node, and closer than the star from the descending to ascending node. A visual orbit by itself, however, cannot differentiate the two nodes, and additional information, such as radial velocities, is needed to break this degeneracy. In the case of reflected light observations the degeneracy should be relatively easy to resolve, since the planet should be significantly brighter after passing the ascending nodes compared to before.

We determine the expected precision of orbital parameters as a function of number of revisits by simulating relative astrometry datasets from space telescopes, and then fitting the orbit and noting how the posteriors narrow as more observations are acquired. This process is repeated for simulated planets with different input parameters and a variety of observing cadences. Astrometric measurements are assumed to have Gaussian noise with $\sigma = 5$ mas, with noise added to each measurement by drawing a random variable from such a Gaussian, and assuming 5 mas uncertainty on the resulting measurement when fitting the orbit. Planets are assumed undetectable if the true separation falls within the IWA, or if the planet lies below the contrast curve, which can happen as planets move into unfavorable orbital phases with minimal illumination of the planet's disk by the host star. Orbit fitting is done with the rejection sampling algorithm OFTI (Blunt et al., 2017), which, like MCMC, samples the posteriors of the orbital parameters, but does so more efficiently for orbits with limited data.

Figure 7 shows the result for such a simulation, with three simulated planets with identical orbital parameters (semi-major axis of 1 AU, period of 1 year, inclination angle of 30°, and distance of 10 pc), but varying eccentricity. Plotted are the 1-σ uncertainties on each parameter from the orbit fits, as more data are added to the orbit fit. For the highest eccentricity, the planet is within the IWA at the first epoch, but detectable at all other epochs. A general result from a variety of inclination angles and noise realizations is that 3–4 well-spaced observations (including the discovery epoch) are sufficient to recover semi-major axis, eccentricity, and inclination angle (Figure 7), as well as separation and phase angle for a particular epoch (Figure 8) to better than ∼10%. In some cases 10% precision is reached after only three observations, but others require four.

Observing cadence is also a factor, with poorly-sampled data increasing the number of epochs required to reach 10% precision. Too frequent

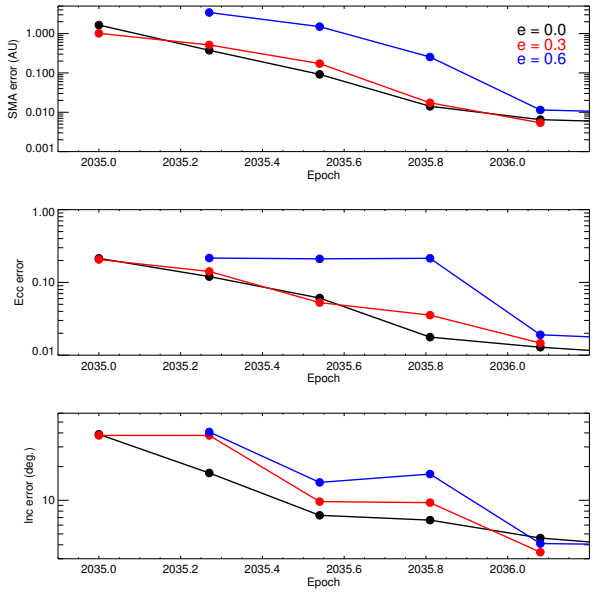

Figure 7. *Precision on orbital parameters as a function of time for simulated habitable zone planets as a variety of eccentricities, but with otherwise identical orbital parameters. Generally, better than 10% precision is reached on these parameters after four astrometric measurements with detections.*

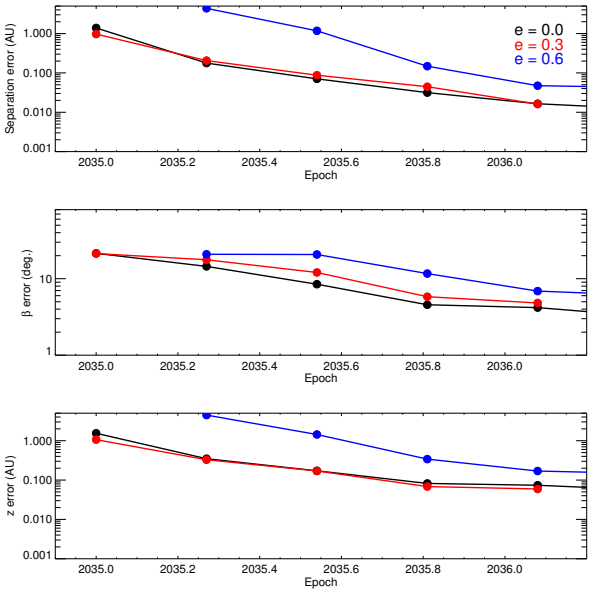

Figure 8. *Precision on separation, phase angle, and line-of-sight offset between star and planet for the discovery epoch as more data are taken. As with the orbital parameters, better than 10% precision is reached on these parameters after four astrometric measurements with detections.*

sampling results in a poorly-measured period, which is degenerate with other parameters. With enough of a gap between epochs, the period can be constrained along with the other parameters. Similarly, too long a gap runs the risk of sampling below the Nyquist limit, and again poorly constraining the period. We have found that spacing observations 2-6 months apart, for an exoplanet on a 1-year orbit, tends to recover orbital parameters with better than 10% precision after 3-4 observations.

Another study by Horning, Morgan, and Nielsen (2019) sought to determine the minimum number of observations required to determine the semi-major axis and eccentricity to 10% uncertainty. A rejection sampling algorithm was developed based purely on astrometry (no photometry) and applied to a test case of an Earth-Sun twin at 10 pc with 45° inclination. An astrometric uncertainty of 5 mas was assumed. A variety of observation cadences were attempted and it was found that the most efficient was uniform sampling over the orbit, for observation numbers from two to six per orbit. The simulation results for uniformly spaced observations over one orbit are shown in Figure 9. Two observations did not achieve 10% uncertainty, even for the most favorable phasing and only for the highly constraining priors. For three to six observations per orbit, the uncertainty on semi-major axis was below 10% after half an orbit. Observations spanning more than half the period of the planet is a critical condition for achieving uncertainty less than 10%. These results also show that three observations, evenly spaced, spanning more than a half a period, is the minimum number of observations to reach 10% uncertainty of the semi-major axis and eccentricity. Higher inclinations may require an additional observation.

The impact of phasing of the observations for three observations was also studied. Less than 10% uncertainty was achieved by all phasing of the uniformly spaced three observations. A sensitivity as low as 1.5% in semi-major axis and eccentricity could be achieved with optimal phasing.

Recently, Guimond and Cowan (2018) have undertaken a similar analysis, though with a slightly different set of instrument assumptions: astrometric precision of 3.5 mas instead of 5, and inner working angle of 31 mas, compared to the 51 mas we assumed earlier. We display their Figure 5c in Figure 10,

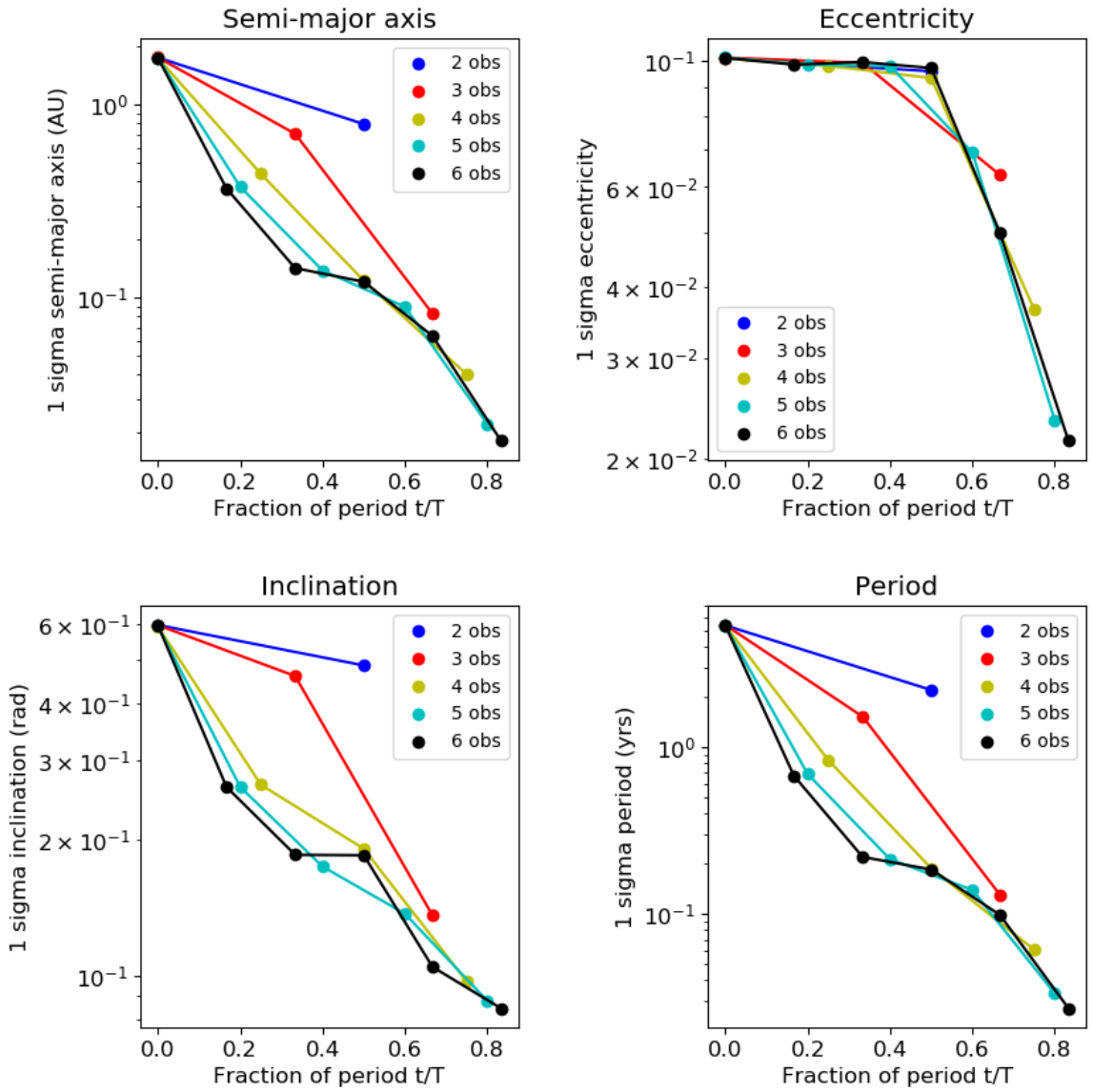

FIGURE 9. *A comparison of uncertainty in the orbital parameters for 2, 3, 4, 5, and 6 observations spaced equally over one period of an Earth-like orbit inclined at 45 degrees. This comparison uses only the astrometry data to infer orbital parameters (it does not incorporate photometry), does not have null observations, and the initial observation is taken at quadrature.*

showing precision on semi-major axis as a function of number of epochs. Their results for 1 and 2 epochs are obtained through a semi-analytic method, while 3 epochs and above are found from an MCMC orbit fit (Blunt et al. 2017 has shown that OFTI and MCMC produce identical posteriors for identical datasets and priors). Additionally, Guimond and Cowan (2018) explore a larger range of parameter space, drawing from six orbital parameters, while leaving distance set to 10 pc and mass to 1 $M_\odot$. Despite the differences in methods, we find generally consistent results: that 3 to 4 epochs result in better than 10% precision on recovered semi-major axis.

Guimond and Cowan (2018) find a greater likelihood of needing only 3 epochs to constrain semi-major axis if the underlying distribution of planet eccentricities favors small eccentricities, such as a beta distribution (Kipping, 2013) or linear with a negative slope (Nielsen et al., 2008). This is consistent with our finding that for an equal number of epochs, better orbital parameter precision is reached for planets on more circular orbits. Guimond and Cowan (2018) also explored the dependence on

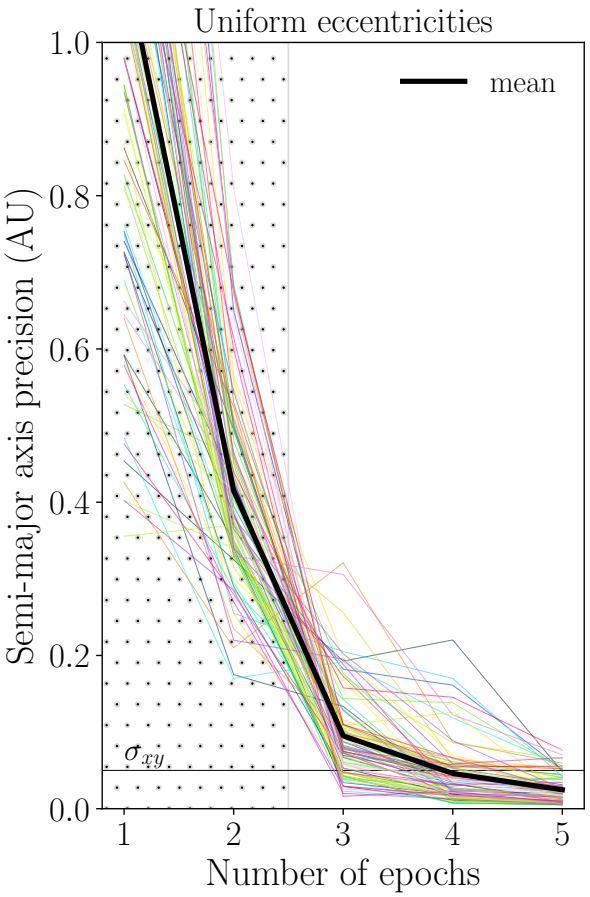

Figure 10. *Figure 5c of Guimond and Cowan (2018), giving the 1σ precision on semi-major axis measurements as a function of number of epochs for 100 simulated planets with varying orbital parameters.*

astrometric precision, and as expected the likelihood of needing a fourth epoch increases with decreasing astrometric precision.

Thus, the consensus result is that *the basic properties of a newly detected habitable zone planet can be characterized with 3–4 detections separated by 2–6 months.*

The effective implementation for each of the modeling codes was slightly different. For AYO, the number of required detection observations was 6 with the assumption that 4 would be successful and provide orbit determination. For EXOSIMS, the criteria was one of several that acted as a funnel to promote targets for characterization observations. For a target to be promoted for characterization, the planet had to have 1) three detections that spanned more than half the period of the planet or four detections, 2) be within the habitable zone, and have a radius fitting the definition of exo-earth candidate. Performing the successful detections implied that orbit fitting had been performed and the observer had knowledge of criteria (2).

3.b. **Input Target Catalog.** EXOSIMS and AYO use different input target list catalogs, a result of previous limitations and unavailability of catalog updates. While ideally all yield calculations would use a single, standardized target list, Stark et al. (2019) has demonstrated that the minor differences between target lists are inconsequential; target list differences result in yield differences at only the few percent level. This is due to the fact that the two target lists, while independently generated, depend heavily on the *Hipparcos* survey, and contain largely the same stars out to 30 pc, and due to the fact that the overall yield is robust to inaccuracies in individual stellar parameters when large numbers of stars are surveyed.

3.b.i. *EXOSIMS.* EXOSIMS uses the original ExoCat-1 catalog (Turnbull, 2015), as stored in the `MissionStars` table of the NASA Exoplanet Archive hosted by the NASA Exoplanet Science Institute[5]. Missing photometric information for targets is optionally synthesized by interpolating over Eric Mamajek's Mean Dwarf Stellar Color and Effective Temperature Sequence (Mamajek, 2019). Information is filled in with the following order of precedence:

(1) Any instances of missing V band apparent magnitudes where the target spectral type can be identified and is a dwarf type are filled by interpolation of the cataloged mean V magnitudes over the spectral subtype.
(2) Any instances of missing B band apparent magnitudes where the target spectral type can be identified and is a dwarf type are filled by interpolation of the cataloged mean B-V colors over the spectral subtype, which are added to the V magnitude.
(3) Any instances of missing stellar luminosities where the target spectral type can be identified and is a dwarf type are filled by interpolation of the cataloged mean luminosities over the spectral subtype.
(4) Any instances of missing bolometric corrections where the target spectral type can be

[5] https://exoplanetarchive.ipac.caltech.edu/docs/data.html

identified and is a dwarf type are filled by interpolation of the cataloged mean bolometric corrections over the spectral subtype.

(5) Any instances of missing K, H, J, I, U, or R magnitudes where the target spectral type can be identified and is a dwarf type are filled by interpolation of the cataloged mean H-K, J-H, V-I, U-B, and V-R colors, respectively, over the spectral subtype, and addition to the K, H, J, V, B, and V magnitudes, respectively.

ExoCat-1 is further modified in the case when the binary leakage model is being used with updated information from the Washington Double-Star catalog, maintained at the U.S. Naval Observatory. Stars from ExoCat are cross-referenced by their Hipparcos identifiers and four additional columns are added to the input catalog:

(1) The separation (in arcseconds) of the closest companion to each target
(2) The Δ magnitude in V band of the closest companion to each target
(3) The separation (in arcseconds) of the brightest companion to each target
(4) The Δ magnitude in V band of the brightest companion to each target

In certain instances, the closest and brightest companions are the same star, in which case the latter data set is omitted.

3.b.ii. *AYO.* AYO uses an input star catalog compiled following the methods of Stark et al. (2019). Briefly, the target list is equivalent to the union of the Hipparcos New Reduction catalog and the Gaia TGAS catalog. For each star, the catalog adopts the most recent measured parallax value from the Hipparcos, Gaia TGAS, and GAIA DR2 catalogs, then down-selected to stars within 50 pc. BVI photometry and spectral types were obtained from the Hipparcos catalog. Additional bands and missing spectral types were supplemented using SIMBAD. All stars identified as luminosity class I-III were filtered out, leaving only main sequence stars, sub-giants, and few unclassified luminosity classes. Binary parameters were retrieved from the Washington Double Star catalog, which was cross-referenced with the catalog via SIMBAD. We note that while the AYO input catalog extends to 50 pc, not even the LUVOIR A concept observes habitable zones beyond 30 pc.

3.c. **Summary of Astrophysical Parameters.** The preceding discussion of astrophysical assumptions and inputs is summarized in Table 4.

3.d. **Instrument Parameters.** The instrument parameters for the baseline HabEx and LUVOIR B architectures analyzed are summarized in Table 5.

We briefly describe what assumptions are made regarding the raw contrast floor for both architectures. Planet yields are estimated using the raw contrast performance predicted by modeling simulations of the coronagraph optics. For HabEx, the contrast performance was predicted by end-to-end structural thermal optical performance ("STOP") models for both the coronagraph and starshade instruments. For LUVOIR Architecture B, the coronagraph performance was modeled using an ideal optical state of the telescope optics, including the segmented primary mirror. To account for possible modeling residual uncertainties and physical wavefront residuals, the raw contrast adopted at a given separation is always defined conservatively as the worst of two values: the model predicted performance at that location and some constant "raw contrast floor," defined as the best instrument contrast reachable at any separation from the star. AYO found HabEx EEC yield to be fairly insensitive to the raw contrast floor as long as its value remains of the order of 10^{-10}. Both AYO and EXOSIMS use the raw contrast floor.

It is worth noting that the raw contrast is an instrumental performance parameter. It is different from the minimum planet-to-star flux ratio detectable, which can be significantly lower than the instrument raw contrast, as illustrated by the ground-based detections of exoplanets significantly fainter than residual starlight speckles using advanced post-processing techniques e.g. Lafreniere et al., 2007; Soummer, Pueyo, and Larkin, 2012.

4. Yield Definition

The desired end product of the direct imaging of exoearth candidates is not only their discovery, not only determination if they are in the habitable zone, but a full spectra to reveal biomarkers. A starshade and coronagraph arrive at a full spectra in very different ways and consequently the observing scenarios to narrow the targets to candidates for full spectral characterization are different. Furthermore, the two yield codes implement the observing scenarios with very different approaches, so metrics that are available explicitly in EXOSIMS may be implicit in AYO. Four spectral characterization metrics are evaluated to provide various levels of fidelity of the

Table 4. *Adopted Astrophysical Parameters*

Parameter	AYO	EXOSIMS	Description
$\eta_\oplus$	0.24	SAG13 power law	Fraction of sunlike stars with an exo-Earth candidate
R_p	$[0.6, 1.4]R_\oplus$		Exo-earth candidate planet radius[a]
a	[0.95, 1.67]AU		Semi-major axis for solar twin
e	0		Eccentricity (circular orbits)
$\cos i$	$[-1, 1]$		Cosine of inclination (uniform distribution)
ω	$[0, 2\pi]$		Argument of pericenter (uniform distribution)
M	$[0, 2\pi]$		Mean anomaly (uniform distribution)
Φ	Lambertian		Phase function
A_G	0.2		Geometric albedo of rocky planets
A_G	0.5		Geometric albedo of gas planets
z_c	23 mag asec^{-2}	Lindler model[b]	Average V band surface brightness of zodiacal light for coronagraph observations
z_s	22 mag asec^{-2}	Lindler model[b]	Average V band surface brightness of zodiacal light for starshade observations
x	22 mag asec^{-2}		V band surface brightness of 1 zodi of exozodiacal dust[c]
n	LBTI best fit distribution		Number of zodis for all stars

[a] Actual lower bound is $R_p > 0.8/\sqrt{a}$

[b] Lindler zodiacal light model as a function of ecliptic latitude and longitude at observation time

[c] Local zodi based on ecliptic pointing of telescope. On average, starshade observes into brighter zodiacal light.

[d] For solar twin. Varies with spectral type, as zodi definition fixes optical depth.

final science product (Figure 11).

Characterization metric A facilitates a quick search for the water line at 940 nm. It is used by the LUVOIR observing scenario to vet candidates for a full spectra. The 20% bandwidth is achievable by a coronagraph in one observation. The spectral resolution of R=70 and SNR=5 is sufficient for detection of the waterline while keeping the integration time minimal.

Characterization metric B adds the oxygen line at 760 nm with a 20% bandwidth. The R=140 and SNR=8.5 is sufficient to detect the narrow water feature. A coronagraph can observe this additional 20% bandwidth subspectra series to the waterline subspectra.

Characterization metric C is the full spectra for the HabEx starshade. The baseline HabEx architecture uses the starshade to achieve a continuous spectra from 300 nm - 1000 nm in a single integration time to SNR=10 at 650 nm. The starshade IFS produces a spectra from 450 - 1000 nm that is an R=140. The starshade UV camera uses a grism to achieve R=7 from 300 - 450 nm. A coronagraph can cover the same spectra in a sequence of 20% BW subspectra. To minimize coronagraph integration time, the subspectra have the spectral resolution and SNR shown in Figure 11 for metric D, which are sufficient to resolve the features of interest in each subspectra.

Characterization metric C as rendered by the HabEx starshade and coronagraph are shown in Figure 12 for an earth-Sun twin at 7.5 pc, 5 exozodis and added noise The coronagraph meets the minimal spectral resolution and SNR to find the critical species of interest over a sequence of integrations while the starshade provides additional spectral resolution in a single observation to produce the spectra in one continuum.

Characterization metric D extends the spectral range to 1250 nm to observe the deep, broad water line at 1130 nm or the methane line at 1150 nm. The extension of the spectra into the NIR allows for observation of multiple absorption bands of a given species and breaks degeneracies of overlapping features. The R=40 and SNR=10 of the NIR subspectra allows for detection of water and methane in the NIR. In the UV, LUVOIR will use band photometry to achieve R=7, SNR = 5 subspectra. In the range from 450 to 700 nm, the species of interest (Water, Oxygen, Ozone, Methane, and Carbon Dioxide) do not produce features or produce

Table 5. *Instrument Parameters*

Parameter	LUVOIR B	HabEx
Primary Diameter (m)	8.0	4.0
Obscuration Factor	0.14	0
Integration Time Limit	60 days	60 days
	Coronagraph Performance	
Raw contrast floor[a]	1×10^{-10}	1×10^{-10}
Raw contrast stability[b]	1×10^{-11}	2×10^{-11}
Post-processing Factor	0.25	0.29
Systematic noise floor	26.5 Δmag	26.5 Δmag
Core throughput[b]	0.46	0.5
Photometric Aperture	0.8 λ/D	0.7 λ/D
Inner Working Angle, $IWA_{0.5}$	3.9 λ/D	2.4 λ/D
Inner Working Angle, $IWA_{0.1}$	1.5 λ/D	1.5 λ/D
Outer Working Angle	60 λ/D	26 λ/D
Bandwidth ($\Delta\lambda$)	20%	20%
	Imaging Channel 1†	
Non-coronagraph Throughput	0.17	0.28
Bandwidth	20%	20%
	Imaging Channel 2*	
Non-coronagraph Throughput	0.39	0.42
Bandwidth	20%	20%
	Spectral Channel	
Non-coronagraph Throughput	0.39	0.42
Bandwidth	20%	20%
$\Delta\lambda/\lambda$	140	140
λ	500 nm	500 nm
	Detectors	
Quantum Efficiency	0.9	0.9
Photon Counting Efficiency	0.75	0.75
Dark Current (e/s)	3×10^{-5}	3×10^{-5}
Read Noise (e/pix)	0	0
Clock-Induced Charge (e/s)	1.3×10^{-5}	1.3×10^{-5}
	Starshade	
Starshade Thrust (mN)	-	1040
Starshade Slew I_{sp} (s)	-	3000
Starshade Stationkeeping I_{sp} (s)	-	308
Starshade Wet Mass (kg)	-	11180
Starshade Dry Mass (kg)	-	4550
Starshade Separation (km)	-	76600

†Blue imaging band for HabEx, UV imaging band for LUVOIR B
*Red imaging band for HabEx, Visible imaging band for LUVOIRB

weak narrow features that require prohibitively large SNR, so R=7 and SNR = 8.5 is used.

For the HabEx starshade, the NIR spectral region can be observed by placing the starshade at a closer distance. The change in distance requires some days to slew the starshade, so NIR spectral characterization will not instantaneously follow the visible spectra. The starshade IFS has the capability for R=40 spectral resolution.

Additional metrics are reported for detected planets and planets promoted for characterization. These metrics are unique to the EXOSIMS approach of scheduling observations on synthetic planets. The simulated observation can be deemed successful

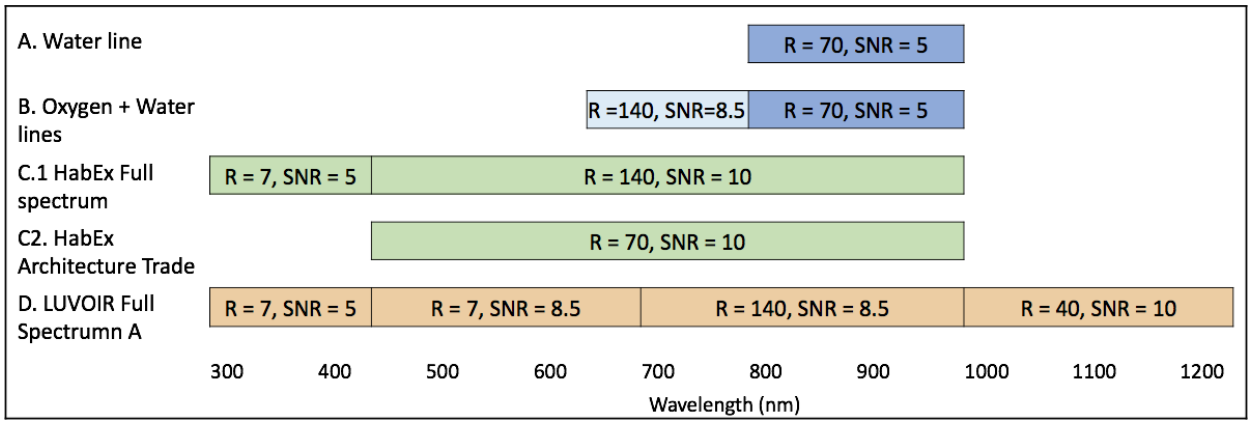

Figure 11. *Four yield characterization metrics are used: metric A (Water line, 20% bandwidth), metric B (water and oxygen lines, each at 20% bandwidth), metric C is the HabEx continuous spectrum from 300 nm to 1000 nm achieved by the starshade at R=140 and aggregated by a coronagraph in 20% bandwidth subspectra, metric D is the extends the spectra to 1250 nm for detection of water at 1200 nm.*

or not based on achieved SNR. Observations over multiple epochs and propagation of the synthetic planet determine when sufficient conditions are met for an orbit within the habitable zone and the planet is promoted for characterization. Due to efficiency of search, it is likely that the number of planets detected is larger than the number promoted.

AYO reports a single number for yield which includes the cumulative completeness for characterization and detection and accounts for the integration time for the number of detections required for orbit determination.

5. Yield Modeling

There are two basic approaches to yield modeling, using many of the same constituent parts and similar calculations, but arriving at the final yield estimates in fundamentally different ways. The first approach is to evaluate the summed completeness of a set of target stars for a particular planet population and instrument. Completeness, defined by Brown (2004, 2005) is the probability of detecting a planet from an assumed population, given it exists, upon the first observation of a target star with a particular instrument. The completeness of multiple stars, scaled by the expected occurrence rate of planets in the population, produces an expectation value for the number of planet detections for that observing program. An extension of Brown's original work (Brown and Soummer, 2010) allows for the inclusion of additional observations of the same target stars (revisits).

Alternatively, we can sample from the same planet population to create a synthetic 'simulated universe' in which planets are placed in orbits around some subset of our target stars in accordance with assumed occurrence rates. We can then simulate an observing sequence using our instrument description on this simulated universe, recording the numbers of successful planet detections and characterizations. An ensemble of such simulations (keeping the instrument description and mission rules constant while varying the random draw of planets) will provide both the expectation values and full distributions of planet detections.

As stated, the completeness yield and full mission simulation yield should (and typically do) produce very similar results. Differences in results occur when different input assumptions are made between the two methods, different operating rules are adopted (for example in how integration time is allocated per target), or when one method imposes different constraints than the other. Full mission simulations make it significantly easier to directly model dynamically evolving factors and constraints throughout the course of the mission, such as the motion of the observatory on its orbit, the observatory keepout regions, and local zodiacal light contributions. They also allow for the simulation of reactive mission rules, such as requiring characterization followups for positive detections. Such elements can be treated broadly in the completeness yield case, but as this approach does not directly model specific observations, or the execution of a time-dependent observing

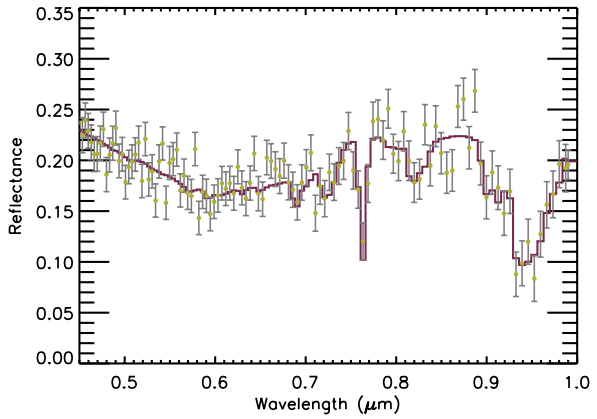

(a) *HabEx 4 m Starshade, R=140, SNR=10. Integration time = 390 hours.*

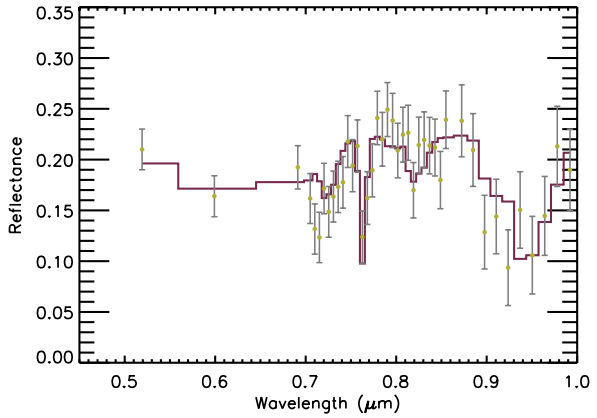

(b) *HabEx 4 m Coronagraph, 500-700 nm: R=7, SNR=8.5; 700-1000 nm: R=140, SNR=8.5. Cumulative integration time = 392 hours.*

FIGURE 12. *Synthetic spectra with added noise for an Earth-Sun twin at 7.5 pc. The magenta line is the Earth's spectrum at goal spectral resolution. The coronagraph 20% bandpasses have some overlap resulting in three duplicate points. Credit: Ty Robinson*

plan, it is much more difficult to capture such details.

On the other hand, the completeness yield is significantly less computationally intensive than the full mission simulation approach, meaning that more complex calculations can be carried out for the full target list, which would be prohibitively expensive to do in each iteration of a full mission simulation. At the same time, the full mission simulations may produce poor yields not due to any particular issue with the instrument or observatory design, but solely due to the assumed operating rules. As a trivial example, we can consider a simulation where every planet detection immediately triggers a spectral characterization attempt. If the assumed planet population is sufficiently broad, then practically every target in a given mission instance may have a detection. A simulation following the instant characterization rule would therefore waste large amounts of time on characterization and produce a poor detection yield. All together, these considerations mean that we should treat completeness-based yields as somewhat optimistic, and describing the case where a mission is executed in a completely optimal fashion. Full mission simulation results, on the other hand, should be treated as lower bounds on performance, as there always remains the possibility that improved mission operation rules will improve the yield. When the two approaches broadly agree, then we should have high confidence in the results, remembering always that the results are entirely dependent on our input assumptions.

For this report, we employ two pieces of software, implementing the completeness yield and full mission simulation approaches, respectively. The first is written and maintained by Chris Stark, and based largely on his Altruistic Yield Optimization (AYO; Stark et al., 2014) algorithm. The second is the EXOSIMS framework (Savransky, Delacroix, and Garrett, 2017a). The implementation specifics of these two codes are described below.

5.a. **AYO.** To calculate expected exoplanet yields, the AYO yield code of Stark et al. (2014) was used, which employs the completeness techniques introduced by Brown (2005). Briefly, for each star in the input star catalog, a random distribution of a large number of synthetic planets of a given type was made, forming a "cloud" of synthetic planets around each star, as shown in Figure 13.

Planet types are defined by a range of radii, albedo, and orbital elements. The reflected light flux was calculated for each synthetic planet, giving its properties, orbit, and phase, and then determining the exposure time required to detect it at a threshold SNR. Based on these detection times and the exposure time of a given observation, the fraction of the synthetic planets that is detectable (i.e., the completeness, as a function of exposure time) was calculated. The completeness simply expresses the probability of detecting that planet type, if such a planet exists. The average yield of an observation is the product of the completeness and the occurrence rate of a given planet type. This process is repeated for every observation until the

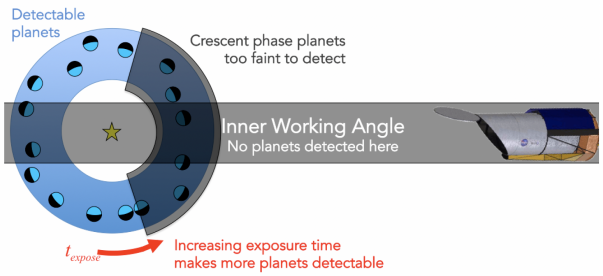

FIGURE 13. *The completeness of an observation is the fraction of detectable planets to total planets and is a function of exposure time. The yield of an observation is the product of completeness and the expected number of planets per star (the occurrence rate).*

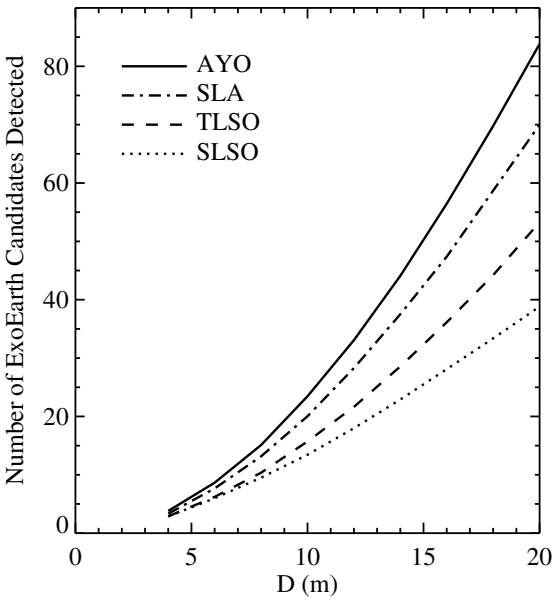

FIGURE 14. *Expected yield vs telescope diameter from Stark et al. (2014) for four different observation design methods. AYO optimization plays to the strengths of a mission to maximize yield of a given planet type.*

total mission lifetime is exceeded, arriving at an average total mission yield. In reality, yields may vary from this average due to the random distribution of planets and exozodi around individual stars (this source of uncertainty was incorporated in the AYO yield calculations by accounting for the Poisson probability distribution of planets and exozodi for each star).

The techniques of Stark et al. (2015) and Stark et al. (2016b) use a cost:benefit calculation to optimally distribute a mission's limiting resource to the most rewarding observations, maximizing the overall yield of a given planet type. For a coronagraph-based search, this involves optimizing the targets selected for observation, the exposure time of each observation, the delay time between each observation of a given star, and the number of observations of each star given an overall time budget(Stark et al., 2015). For a starshade-based search, a similar optimization was made, but the time between observations was not allowed to be optimized due to expected scheduling constraints; instead the balance between fuel use and exposure time was optimized given both time and fuel budgets(Stark et al., 2016b). Via observation optimization, the AYO code adapts the observing strategy to play to each mission's strengths and avoids the pitfalls that can result by making non-ideal assumptions about the target list, observing cadence, or preferred target stars. Figure 14 illustrates the yield benefits of AYO when compared to other methods for choosing exposure times and target lists (Stark et al., 2014).

After optimizing the observation plan for planets of a given type, the set of observations and target stars is saved. The AYO yield code can then be called again, with optimization turned off, to calculate the yields of other types of planets that would be detected using the saved set of observations and target stars. To do so, AYO simply generates other clouds of exoplanets for each of the 15 types defined by Kopparapu et al. (2018) and calculates the completeness of each observation; AYO returns the expected yields for all types of planets when optimizing the observing strategy for a single planet type.

AYO does not directly schedule observations, nor does it calculate the visibility of any individual star as a function of time. The ability to schedule the observations is expected to have a negligible impact on coronagraph-based surveys given the large instantaneous fields of regard of the missions simulated. However, the ability to schedule the observations would be more of an issue for the starshade, which has a smaller field of regard and requires direct scheduling with realistic mission dynamic elements, such as solar angle constraints.

5.b. **EXOSIMS.** EXOSIMS consists of a collection of modules, abstracting out various state variables and methods associated with different aspects of the

full mission simulation, all with a strictly defined input/output specification. This allows for modules to be extended, or for new modules to be implemented, without requiring any modifications to other portions of the code. EXOSIMS is thus adaptable to entirely new designs for instruments, observatories, or overall mission concepts. The module functionality is split as follows:

- Optical System: a description of the observatory optics, all science instruments, starlight suppression systems (coronagraphs and occulters), and methods for computing integration times for different targets to varying levels of contrast
- Star Catalog: an input stellar catalog with astrometric and photometric information on potential target stars
- Planet Population: a statistical description of the planet population including factorized or joint density functions for all planetary physical and orbital parameters
- Observatory: a description of the observatory spacecraft, its orbit, and methods for computing target look vectors, keepout regions, and fuel use for starshade slewing and stationkeeping
- Planet Physical Model: methods for converting between planet mass and radius, and descriptions of planet phase functions
- Time Keeping: methods for tracking mission time throughout the simulation, including time specifically devoted to exoplanet science
- Zodiacal Light: descriptions of local and exozodiacal light
- Background Sources: models for false positives generated from background sources
- Post-Processing: models for the effects of post-processing
- Target List: methods for filtering the full star catalog to a list of targets for a specific instrument and mission
- Simulated Universe: methods to sample the planet population and assign simulated planets to stars from the target list
- Survey Simulation: methods for simulating the full mission, including logic for automated scheduling of targets
- Survey Ensemble: methods for generating ensembles of full survey simulations

Figure 15 shows a schematic representation of how an EXOSIMS Mission Simulation object is constructed out of the individual modules. Yield is calculated from a generated Survey Ensemble, which contains the outputs of N Survey Simulations, each of which uses exact copies of all of the downstream modules, except for the Simulated Universe, which is re-generated (by re-sampling the planet population) for each individual simulation.

The execution of a single mission simulation occurs within a top-level loop which selects each subsequent target from the pool of 'currently' (at the current simulated mission time) available targets, calculates the required integration time, simulates the observation (and followup characterization, if called for by the selected mission rules) and then simulates the outcome, which can be a true positive (detection), false positive (misidentified speckle or background object), true negative (null detection) or false negative (missed detection).

Figure 16 shows a schematic of the default observation loop. The functionality of the default survey execution is extended and augmented in multiple additional Survey Simulation implementations designed specifically for analyzing HabEx and LUVOIR. Below we detail two of these, which were used extensively to produce the results in this report.

5.b.i. *Weighted Linear Cost Function Scheduler.* The weighted linear cost function scheduler, provided by EXOSIMS Survey Simulation implementation 'linearJScheduler', is based on the observation scheduling methodology described in Savransky, Kasdin, and Cady (2010). A merit function is defined to represent the 'cost' of transitioning from observing the current target (i) to observing the next target (j), of the form:

$$A_{ij} = \sum_k a_k \, c_k(i,j) \,, \tag{3}$$

where $\{c_k\}$ are independent cost/reward terms (depending on one or both of the current and next targets), and $\{a_k\}$ are normalized weighting factors. An adjacency matrix $[A]_{ij} = A_{ij}$ for all targets represents the edges of a directed, cyclic graph whose nodes represent all possible subsequent observations. While such a matrix representation cannot encode the dynamic constraints and system evolution described above, it represents a valid approximation for a fixed number of observations (the specific number is dependent on the length of each observation and how much time is required to pass between observations). We can thus approximate a small number of future observations using the current adjacency matrix and determine the minimum cost path through the graph for that fixed number of steps. The root node of this graph is then selected

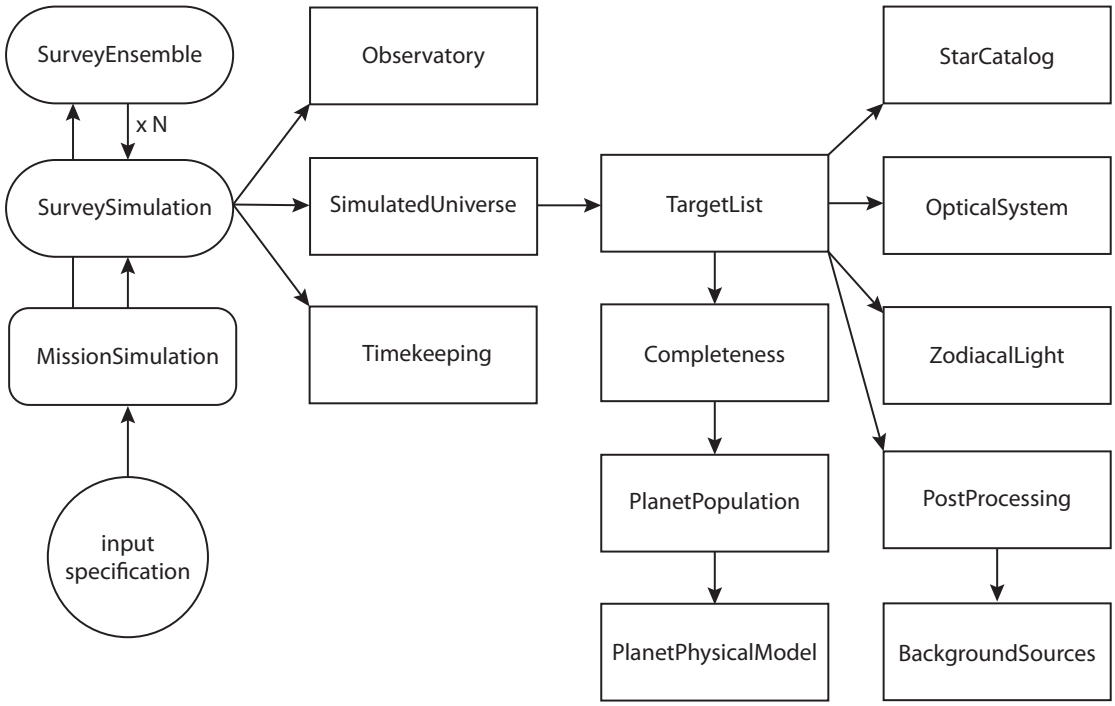

Figure 15. *Schematic depiction of the instantiation path of all EXOSIMS modules. The arrows represent instantiation of an object, and object references to each module are always passed up directly to the top calling module, so that a given module has access to any other module connected to it by a direct path of instantiations. For example,* TargetList *has access to both* PostProcessing *and* BackgroundSources*, while* Observatory *does not have access to any other modules. The typical entry point to EXOSIMS is the construction of a* MissionSimulation *object, which causes instantiation of* SurveySimulation*, which in turn instantiates all the other modules. In the case of a parallelized* SurveyEnsemble*, multiple, independent* SurveySimulation *modules are instantiated at the same time.*

as the next target, the observation is simulated, and the full adjacency matrix is recalculated at the time of the start of the next observation.

The linearJScheduler implementation uses a five-term cost function with the following terms:

(1) For the case of an external occulter, the first term encodes the cost of transitioning the occulter between the two targets, either via a direct calculation of fuel use, as detailed in Soto et al. (2018), or via a heuristic proportional to the angle between the telescope look vectors to the two targets. For the case of an internal coronagraph, it is assumed that all telescope re-pointings have approximately equal cost and this term is set to zero.
(2) The second term represents the reward metric of the observation, encoded as 1 minus the target completeness.
(3) The third and fourth term bias towards previously unobserved stars and stars observed less frequently. The weights on these terms increase exponentially with mission time, making it less costly to make new observations (versus revisits) towards the end of the mission execution, and to prevent high-completeness targets from being repeatedly revisited.
(4) The fifth term biases observations towards targets that are scheduled for observation near the current mission time.

Changing the weighting factors on these terms effectively changes mission priorities and rules. Optimal weighting factors can also be determined by wrapping the whole simulation in an optimization scheme with an appropriately-defined objective function (e.g., the number of Earth-twin spectral characterizations within a fixed set of simulated universes). This approach was used several times to evaluate parameter choices for this scheduler under different operating conditions.

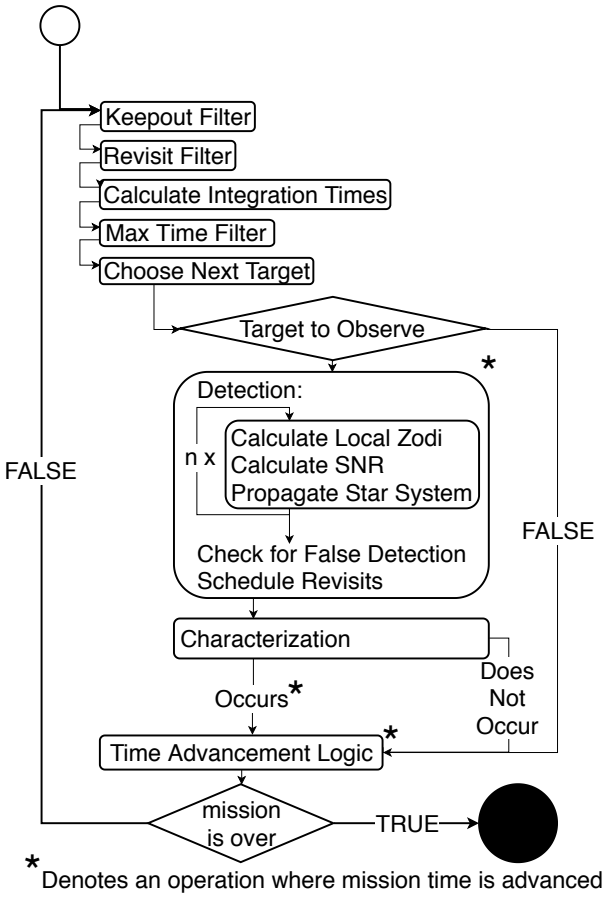

FIGURE 16. *Mission simulation top-level loop. At every loop iteration, targets in keepout regions are filtered out, along with previously observed targets, unless explicitly scheduled for re-observation. Integration times are calculated based on current zodiacal light levels, and targets with too-long integration times are removed. From the remaining targets, one is selected for observation. Integrations are split into n segments, with spacecraft and target positions, and the local zodiacal light contribution, updated in each segment, and the integrated signal and noise is approximated via Riemann sums. Detections and false alarms are generated probabilistically, based on the threshold SNR of the observation, and assuming Gaussian statistics for the noise. Mission time is advanced according to mission operating rules to account for other observatory science, and the loop repeats until no mission time remains.*

5.b.ii. *Tiered Scheduler.* The Tiered Scheduler was developed for the HabEx hybrid starshade and coronagraph architecture. It is a tiered, or hierarchical scheduler that utilizes the above weighted linear cost function scheduler for the starshade. The starshade is scheduled first using the weighted linear cost function scheduler to solve the travelling salesman problem (TSP) of the starshade path. During the starshade slews, coronagraph observations are scheduled on the second tier. Also during the slews, general observatory observation (GO) time is allocated at the specified rate, which is 50% for the HabEx baseline mission concept. GO time is allocated whenever "owed" GO time accumulation exceeds 1 day, unless a starshade observation is occurring, then the owed time is allocated at the end of the starshade observation. This distributes the GO time evenly throughout the mission. Additional details are in the results section for the HabEx 4H hybrid case (§6.a).

6. Results

The results are presented by architecture and its appropriate observing scenario.

6.a. **HabEx 4H: Starshade and Coronagraph .** The HabEx 4-meter H, or hybrid, case consists of a coronagraph used in a blind search for the detection of exoplanets and a starshade for the spectral characterization of exoplanets. The hybrid case utilizes the strength of the coronagraph, which is its agility to observe and revisit numerous targets, and the strength of the starshade, which is to provide a continuous spectrum over more than 100% bandpass. Observation scheduling is of critical importance to the starshade design reference mission. Observation scheduling, using the realistic solar constraints and slew transits between targets, shows that the design reference mission is achievable and verifies that the design of the starshade (dry mass, fuel mass, and propulsion) closes.

Observation scheduling with EXOSIMS utilizes a tiered approach. In the top tier, the slews of the starshade have top priority and are scheduled using a two-step look ahead Traveling Salesman Problem (TSP) optimizer described in section §5.b.i. Characterization targets consist of the initial eight “Deep Survey” stars and any targets discovered and vetted by the coronagraph blind search, denoted as “promoted” targets. As exoplanets are discovered and their orbits are determined, if the synthetic planet meets the criteria of an exoearth candidate (EEC), the target is promoted to the characterization target list. During starshade slews, the second tier makes detection observations with the coronagraph and general observer (GO) observations.

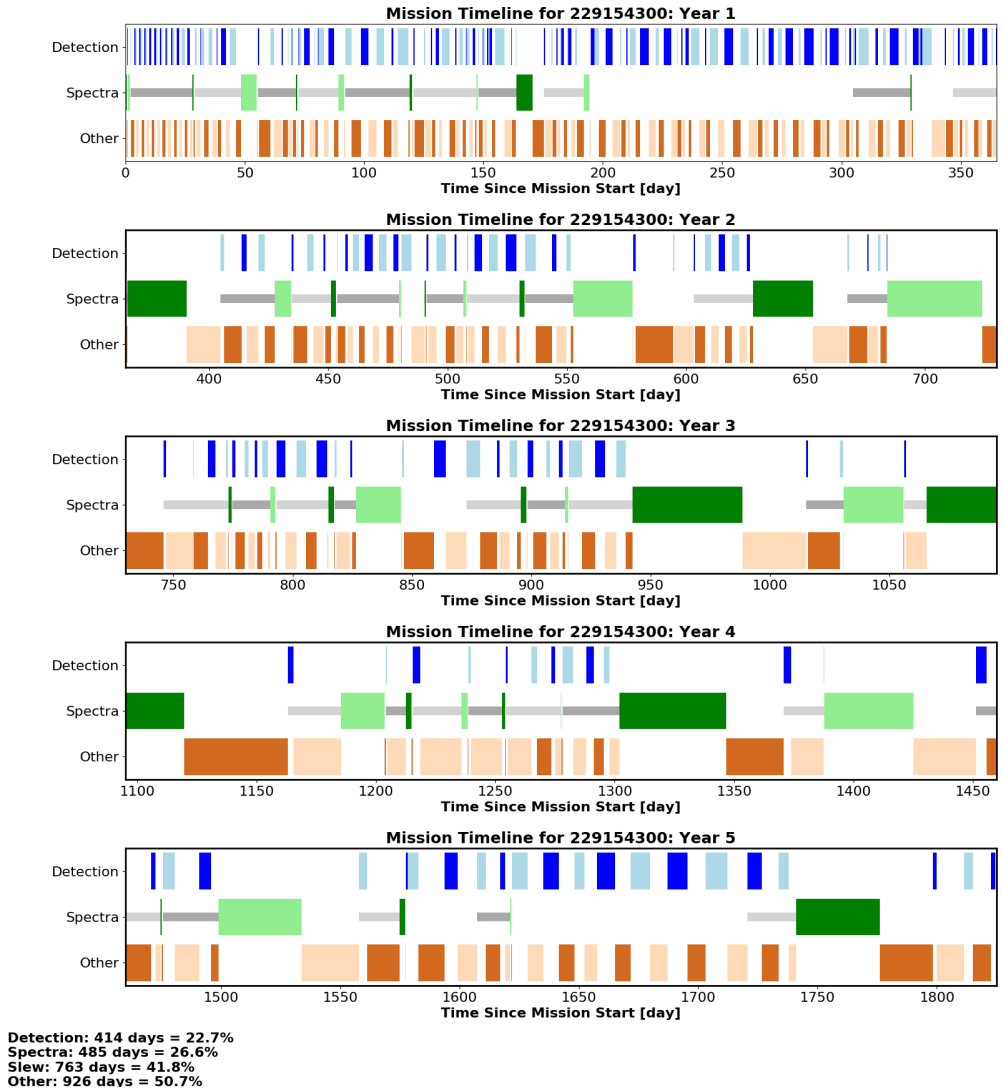

FIGURE 17. *The observation timeline of the Tiered Scheduler for HabEx 4H shows spectral characterizations with the starshade (gray bars show minimum slew time with 85% burn portion, and green is the integration time for 300–1000 nm spectra at R=140 to SNR=10), the detection observations with the coronagraph (blue), and general astrophysics observations (in orange, labelled "Other") for one particular synthetic universe and observing sequence. Alternating observations are visually distinguished by light and dark colors.*

The coronagraph blind search target list is ranked by probability of detection divided by integration time to detect an earth twin at quadrature. The target list is observed in rank order until the revisit wait period has elapsed. The wait period for each star is a third of the period of an earth twin around that star. The stars are observed by the coronagraph at the cadence of their revisit wait period, with priority given to higher ranking stars. The third tier of the scheduler allocates time for general observing (GO). Time is allocated to GO at the rate of 50% of the mission time, distributed throughout the mission.

Figure 17 shows the observing sequence over 5 years of mission time for one particular synthetic universe. The eight broad survey targets are observed first, then characterizations wait for the blind search to promote planets. The eight broad survey targets are observed again and other targets as they are promoted. The spectra occuring throughout the five year mission shows the mission elapsed time at which new EECs were promoted by the

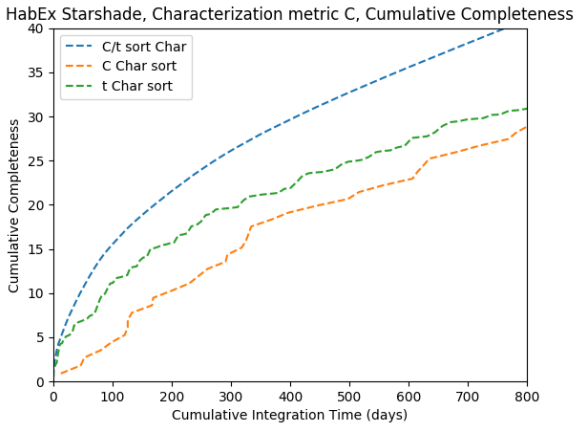

FIGURE 18. *For the spectral characterization with the HabEx starshade, the cumulative completess is plotted against the cumulative integration time when the targets are sorted by 1)Completeness/integration time, 2) Completeness, 3) integration time. The completeness was the single visit completeness; the integration time was the integration time to a limiting* Δ *magnitude of 26.*

coronagraph blind search. For the yield calculations, hundreds of synthetic universe realizations with their associated observing sequences were used and statistics calculated on the ensemble of realizations.

6.a.i. *Starshade Scheduling.* With the complexity of observation scheduling, it is important to evaluate the impact of realistic scheduling against more optimistic yield assessments. To do this, we separate the coronagraph blind search from the starshade characterization scheduling. To establish a simplistic upper bound of yield, we plot the cumulative sum of single visit Completeness against the cumulative sum of the single visit integration time to limiting Δ magnitude of 26 (Figure 18). The targets are ranked by Completeness, Completeness divided by integration time, and by integration time. Yield is achieved most quickly for ranking by Completeness divided by integration time, an important lesson used in the coronagraph blind search.

Let's explain two example data points from Figure Figure 18: for 330 days, the cumulative completeness is about 21 exo-earths and for 720 days the cumulative completeness is about 30 exo-earths. The first number corresponds to the 0.9 years of mission time allocated in the baseline HabEx observing scenario to perform spectral characterizations of systems to a depth sensitive to exo-earths. This sets an simplistic upper bound on the HabEx starshade spectral characterization yield. The HabEx scenario expects to make multiple visits, three to each EEC and three to the deep survey stars, so this reduces the simplistic upper bound by one third to become about 7. Depending on the revisit policy and the number of targets promoted for starshade characterization, the simplistic upper bound is between 7 and 21 stars. Note that an even more optimistic upper bound could be achieved using a more optimal static allocation of integration time for the mission time available, such as in the AYO simulations.

We make use of the second data point from Figure 18, to evaluate the impact of starshade slew scheduling. Using EXOSIMS, we isolate the impact of starshade slewing, including the TSP, on characterization yield by simulating an omniscient scenario in which all the exo-earths in the synthetic universe are promoted on Day 1 of the mission and their exact integration time is known. The EECs are positioned at quadrature during characterization so that every observation has favorable IWA and photometry. The exozodical light is set to 3 zodis.

The average number of exo-earths spectrally characterized with the starshade was 27. This is close to the simplistic upper bound for this omniscient case of 30 exo-earths at 720 days; some minor yield degradation could be due to starshade slew scheduling and observing consraints. The observation timeline for a single, representative DRM (or universe) in Figure 19 shows that the population of characterizable exo-earths with the occurrence rate of 0.24 was exhausted during the 5 year mission time. Additional post-processing confirmed that all of the targets in each DRM with an integration time less than the 60 day limit was characterized. The ability of the starshade to slew between observations was not the rate limiter for the omniscient scenario. (Starshade slew times and path optimization could be a limit to the number of revisits, though revisit efficiency was not deeply investigated in this study.)

The omniscient case was also used to tune the weighting coefficients of the TSP cost function. For the omniscient case, in which revisits were unnecessary, the two cost function variables were integration time and slew time. The tuning of the coefficient weights was fairly insensitive to coefficient variation because all of the viable targets were observed during the mission. For a shorter mission or fewer targets, the coefficient weights would have higher sensitivity and impact. This result underscores the importance

of the coronagraph blind search to promote targets to the starshade.

Next, the favorable planet position condition was removed and planet phases were allowed to follow their internally-consistent orbital propagation throughout the simulation. Thus, the observation by the starshade is independent from the planet phase. The resulting number of characterizations, for the same ensemble of universes, is 14.8. This drop in yield from 27 exo-earth characterizations is consistent with Figure 45, where for a dozen nearby stars the starshade keepout and planet SNR are plotted and the average joint probability of characterization observability is ∼50% averaged over several years. Additional discussion is provided in 6.d along with a corresponsing observation timeline (Fig. 40).

6.a.ii. *Coronagraph Blind Search Scheduling.* Now that the bounding cases of starshade scheduling have been explored, we turn to the coronagraph blind search. The coronagraph, with a 40 degree sun avoidance angle, has a large region of observability and the keepout constraints are likely to have only the most minor impact on efficiency of coronagraph observations. The importance of observation scheduling for the coronagraph is in the revisit cadence for optimizing the probability of detection and successful orbit determination. While AYO allocates at least 6 coronagraph detection observations with the assumption that 4 will succeed in detection (the minimum required for orbit determination), EXOSIMS schedules the detection observations at a cadence optimal for orbit determination and promotes the planet only when the minimum number of detections span more than half a period.

The crafting of the blind search seeks to efficiently discover, revisit, and retire targets. The target-rich environment for coronagraph detections means that target pruning should be applied. The first constraint applied is to filter the targets for the potential characterization outcome, not the detection outcome. Targets are excluded if the characterization integration time for an Earth twin at quadrature is greater than 60 days and if the completeness is below 10%. Figure 20 shows the subset of targets kept after filtering for characterization criteria (colored by completeness) and the targets (grey) which have detection integration time less than 60 days.

A null detection could occur when the planet is obscured, has a poor SNR, or if a planet does not exist. A high number of visits with null detections, while conservatively thorough, uses integration time that could be spent on other targets. Following reasoning similar to Brown and Soummer (2010, sec. 3), we note that the probability of a series of N independent missed detections, if there is an Earth present, is $(1-C)^N$, where C is the single-visit completeness. Turning this around via Bayes theorem shows that

$$P(\text{Earth} \mid N \text{ misses}) = \frac{P(N \text{ misses} \mid \text{Earth})}{P(N \text{ misses})} = \frac{(1-C)^N \eta}{(1-C)^N \eta + (1-\eta)} \quad ,$$

from which it is easy to find the number of observations needed to force this below any given threshold (Figure 21). For example, for moderately difficult targets with $C = 0.5$, five failed observations are needed to force the probability that an Earth is present below 0.01.

The craftsmanship of the coronagraph blind search involves trading thoroughness for efficiency. A parameter sweep was performed for: the weighting factor of revisits, number of allowed null detections, maximum number of successful detections, the minimum number of detections required for promotion. The heuristic that produced the highest characterization yield was used for all the coronagraph blind searches. Other approaches may more efficiently promote targets, such as a dynamic global optimizer (Savransky, Delacroix, and Garrett, 2017b), whose implementation in the Tiered Scheduler exceeded the scope of this study. Figure 22 shows the histogram of the total number of detections (blue) and the subset of detections which contributed to a promoted target (yellow) for the nominal, baseline HabEx case. An average of about 280 detection observations occurred of which $\tilde{5}0$ contributed to targets that were promoted. The detection observations on promoted targets includes nulls and the three to four successful detections required for orbit determination.

In comparison to AYO, AYO allocated ∼280 detections, each of which contained a minimum of 6 detection observations to allow for 4 successful detections and 2 null observations. The AYO yield of 8 earths corresponds to a minimum of $6 \times 8 = 48$ detection observations, which is very close the ∼50 simulated by EXOSIMS. The total number of detections of 280 is the same for AYO as EXOSIMS. This shows a strong similarity of result for the coronagraph results, which are weakly influenced by

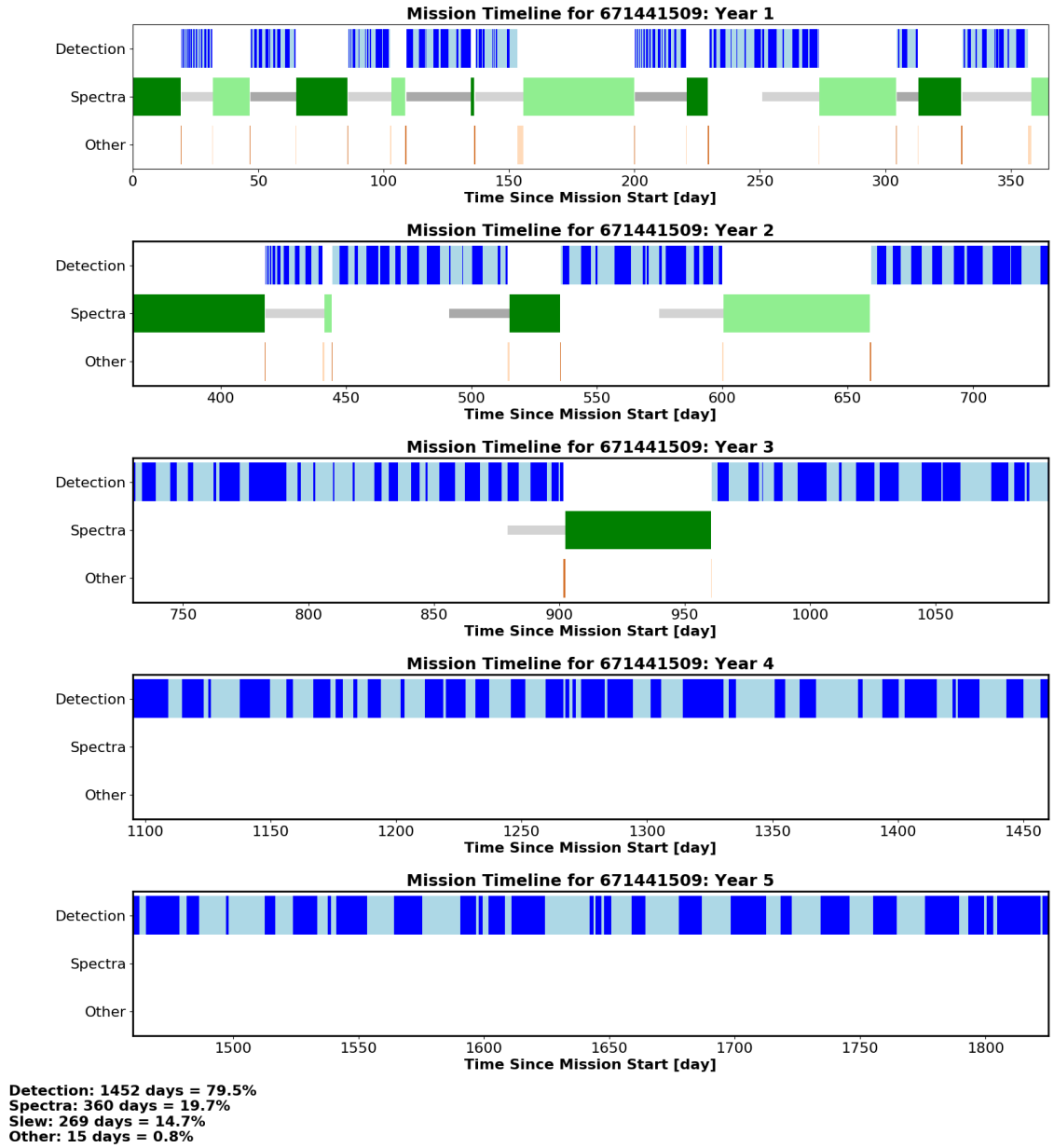

FIGURE 19. *The observation timeline for an omniscient case in which all characterizable earthlike planets were promoted to the starshade target list at the mission start. The exo-earths were placed at quadrature. The timeline shows the slew-limited rate of observation for one particular synthetic universe. The characterizable targets were exhausted. Coronagraph observations were allowed to occur during slews to compare the blind-search discovered targets to the omniscient characterized targets. All observation types have alternating light and dark colors to distinguish event sequences.*

the region of observability and more strongly by the crafting of the coronagraph blind search.

6.a.iii. *EXOSIMS Yield Results for HabEx 4H.* Now that the coronagraph blind search has been crafted, the two tiers of the scheduler are rejoined so that the targets found and vetted by the coronagraph blind search are promoted to the starshade for characterization. The full HabEx observing scenario uses the eight broad survey targets and the promoted targets. The characterization observations are performed with the planets at quadrature. While the purest mission simulation would schedule

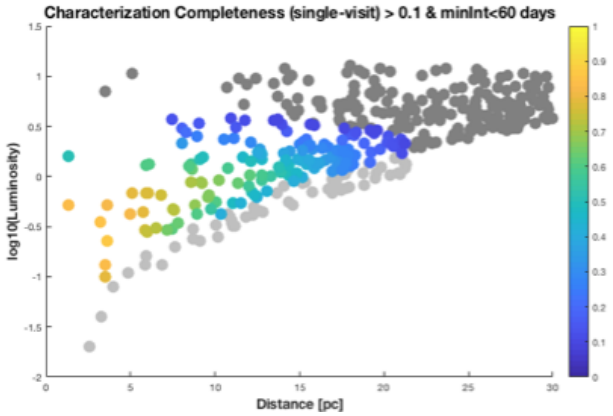

FIGURE 20. *Target stars color coded by characterization completeness as function of distance from Sun and stellar bolometric luminosity. Targets whose detection integration times are longer than 60 days (dark grey) or which have completeness <10% (light grey) are filtered out.*

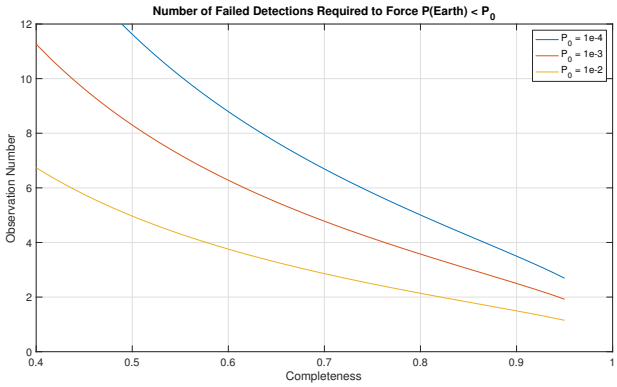

FIGURE 21. *The number of failed detections required to force the probability of an EEC less than a selected threshold P_0, as a function of first-visit completeness, taking $\eta = 0.24$.*

visits to occur when the EEC was at the most favorable orbital phase, this currently is a topic for research. The use of the EEC at quadrature is motivated by two arguments: first, that the orbit determination problem can be solved, as supported by the illustrative case in Figure 45; and second, that it is of greatest value to present the fundamental constraints on yield rather than the convolution of two imperfectly-understood optimization problems (orbit determination and orbit-cognizant scheduling).

An animation of the observation sequence for one of an ensemble of DRMs is available on the SDET website https://exoplanets.nasa.gov/exep/. The final frame of that animation, which overlays 5

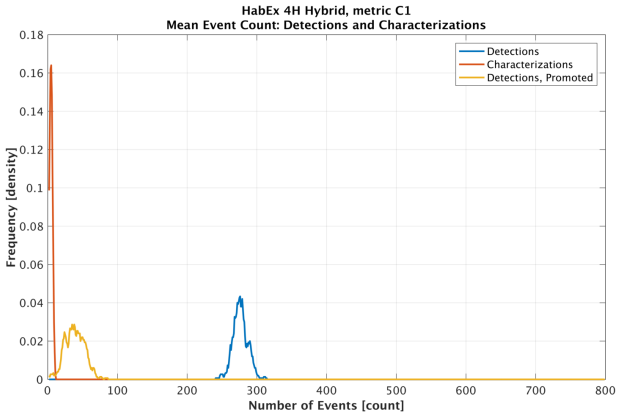

FIGURE 22. *Detections and characterizations for the tiered scheduler nominal case. All plotted quantities are probability mass functions (histograms) for discrete event counts across an ensemble of 46 simulated universes and consequent observation sequences. The blue line, peaking around 280, shows the count of detection events for each simulated mission. The gold line shows how many of these detections were done on targets that were eventually promoted, and the red trace shows how many characterizations were actually performed.*

years of observation, is shown in Figure 23.

For the nominal, baseline case, 9.1 EECs were characterized by the starshade, and 14.4 exo-earths had at least one detection by the coronagraph. The plots are presented in the order of detections with the coronagraph, including a plot of blind search efficiency, and then the characterizations.

Rhonda: add words explaining these plots.

6.a.iv. *AYO Yield Results for HabEx 4H.* AYO produced results for the HabEx baseline case which are shown in the HabEx Final Report in Chapter 3.3 and Appendix C. The results correspond to characterization metric C, the continuous spectrum produced by the HabEx starshade. Time was allocated based on four survey strategies.

The overall 2.5-year exoplanet survey consists of:

- Starshade survey of star systems with non-exo-earths consisting of 0.5 years of integration time and about 35 starshade slews.
- Starshade characterization of discovered exo-earths, consisting of 0.65 years of integration time and about 25 visits (about three revisits to 8 discovered EECs).

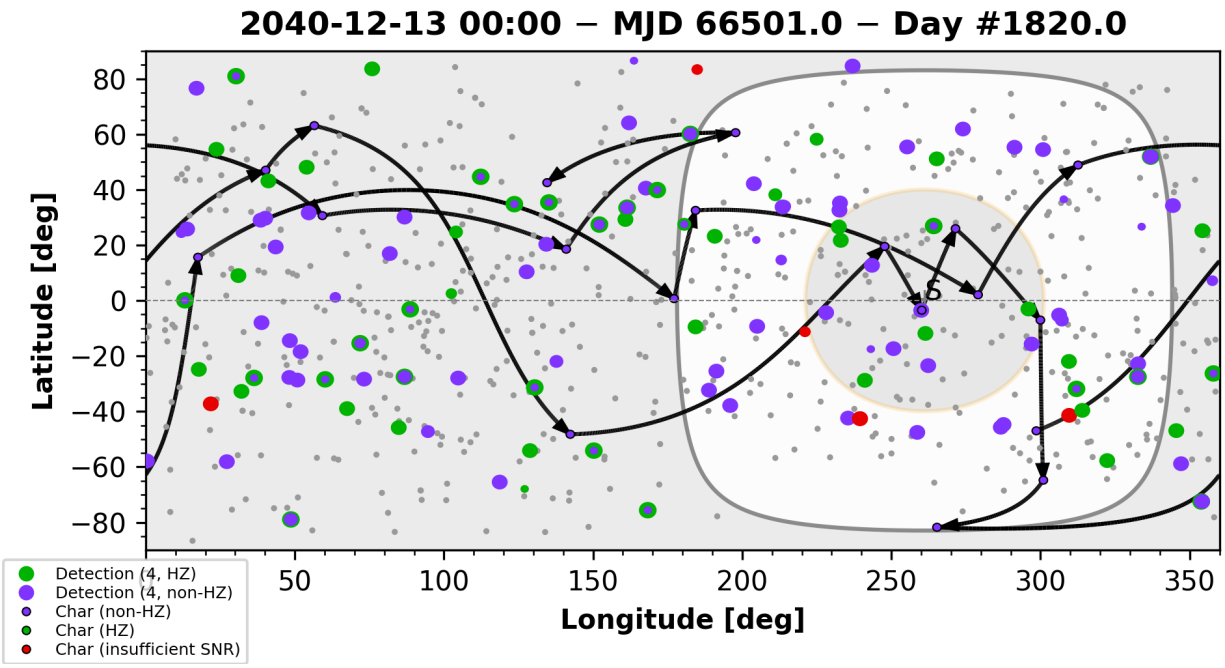

FIGURE 23. *The synthetic planets are 'observed' and considered detected or characterized if the goal SNR is reached: green for rocky planets in the HZ, purple for all other planets including rocky planets not in the HZ, red for insufficient SNR to detect any planets, grey for an unobserved star, all from a broad list of ∼760 potential target stars. The size of the circle indicates the number of repeat detections or characterizations, with the case of 4 detections shown in the legend for scale. Spectral characterizations with the starshade are distinguished by a black edge around the circle marker and are at the tip of a black slew arrow. The white annulus is the region of observability for the starshade. The central grey circle with yellow boarder is the solar keepout zone for both the coronagraph and the starshade. The position of the Sun is labeled 'S' and denoted by a grey cross.*

- Coronagraph blind search and orbit determination via ∼6 detection observations per star consisting of 1.1 year of total detection integration time and about 280 observations.
- 3 months of deep survey, using the starshade only for broad-band large OWA imaging and spectral characterizations at 3 different epochs of eight predetermined stars.

Discussion and additional explanation of HabEx AYO results from the HabEx final report will be added here to provide context for the reader.

Metrics A (20% BW at waterline) and B (water and oxygen line, 40% BW) are subsets of metric C, the continuous spectrum for HabEx already presented in these results. Metric D, 300 nm–1250 nm can be accomplished by the HabEx starshade at two distances: the nominal separation distance of 76,600 km and the nearer distance of 42,600 km (HabEx Final Report Table B.1-3, p. B-13). The two distances were scheduled as two different visits to the target, a different distance at each visit. Since the nominal observing scenario planned for three visits to each of the EECs, one of those visits was used as the closer distance for NIR and there was little impact on the characterization yield.

6.b. **LUVOIR B.** LUVOIR B uses the coronagraph instrument for detections for the blind search and orbit determination as well as the spectral characterization. The spectral characterization is limited to 20% bandwidth and is accordingly performed in serial to achieve an aggregate spectrum. The solar keepout constraints are generous with solar keepout angles at 90 degrees for typical observations and 45 degrees for high value observations, such as characterizations. The importance of observation scheduling for the coronagraph-only mission is not in the solar keepout constraints but in determining the revisit cadence for detection and the revisit cadence for orbit determination. The observation scheduling exposes the inefficiency of the blind search with

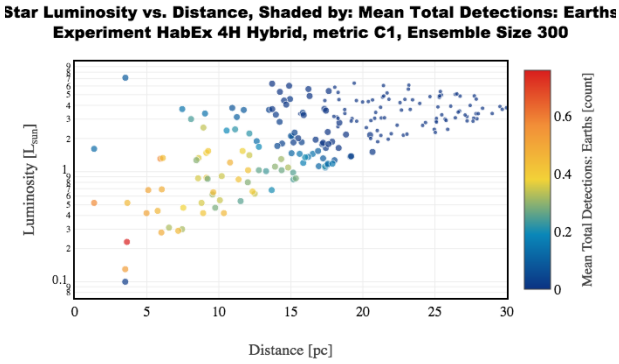

(a) *Detected exo-earths*

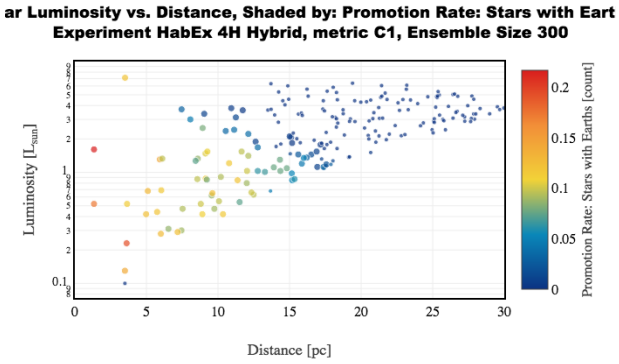

(b) *Promoted for characterization*

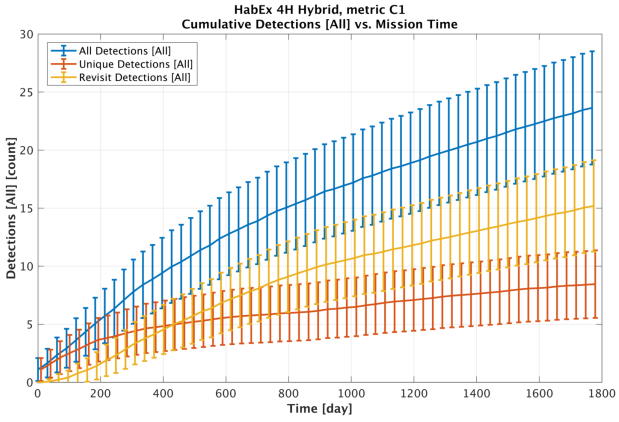

(c) *Mission time of first characterization observation*

FIGURE 24. *(a) exo-earths that received atleast one detection, (b) exo-earths candidates that meet the promotion criteria, (c) The targets with high completeness/integration time are observed early in the mission.*

the coronagraph under realistic mission scheduling constraints.

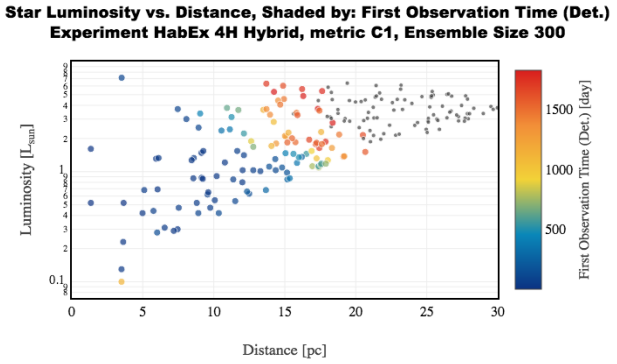

FIGURE 25. *Over the mission time, the unique detections declines as the target pool for the blind search progresses to longer integration time targets. Revisits begin after a wait period of one third of an orbit. Characterizations begin after targets are promoted.*

The LUVOIR B nominal observing scenario allocates 6 months for full spectra characterization and 2 years for the coronagraph blind search and initial characterization with metric A, water line detection at 940 nm. The EXOSIMS results presented here use 50% of the 5 year mission time, or 2.5 years, for the coronagraph blind search and characterization of targets at the water line. The 2.5 years, instead of 2 years, was used to facilitate comparison with the HabEx architectures and other metrics which were evaluated for 2.5 years of total mission time.

The EXOSIMS coronagraph-only scheduler makes detection observations and revisits until an exo-earth candidate is discovered and the orbit characterized by a minimum of 3 detections spanning more than half a period, then the target is promoted for spectral characterization. Spectral characterization is prioritized over the coronagraph blind search and happens immediately after the final orbit-determination detection, if sufficient time remains in the window of observability. For the characterization observation, the exoplanet is place at quadrature, as with the Tiered Scheduler, with the justification that the characterization could be scheduled at a favorable viewing angle once the orbit is determined. It was beyond the scope of this study to fully implement scheduling constraints and optimizations based on exoplanet ephemerides.

For the LUVOIR B coronagraph blind search, the same heuristics for pruning null observations were used as for the HabEx coronagraph blind search. A parameter sweep was also performed for LUVOIR B

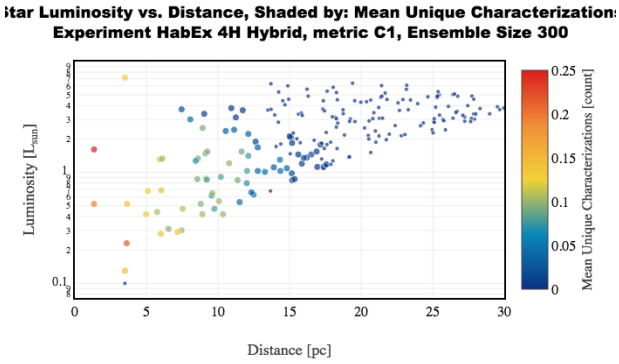

(a) *Characterized exo-earths*

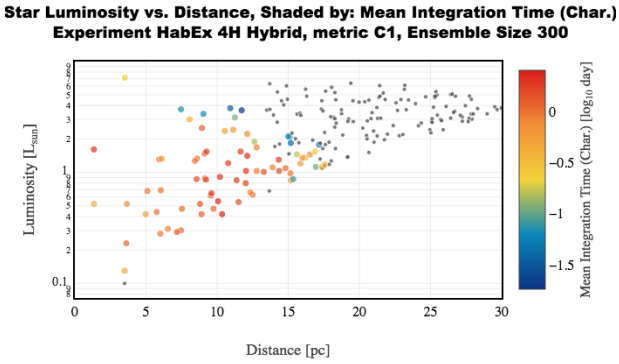

(b) *Characterization integration time*

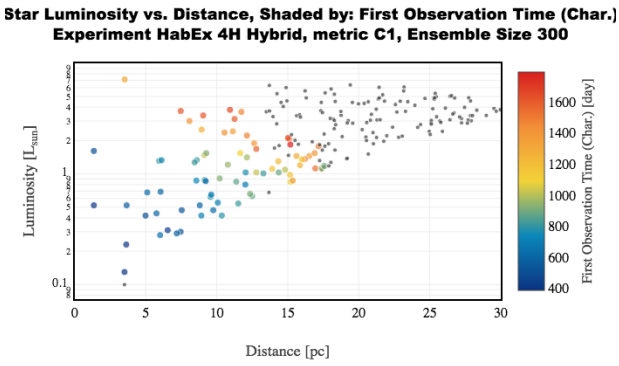

(c) *Mission time of first characterization observation*

FIGURE 26. *All of the targets promoted by the coronagraph are spectrally characterized. The high completeness targets are characterized early in the mission because they are promoted early in the mission.*

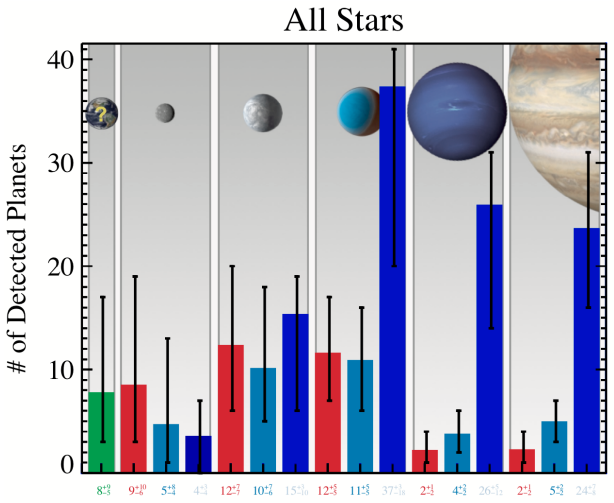

FIGURE 27. *AYO calculated a yield for HabEx of 8 potential Earth analogs (green bar), 55 rocky planets, 60 sub-Neptunes, and 63 gas giants. Yield mean values and uncertainties for each planet type are indicated at the bottom of the plot.*

coronagraph blind search to maximize yield. The coronagraph blind search detects more exo-earths than are promoted and characterized due to the limitations of the physical cadence of the blind search, particularly the target that whose observations are begun late in the mission when insufficient time remains for the correct cadence of repeated observations for orbit determination. The coronagraph blind search also has an inefficiency which could be improved by a different optimization of observing time and schedule.

Yield results for the EXOSIMS case are shown in Figure 32. The EXOSIMS yield for metric A was 25.5 EECs characterized and 36.2 detected with atleast one imaging observation.

Additional narrative, explanation, and caveats of the plots will be added.

An important caveat to note is that the EXOSIMS yield results presented here were generated using the traditional exozodi value of 3 zodis for all stars, not the HOSTS exozodi data. This was due to an artifact of EXOSIMS' calculation of the integration time for the observation which uses the traditional exozodi. This is not realistic to an actual mission, because the exozodi level will be measured with the first imaging observation and can be used in the calculation of integration for future observations. Such a change is planned for upgrade to the EXOSIMS code was not incorporated in time for inclusion with these results. The impact of using an integration time naive of exozodi is shown in Figure 33. Subplot (a) shows the fraction of exo-earths detected to exo-earths present for the traditional case of 3 zodis. Subplot (b) shows the fraction of exo-earths detected to exo-earths present for the HOSTS exozodi data.

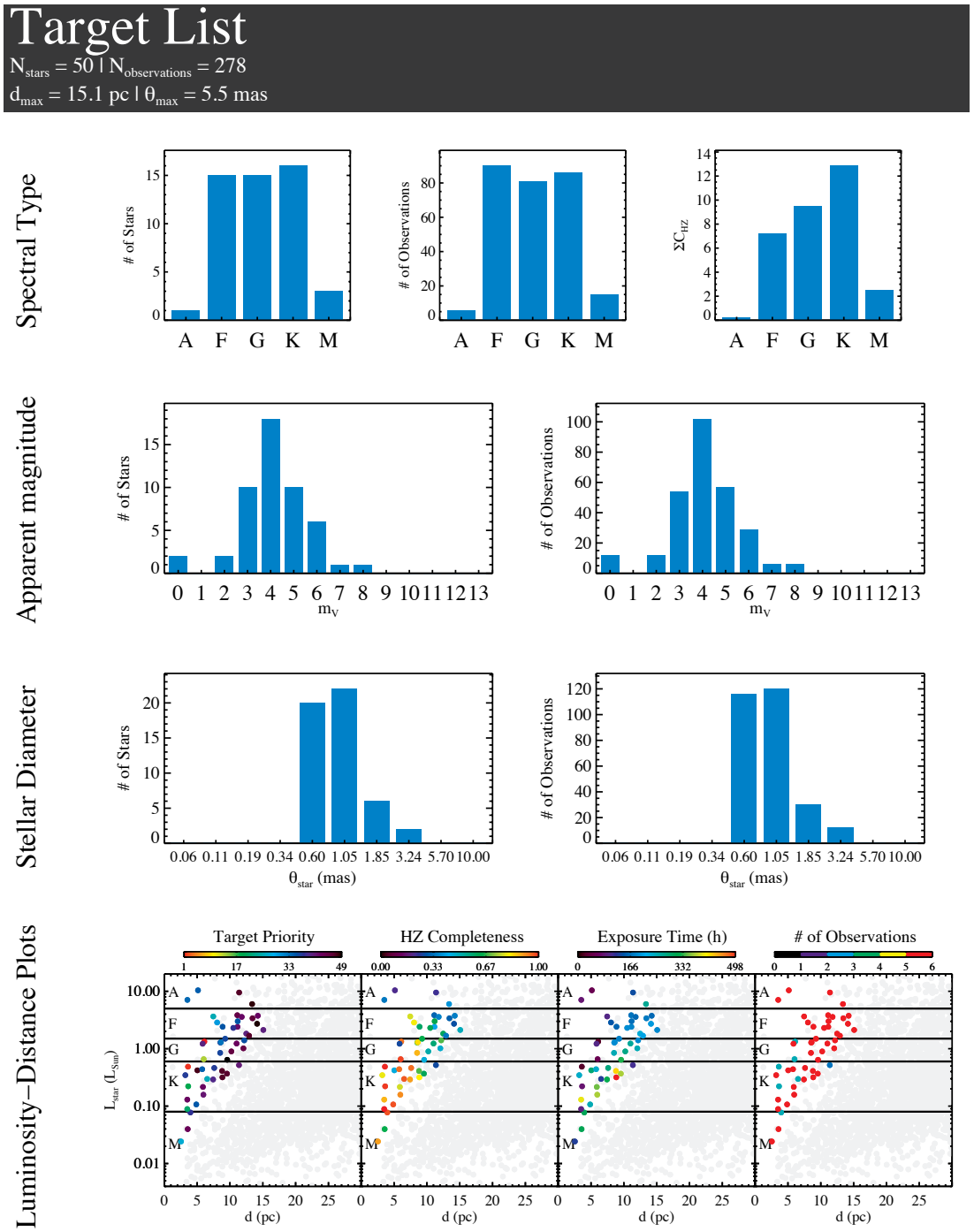

FIGURE 28. *Example distributions of the properties of target stars surveyed by HabEx during the prime mission, assuming a random exozodi draw from the nominal distribution of exozodi levels derived from LBTI. The exact number of stars surveyed depends on the exozodi levels drawn around each potential target. A total of ∼50 stars is expected to be surveyed: 8 during the deep survey (starshade only) and 42 during the broad survey (multi-epoch coronagraphic searches and planet orbit determination, followed by planet spectral characterization with the starshade). Based on the HabEx survey strategy, the upper-right panel shows the number of HZ Earthlike planets that would be characterized around stars of different types, assuming each star had one such planet.*

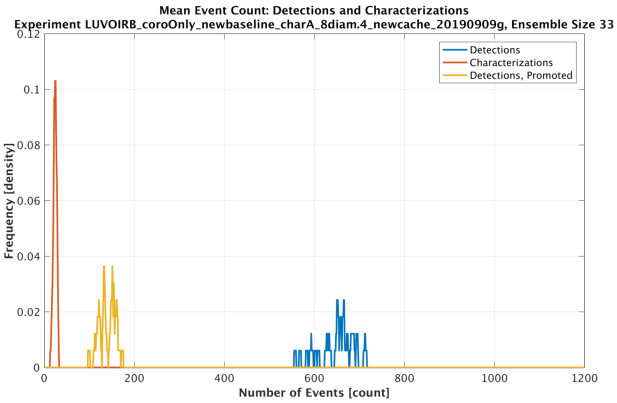

FIGURE 29. *Detections and characterizations for the LUVOIR B corongraph only scheduler. All plotted quantities are probability mass functions (histograms) for discrete event counts across an ensemble of 46 simulated universes and consequent observation sequences. The blue line shows the count of detection events for each simulated mission. The gold line shows how many of these detections were done on targets that were eventually promoted, and the red trace shows how many characterizations were actually performed.*

The fraction of exo-earths detected decreases to 65% - 95%, with only a few targets with 100% detection. This resulted in significantly fewer targets being promoted and an unreasonable decline in characterization yield. For these reasons, the EXOSIMS yield results reported for LUVOIR B and HabEx 4C coronagraph only utilize the traditional, non-HOSTS exozodi level. These reported yields are thus slightly optimistic.

AYO evaluated LUVOIR yield over a 2 year mission portion to metric A. An additional six months was allocated for full spectra of exo-earth candidates discovered and found to have water. The results presented here are for the yield on metric A.

Discussion and additional explanation of LUVOIR AYO results from the LUVOIR final report will be added here to provide context for the reader.

6.c. **HabEx 4C: Coronagraph Only.** The HabEx Coronagraph-only architecture ("HabEx 4C") uses the same observation scenario as the LUVOIR B scenario.

The same parameters for the HabEx coronagraph as adopted as before. For HabEx coronagraph-only observations, there is no UV capability (see HabEx final report p. 10-8), so the AYO yield cited in the HabEx Final report is for a broad band spectra from

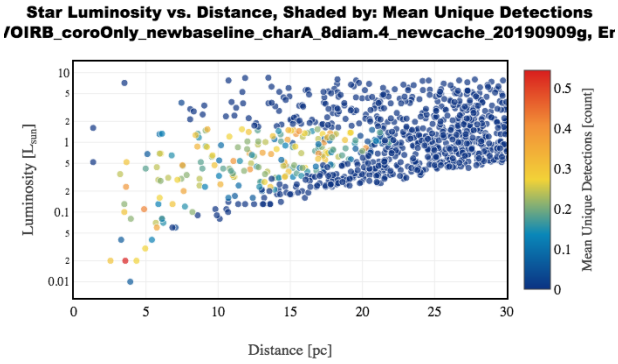

(a) *Detected exo-earths*

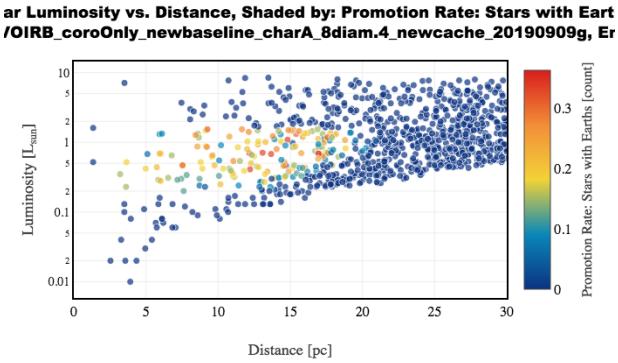

(b) *Promoted for characterization*

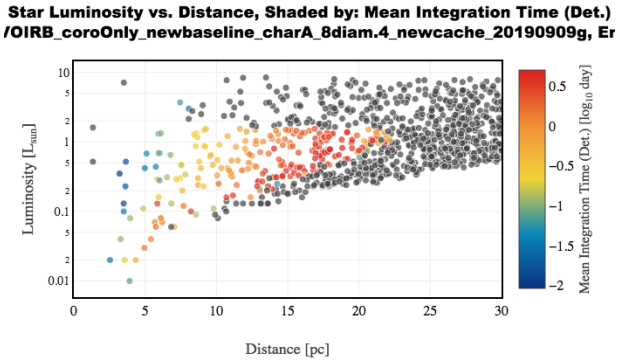

(c) *Mission time of first characterization observation*

FIGURE 30. *For LUVOIR B and spectra at the water line (metric A): (a) exo-earths that received at least one detection, (b) exo-earths candidates that meet the promotion criteria, (c) the targets with high completeness/integration time are observed early in the mission.*

450 nm to 1000 nm. The detection and characterization phase assumed 2.5 years of allocated time.

The AYO yield for metric C was 5 exo-Earths (HabEx final report Table 10.3-1, p. 10-10).

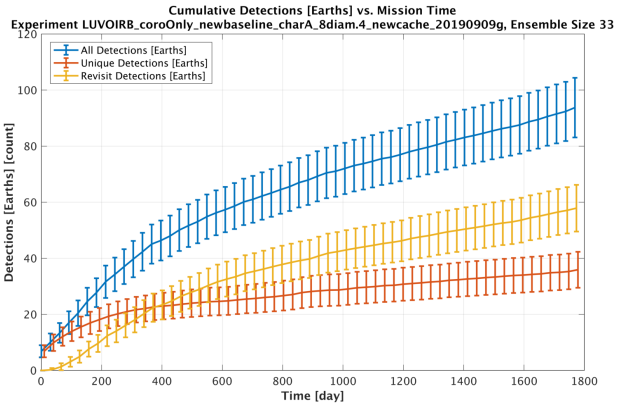

FIGURE 31. *Over the mission time, the unique detections declines as the target pool for the blind search progresses to longer integration time targets. Revisits begin after a wait period of one third of an orbit.*

EXOSIMS evaluated HabEx coronagraph only yield with metric D, a broad band spectra from 300 nm - 1250 nm. It was assumed that if a HabEx coronagraph only mission were to fly, a UV coronagraph would be included. The optical throughput used for the assumed UV coronagraph channel was the same as the throughput for the starshade UV channel, which may be slightly optimistic for a UV coronagraph. The spectral bands were observed in sequence. Consequently the total integration for metric D is higher than the integration time for metric C and the EXOSIMS yield numbers will appear lower than if metric C had been evaluated.

The EXOSIMS yield for metric D was 6.5 earths characterized and 13.5 earths detected with at least one imaging observation.

Additional narrative, explanation, and caveats of the plots will be added.

Observing time spent on blind search for targets late in the mission may not have sufficient time remaining for the epochs for orbit determination. These targets could be observed earlier in the mission by front loading the mission portion for exoplanets, or this observational time could be used for repeat characterizations at different epochs.

6.d. **HabEx 4S: Starshade Only.** The HabEx Starshade only case utilized the starshade for the blind search and the orbit determination. The characterization was taken immediately after the initial detection. Subsequent visits were used for detections for orbit determination. The revisit wait period of the coronagraph blind search was enforced, though a more optimal scheme could be developed

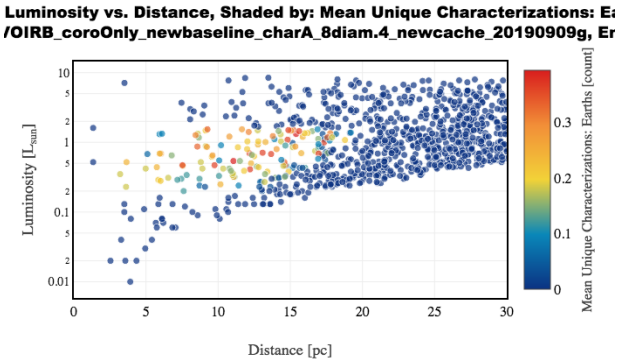

(a) *Characterized exo-earths*

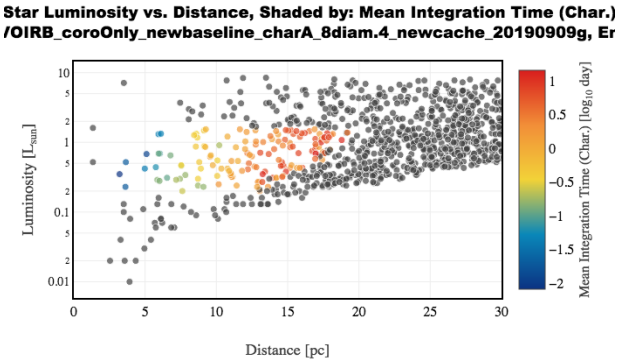

(b) *Characterization integration time*

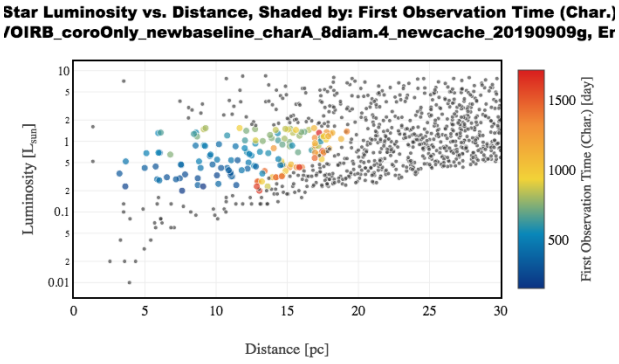

(c) *Mission time of first characterization observation*

FIGURE 32. *LUVOIRB Characterization yield: the high completeness targets are characterized early in the mission because they are promoted early in the mission.*

utilizing orbit information as the orbit fit evolved at each epoch.

This observing scenario subjected the starshade characterizations to the random phase of the exoplanet at initial detection. The benefit of orbit

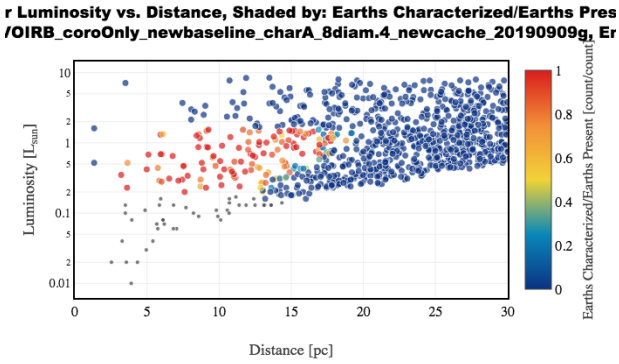

(a) *Fraction of exo-earths detected to exo-earths present for 3 zodis*

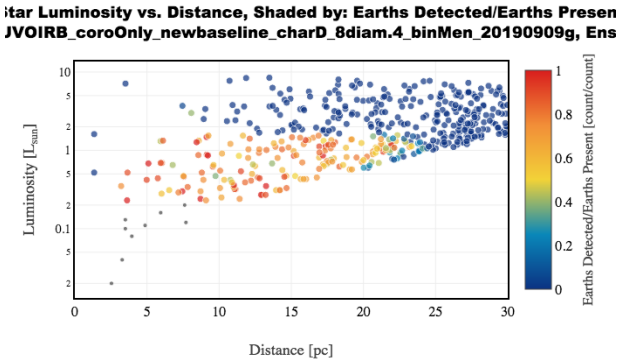

(b) *Fraction of exo-earths detected to exo-earths present for HOSTS nominal exozodi data fit.*

FIGURE 33. *The variation in exozodi generated by the HOSTS survey caused a lower fraction of exo-earths to be detected, even around high completeness stars. The top plot (3 zodis) was used for LUVOIR B.*

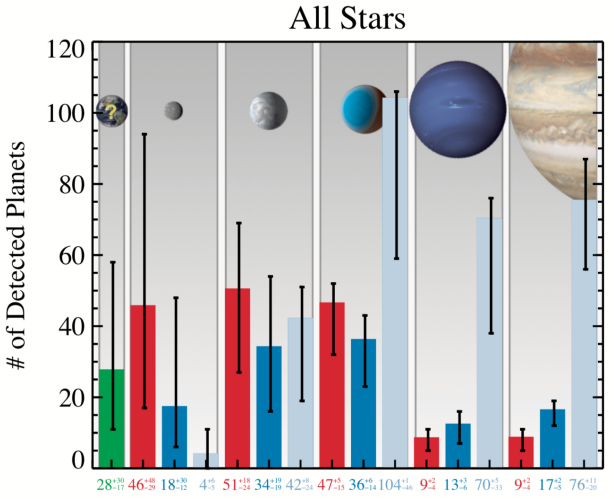

FIGURE 34. *AYO calculated a yield for LUVOIR B of 28 potential Earth analogs (green bar), 180 rocky planets, 190 sub-Neptunes, and 200 gas giants. Yield mean values and uncertainties for each planet type are indicated at the bottom of the plot.*

determination for a favorable phase could not be claimed. From Figure 45, the starshade characterization yield could be 25-50% of the yield when the explanet is at a favorable phase.

To more closely evaluate the impact of the random phase of the orbits, we return to the omniscient case in which all the exo-earths are promoted to for spectral characterization by the starshade on day 1 of the mission. This time, instead of placing the exo-earths at quadrature for the observation, the planet phase corresponds to its natural, propagated phase in the synthetic universe. The characterization yield drops from 27 earths (at quadrature) to 14.8 when observations are uncoordinated to the planet phase. In this scenario, multiple starshade observations of a target were permitted to increase the probability of a successful characterization (Figure 40; an average of 41.5 characterization attempts were made to acquire the 14.8 successful spectra. Once a successful characterization was achieved, the target was retired. For the scenario in which only a single observation permitted, the average yield was 13 exo-earths.

Now that impact is understood of the observation uncoordinated to the planet phase, the HabEx Starshade Only scenario is discussed. In the observing scenario, the starshade performs a blind search in detection mode, which is imaging over a 450-1000 nm bandpass. As soon as an exo-earth is detected in imaging mode, a spectral characterization is taken immediately, as long as sufficient time remains in the observable window. Immediate characterization ensures that a spectrum is acquired before the exoplanet can propagate to an unfavorable, and possibly unknown, position at the next epoch of potential starshade observation.

Follow up observations are made in imaging mode at two to three more epochs to determine the orbit of the exo-earth to be able to classify it in the habitable zone or not. This is a change from the observing scenarios for the coronagraph and the coronagraph/starshade hybrid in which the agility of the coronagraph allowed for frequent, lightly constrained imaging observations and the

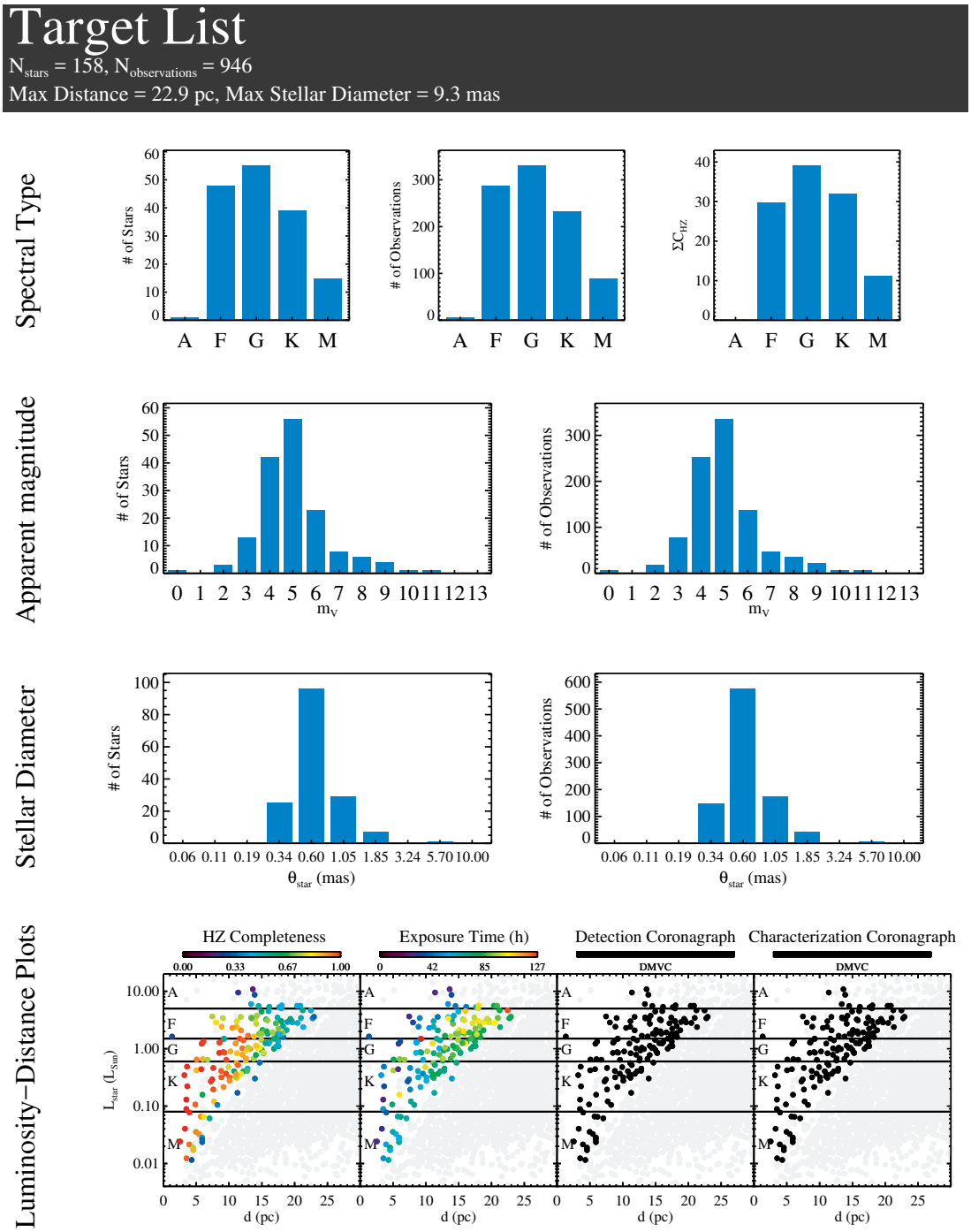

FIGURE 35. *Example list of target stars surveyed by LUVOIR B during the prime mission, assuming a random exozodi draw from the nominal distribution of exozodi levels derived from LBTI. The exact number of stars surveyed depends on the exozodi levels drawn around each potential target. The upper-right panel shows the number of HZ Earthlike planets that would be characterized around stars of different types, assuming each star had one such planet.*

orbit could be determined at least cost of observing time and mission resources than the spectral characterization. In the starshade only scenario, the orbit characterization is performed as a follow-up to the spectra. In observation scheduling, this results in more exoplanets being spectrally characterized than

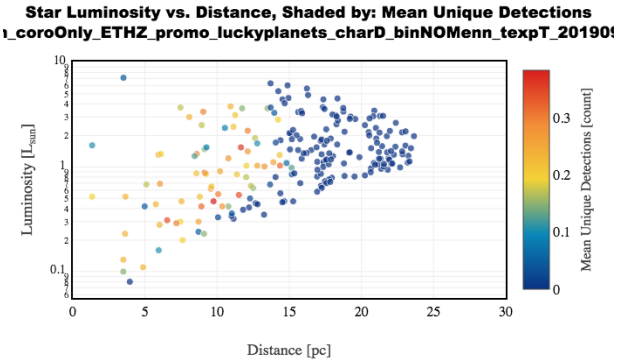

(a) *Detected exo-earths*

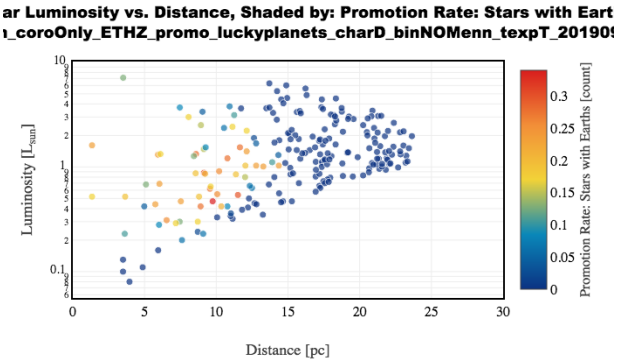

(b) *Promoted for characterization*

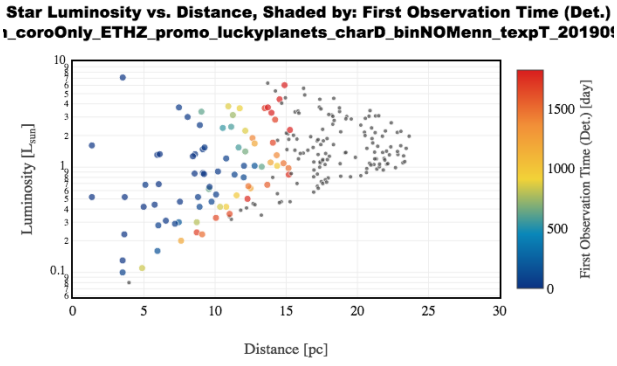

(c) *Mission time of first characterization observation*

FIGURE 36. *HabEx 4C coronagraph-only (a) exo-earths that received atleast one detection, (b) exo-earths candidates that meet the promotion criteria, (c) The targets with high completeness/integration time are observed early in the mission.*

having their orbits determined.

There is some artificiality in the execution of this scenario in EXOSIMS. For the yield results reported

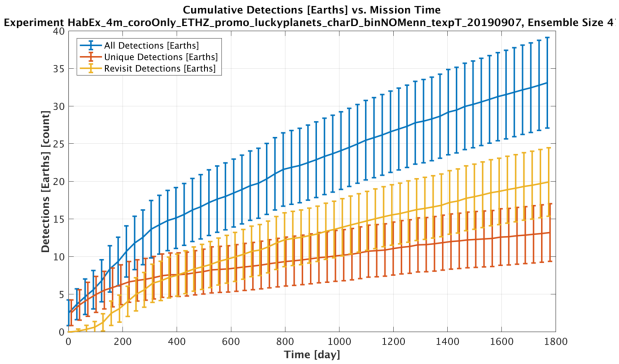

FIGURE 37. *HabEx 4C coronagraph-only: over the mission time, the unique detections declines as the target pool for the blind search progresses to longer integration time targets. Revisits begin after a wait period of one third of an orbit. Characterizations begin after targets are promoted.*

here and in the summary table, a planet population of only exo-earths was used, and thus every spectral characterization was of an exo-earth and all followup detection observations were of earths. While EXOSIMS is capable of synthesizing the continution Dulz-Plavchan-SAG13 planet demographic population, the non-exo-earths provide confusion, particularly in multi-planet systems. In multi-planet systems, the "successful characterization" may be of non-exo-earth and the three additional epochs for orbit determination could contain "successful detections" of any of the planets in the system. An additional approach is needed to distinguish the planets from one another in a multi-planet system. One approach is to acquire a low resolution spectra (of significantly shorter integration time than the full spectra) for coarse characterization which could be sufficient to fingerprint the planet and repeatedly identify all the planets in the system at multiple epochs. This is a topic for further research. For the simplicity of these yield simulations, an exo-earth only population was used to assess a scenario free from confusers.

The EXOSIMS yield results are shown in Figure 39. In the starshade only scenario, the characterization preceeds the orbit determination, and so a favorable exoplanet phase is not assumed. As a result, the yield is below the occurrence for exo-earths. The Mission Elapsed Time plot shows that the high completeness stars are characterized early in the mission, while the stars on the edge of sensitivity are visited late in the mission. The fraction of exo-earths characterized to exo-earths present is close half for

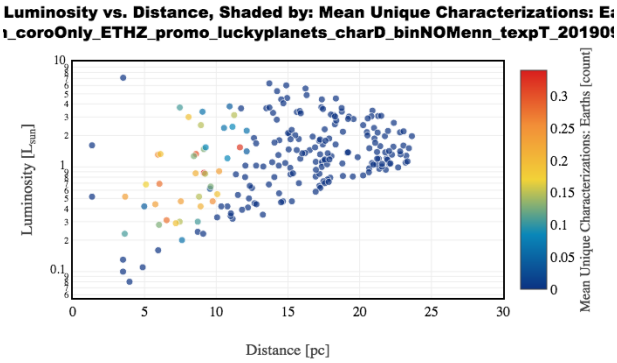

(a) *Characterized exo-earths*

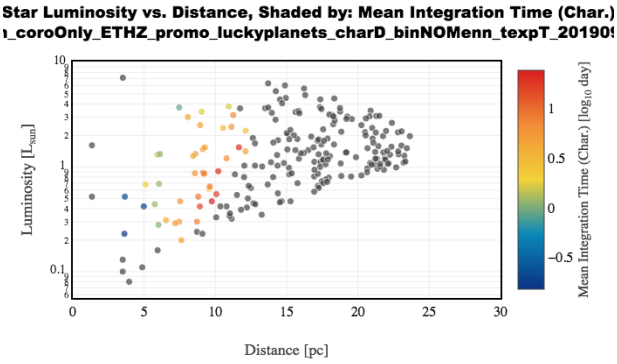

(b) *Characterization integration time*

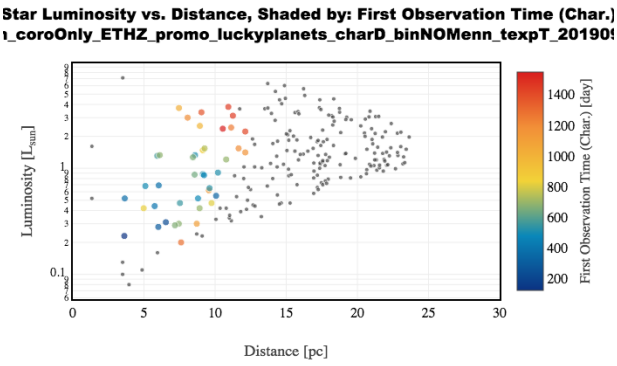

(c) *Mission time of first characterization observation*

FIGURE 38. *HabEx 4C coronagraph only: All of the targets promoted by the coronagraph are spectrally characterized. The high completeness targets are characterized early in the mission because they are promoted early in the mission.*

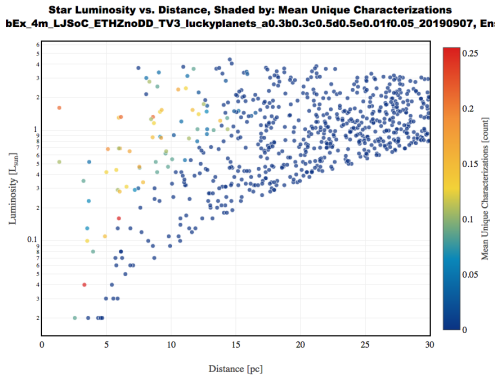

(a) *Characterized exo-earths*

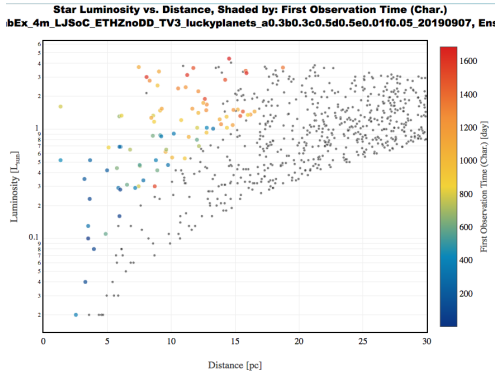

(b) *Mission elapsed time of first characterization observation*

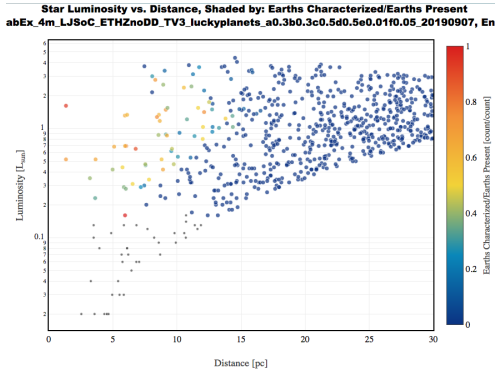

(c) *Fraction of exo-earths characterized to exo-earths present.*

FIGURE 39. *HabEx 4S starshade-only (a) The characterized earths are high completeness as they are discovered with blind search by the starshade which has a limited number of observations.*

most of the stars observed; this is due to the lack of orbit knowledge of the exo-earth.

EXOSIMS evaluated the number of exo-earths detected to be 10.2 and the number of exo-earths characterized to be 6.1. Of these, only 2.5 exo-earths achieved orbit determination.

AYO evaluated the yield for the HabEx 4 m starshade only case as part of the HabEx architecture comparison. The metric for that case used R=70,

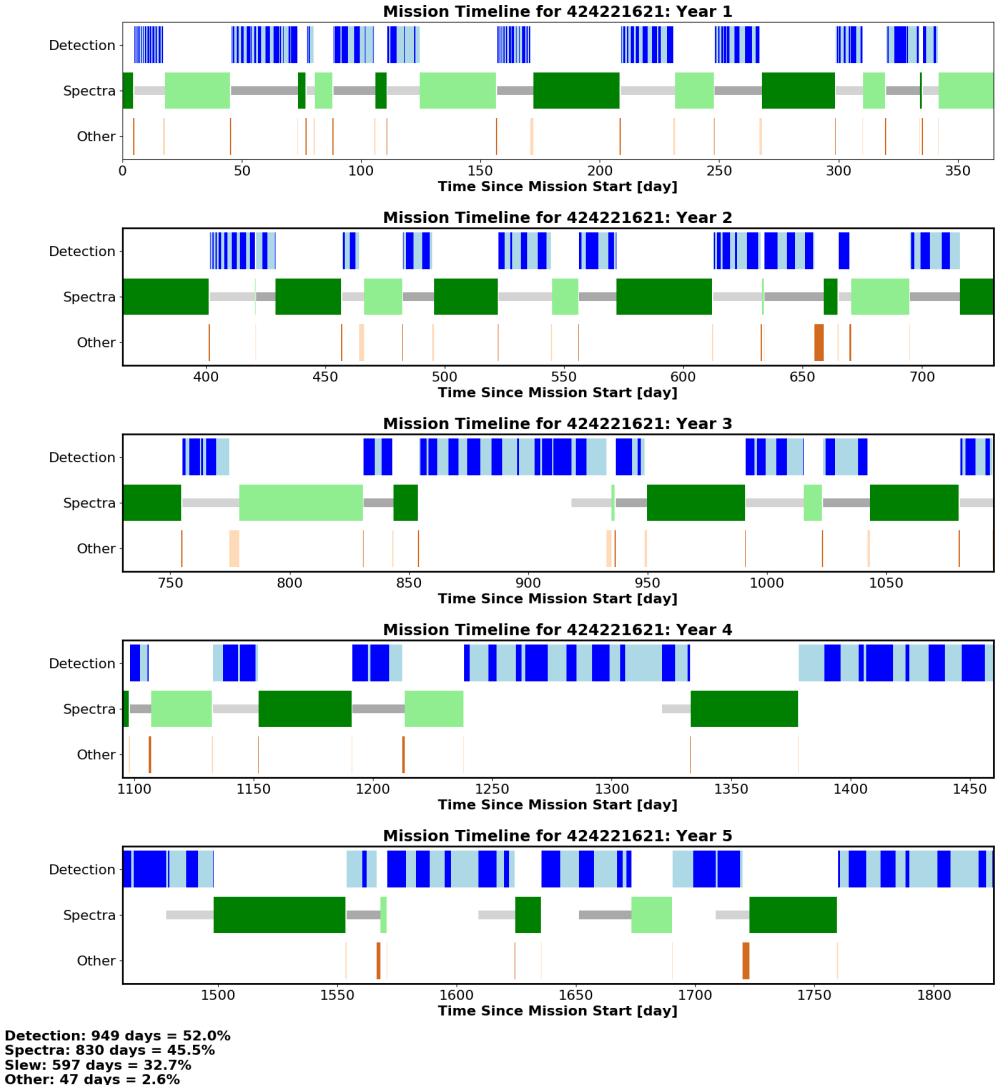

FIGURE 40. *The observation timeline for a scenario in which all of the exo-earths are known on Day 1 of the mission, but the characterization observation epoch is uncoordinated with exo-earth phase. Multiple starshade visits to the same target were allowed.*

instead of R=140 as in the HabEx baseline scenario and the EXOSIMS evaluation for the starshade only. AYO calculated a yield of 5 EECs; the AYO evaluation includes characterization and at least four imaging detections.

6.e. **Comparison Summary.** While the AYO results have been previously detailed in the HabEx and LUVOIR final reports, the EXOSIMS results are presented for the first time in the previous sections. A summary of the yield results from AYO and EXOSIMS are summarized in Table 6.

The summarized results are tailored to the results presented in the mission concept study final reports. LUVOIR B was evaluated for a 20% bandwidth spectra to search for the water line feature at 940 nm (metric A, §4). EXOSIMS evaluated both LUVOIR B and HabEx 4C coronagraph only to allow for a side by side comparison. HabEx achieved about half the metric A yields as LUVOIR B. The EXOSIMS and AYO results were close, with caveats discussed in greater detail in the LUVOIR B results section.

The three HabEx architectures were compared in Chapter 10 of the HabEx final report using AYO. The full spectra yield values in the summary table

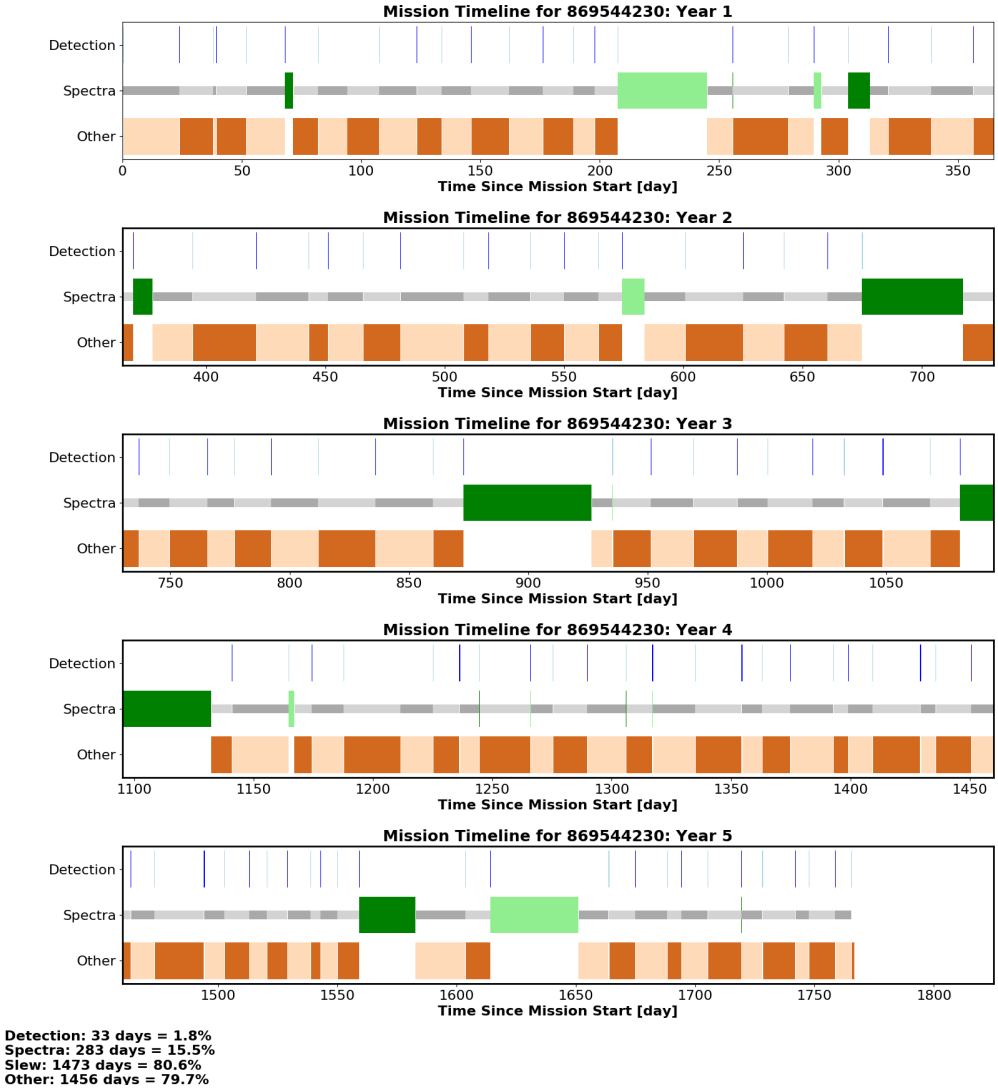

FIGURE 41. *The starshade only scenario uses the starshade for blind search, spectral characterization, and follow-up detections for orbit determination. The slews preceeding detection observations are still shown in the "spectra" row. The detection observations with the starshade are shown in blue, while spectral characterizations are shown in green on the "spectra" row. Telescope time during slews is used for the "other" timeline shown in brown, such as the UV Spectrograph or the Work Horse Camera, which receives ∼80% of the mission time.*

are for full broadband spectra from 450 nm - 1000 nm (metric C).

What we have learned from the results, summarized in the table and detailed below, and from scheduling mission observations, is that the blind search by coronagraphs is costly with respect to the baseline mission timeline and cannot achieve the omniscient upper bound, largely due to the fact that observations on higher integration time targets are initiated too late in the mission to allow for the epochs necessary for orbit determination. A higher yield should be achievable by front-loading the exoplanet observation portion of the mission.

We have also learned that the starshade blind search is not as inefficient as one might expect. The HabEx starshade-only scenario achieved nearly as many full spectra as the coronagraph-only scenario. The starshade-only scenario did have difficulty achieving follow-up detection observations for orbit determination of all of the spectrally characterized

Table 6. *A comparison of yield of spectral characterization of Earthlike planets for full spectra and partial spectra at the 940 nm water line. Also evaluated by EXOSIMS was the upper bound of an omniscient case in which all EECs were known and characterized at quadrature.*

	Water line, Metric A			Broad spectra, Metric C1			Broad spectra, Metric C2		
Architecture	AYO	EXOSIMS	Omni	AYO	EXOSIMS	Omni	AYO	EXOSIMS	Omni
HabEx 4H	–	9	29	8	5	9	8	7	17
LUVOIR A	54	–	50	–	–	–	–	–	–
LUVOIR B	28	18	28	–	4	6	–	7	10
HabEx 4C	–	6	12	–	2	3	5	3	5
HabEx 4S	–	3	18	–	3	9	5	3	13

targets.

We see that HabEx is target starved but can return a significant number of fully characterized EECs with orbit determination.

Appendix A. EXOSIMS and AYO comparison

A.a. **Common Physical Assumptions.**

A.a.i. *Integration Time Calculation.* AYO and EXOSIMS use different integration time equations. The EXOSIMS integration time calculation is based on the formalism developed by Nemati and Krist, that allows for an asymptotically increasing integration time as the noise floor is reached.

both equations will be inserted here and respective papers cited.

A.a.ii. *Comparison of Count Rates.* Table 7 shows a comparison of integration times and individual count rates between the EXOSIMS and AYO codes for a number of representative stars of varying magnitude. Despite different implementations and model assumptions, the two codes typically agree on all integration times to within 50%. The most important differences between the two are:

- EXOSIMS does not currently include variation in the instrument PSF and performance as a function of stellar diameter, which accounts for the majority of the differences in the stellar residual term (C_{sr})
- EXOSIMS employs a slightly different interpolation of the local zodiacal flux term from the Lienert data than AYO, accounting for the differences in C_z
- EXOSIMS employs an empirical scaling model for exozodi based on observed local zodi variation, as explained in §3.a.v, accounting for the differences in the Cez term
- AYO uses a variable, optimized frame time, unlike EXOSIMS's static time, which accounts for the variation in the C_{cc} term.

A.b. **Observing Constraints.**

A.b.i. *Keepout Constraints.* One of the most important (and difficult to capture in simulation) constraints on imaging missions are the keepout regions imposed on the observatory by the scattered light requirements of the high contrast instrumentation. The most important keepout regions, shown schematically in Figure 42, for observatories in Sun-Earth L2 orbits, are due to the Sun, Earth and Moon, all of which lie in approximately the same (but not exactly overlapping) regions of space with respect to the observatory in the rotating frame.

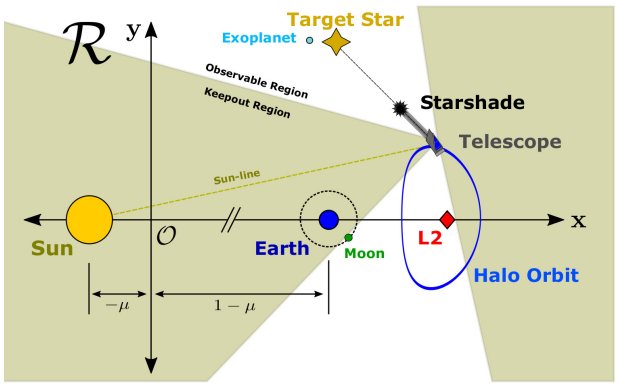

Figure 42. *Schematic representation of observatory keepout regions (due only to the Sun) in the Sun-Earth rotating frame ($\mathcal{R}$). The $\mathbf{x}-\mathbf{y}$ plane is the ecliptic and orbits of the Moon and the observatory's halo orbit about the Sun-Earth L2 point are shown projected in this plane. The starshade lies along the telescope-star "look vector". Targets whose look vectors fall within the shaded regions are excluded from observations at this time due to solar keepouts. From Soto et al. (2019).*

As the observatory's nominal orbit (assumed in this case to be a fully periodic halo about the Sun-Earth L2 point) typically has a large (several hundred thousand kilometer) extent in the direction orthogonal to the ecliptic, the angles between the telescope, Sun, Earth and Moon are sufficiently different at times that one of these objects may scatter light into the telescope pupil even while the other two are outside of their respective keepout regions. The presence of a starshade further complicates things by introducing the possibility of back-scatter of sunlight reflected off of the external occulter back into the telescope pupil (reflection due to illumination by the Earth and Moon is less of a concern, as they would be near 180° phase with respect to the starshade and Sun in these cases).

We can thus parameterize the observable region due to each illuminant with a single pair of angles, $\alpha_{\text{min}}^{(\text{object})}$, $\alpha_{\text{max}}^{(\text{object})}$ such that the observable region for a given target star i at a particular point in time is given by the intersection of all of the individual-illuminant observable zones:

$$\bigcap_{\text{objects}} \alpha_{\text{min}}^{(\text{object})} \leq \cos^{-1}\left(\hat{\mathbf{r}}_{i/\text{SC}} \cdot \hat{\mathbf{r}}_{\odot/\text{SC}}\right) \leq \alpha_{\text{max}}^{(\text{object})}$$

where $\hat{\mathbf{r}}_{i/\text{SC}}$ is the unit vector from the spacecraft to the target and $\hat{\mathbf{r}}_{\odot/\text{SC}}$ is the unit vector from the spacecraft to the Sun. In addition to the Sun, Earth, and Moon, we can also consider scatter from other solar system objects. As these are

Table 7. *Integration time calculation comparison between EXOSIMS and AYO codes for a number of representative target stars.*

Target	Distance (pc)	L ($L_\odot$)	Vmag	EEID	ΔMag	C_{p0} (s^{-1})	C_b (s^{-1})	C_{sr} (s^{-1})	C_z (s^{-1})	C_{ez} (s^{-1})	C_{cc} (s^{-1})	Int. Time (d)
EXOSIMS												
HIP 105090	3.9500	0.0800	6.6900	0.0816	22.0992	0.0816	0.1599	0.0046	0.0159	0.0400	0.0049	0.0186
HIP 15457	9.1400	0.8800	4.8400	0.1026	24.7027	0.0554	0.2312	0.0390	0.0178	0.0448	0.0038	0.0446
HIP 17651	17.6300	5.3900	4.2200	0.1317	26.6704	0.0190	0.2915	0.0819	0.0188	0.0472	0.0013	1.0847
HIP 19849	4.9800	0.4200	4.4300	0.1301	23.8996	0.1735	0.4489	0.0583	0.0187	0.0471	0.0120	0.0086
HIP 2021	7.4600	3.7000	2.8200	0.2578	26.2620	0.1059	0.9992	0.3135	0.0204	0.0512	0.0073	0.0694
HIP 23693	11.6500	1.5400	4.7100	0.1065	25.3103	0.0382	0.2280	0.0471	0.0180	0.0452	0.0026	0.0955
HIP 68184	10.0600	0.3300	6.4900	0.0571	23.6378	0.0201	0.0830	0.0053	0.0143	0.0360	0.0014	0.1293
HIP 95149	18.8300	0.8200	6.4800	0.0481	24.6260	0.0081	0.0604	0.0053	0.0128	0.0322	0.0006	0.6135
HIP 98036	13.7000	6.2900	3.7100	0.1831	26.8381	0.0239	0.3981	0.3006	0.0197	0.0495	0.0016	1.7824
AYO												
HIP 105090	3.9709	0.0874	6.6900	0.0801	22.0635	0.0623	0.0487	0.0109	0.0122	0.0201	0.0056	0.0233
HIP 15457	9.1457	0.8720	4.8400	0.1021	24.6927	0.0504	0.1530	0.0535	0.0156	0.0894	0.0045	0.0897
HIP 17651	17.6378	5.2869	4.2200	0.1304	26.6495	0.0178	0.2289	0.1161	0.0103	0.1008	0.0017	0.8544
HIP 19849	5.0361	0.4204	4.4300	0.1287	23.9005	0.1547	0.1781	0.0803	0.0125	0.0817	0.0136	0.0121
HIP 2021	7.4588	3.6453	2.8200	0.2559	26.2458	0.0982	0.5670	0.4546	0.0090	0.0948	0.0087	0.0825
HIP 23693	11.6247	1.4993	4.7100	0.1053	25.2812	0.0357	0.1668	0.0653	0.0076	0.0906	0.0032	0.1641
HIP 68184	10.0878	0.3177	6.4900	0.0559	23.5964	0.0181	0.0572	0.0086	0.0065	0.0404	0.0017	0.2296
HIP 95149	19.8861	0.8924	6.4800	0.0475	24.7179	0.0069	0.0836	0.0070	0.0125	0.0635	0.0007	2.0864
HIP 98036	13.3755	5.9940	3.7100	0.1830	26.7858	0.0225	0.7011	0.6143	0.0136	0.0812	0.0021	1.5957
Factional Difference												
HIP 105090				0.0215	0.0016	0.1296	0.6954	-1.3756	0.2362	0.4985	-0.1312	-0.2554
HIP 15457				0.0052	0.0004	0.0911	0.3380	-0.3710	0.1237	-0.7731	-0.1831	-0.7855
HIP 17651				0.0101	0.0008	0.0651	0.2147	-0.4170	0.4513	-1.1374	-0.2759	0.2123
HIP 19849				0.0107	-0.0000	0.1084	0.6032	-0.3781	0.3345	-0.5229	-0.1386	-0.4078
HIP 2021				0.0076	0.0006	0.0831	0.4325	-0.4502	0.5599	-0.8502	-0.1896	-0.0453
HIP 23693				0.0112	0.0011	0.0657	0.2682	-0.3873	0.5757	-1.0059	-0.2308	-0.7194
HIP 68184				0.0206	0.0017	0.0996	0.3099	-0.6286	0.5470	-0.1232	-0.2288	-0.7763
HIP 95149				0.0122	-0.0037	0.1485	-0.3832	-0.3125	0.0256	-0.9731	-0.2665	-2.4010
HIP 98036				0.0001	0.0020	0.0584	-0.7611	-1.0435	0.3105	-0.4381	-0.2643	0.1047
Mean				0.0110	0.0005	0.0933	0.1909	-0.5960	0.3516	-0.5917	-0.2121	-0.5637

significantly fainter, it is typically not expected that they should cause any off-axis scatter issues, and so their keepouts are defined solely to keep them out of the observatory's actual field of view. However, if subsequent analysis reveals that brighter objects such as Jupiter or Venus can potentially affect contrast off-axis, they too will need to be included in the keepout calculations.

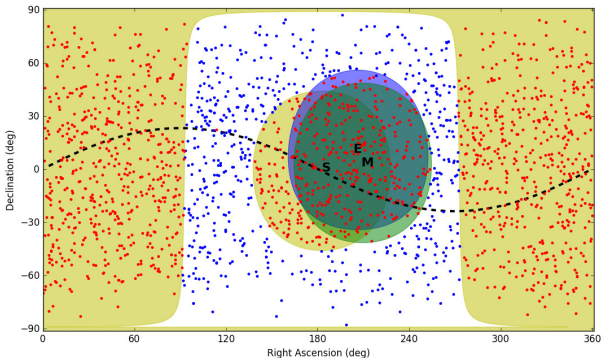

Figure 43. *Schematic view of solar system keepout regions viewed from a spacecraft-centered frame, plotted in equatorial coordinates. The three central shaded regions represent annuli (equal to the same $\alpha_{min}^{(object)}$) about each of the Sun, Earth and Moon (labeled, S, E and M, respectively), and the exterior shaded region represents the additional solar keepout due to the presence of a starshade. Points represent target stars, with blue points corresponding to targets that are currently observable. The dashed line represents the ecliptic plane.*

Figure 43 shows a view of the keepouts due to the Sun, Earth and Moon, each corresponding to a 45° exclusion zone about the line of sight, as well as a starshade keepout of 180° centered about the anti-solar point. The coordinates in this case are equatorial, and sample target stars are shown to give a sense of the fraction of targets that are unavailable at any given time in the mission. This schematic also makes it clear that even though these keepouts are mostly overlapping, each also includes a non-overlapping region of space, making it important to keep track of the positions of all three throughout the mission simulation.

In addition to the keepouts imposed by bright solar system objects, additional keepout restrictions may be needed due to solar panel pointing requirements. We can consider the case of an observatory with fixed solar panels mounted along half of the telescope barrel, in parallel to the boresight direction. To prevent excessive shadowing of the solar panels during observatory operations, there will typically be yaw, pitch and roll restrictions in the observatory's body frame, which can be translated to minimum and maximum allowable angles between the boresight and the observatory-sun line. This makes these restrictions fully compatible with the $\alpha_{\rm min}^{(\rm sun)}, \alpha_{\rm max}^{(\rm sun)}$ parameterization described above. In EXOSIMS, solar panel keepouts replace the sun keepout angles when they are more restrictive, and are ignored otherwise.

Fixed, aft-mounted solar panels (such as JWST's) typically increase solar keepouts (boresight must point near the anti-solar point), while side-mounted panels (such as WFIRST's) create keepouts similar to those due to starshades. The only case where solar panels do not induce additional keepout restrictions on an imaging mission is when the observatory carries either articulable or highly redundant solar panels, allowing for the spacecraft to roll freely about the sun-pointing vector.

Finally, it is important to remember that for missions carrying multiple different starlight suppression systems, each system may have different keepouts. This is particularly true in cases where a mission uses both an internal coronagraph and an external starshade to make various observations. The starshade will typically have significantly stricter keepout restrictions, meaning that it will generally be more difficult to schedule observations for the starshade, and this must be taken into account in mission simulation and execution.

EXOSIMS deals with this by generating cached keepout maps for each starlight suppression system in each simulated mission scenario. An example of one such set of maps, for the case of a coronagraph and starshade on one mission, is shown in Figure 44.

A.b.ii. *Dynamic Observation Scheduling.* One of the strengths of the full mission simulation approach employed by EXOSIMS is the ability to explicitly model how the early results of a mission can impact the execution of the rest of the mission. This is particularly important in cases where followup observations are required after initial detections in order to confirm and further characterize a planet candidate. Since EXOSIMS continuously recalculates its observing plan after each observation is completed (see §5.b.i), this gives us the opportunity to schedule

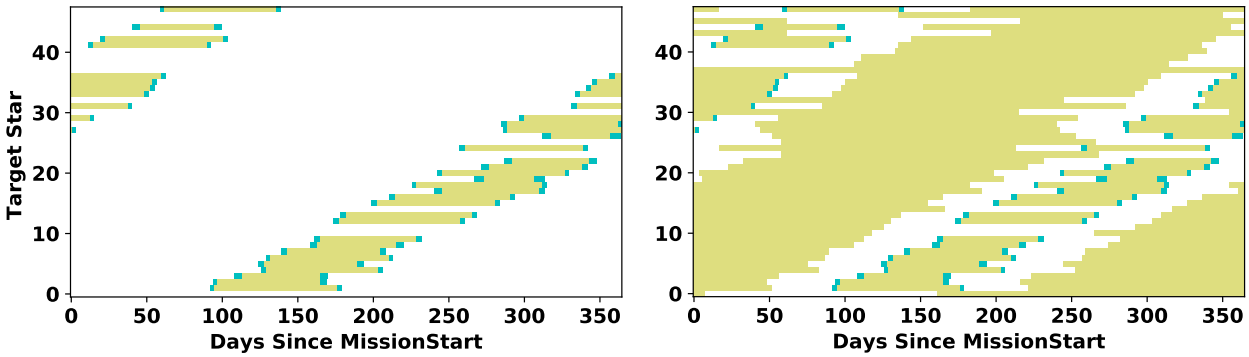

Figure 44. *Sample keepout maps for HabEx coronagraph (*left*) and starshade (*right*) for a subset of target stars during the first year of the mission. Blank regions correspond to times when a target is observable, yellow regions represent keepouts due to the sun, and other colored regions correspond to keepouts due to the Earth, moon or solar panel pointing restrictions. The targets are sorted by RA, which gives the overall structure to the plots, but effectively random in declination, such that neighboring targets can have very different observable periods. The right-hand plot clearly shows how much more difficult it is to schedule starshade observations than coronagraph ones.*

subsequent observations of various targets. Figure 45 illustrates the importance of dynamic scheduling to account for the key observational constraints of solar system keepout (which is readily predictable, but is a significant constraint, especially on starshade observations) and exo-system planet phase (which is only predictable after orbit determination). In the illustrated case (similar to Fig. 44), solar system keepout removes over 50% of characterization observing windows, while exosystem planet phase removes a somewhat smaller portion. The two constraints operate largely independently, so that the compound observing constraint is roughly the product of the individual components. This situation also underscores the importance of the orbit determination problem to increase the probability of scheduling characterization time within high-SNR observing windows.

There are multiple strategies for observation rescheduling. By default, the prototype Survey Simulation implementation reschedules targets where no planet is detected for re-observation at three quarters of the mean orbital period of the population of interest after the initial null detection (however, such followups are not highly prioritized, as it is typically better to observe a new target). In cases where a planet candidate is identified, the default logic schedules a mean observation for one half of the estimated period of the candidate. This period is calculated from the approximated mass of the target star (from its luminosity via empirical mass-luminosity relationships as in Henry and McCarthy Jr. (1993)), and by assuming that the observed projected separation is the planet's semi-major axis. The projected separation at first observation is actually the maximum likelihood estimator for the semi-major axis, but this estimate can carry very high errors, depending on the exact population of planets being modeled.

A.b.iii. *Exozodiacal Light Assumptions.*

A.b.iii.1. **AYO.**

A.b.iii.2. **EXOSIMS.** While EXOSIMS assumes a constant exozodiacal brightness (in number of local zodis) for each target when calculating integration times for initial detection observations, in calculating the actual SNR of each simulated observation, the exozodical light contribution is updated to reflect the true (assumed unknown) inclination of the target exosystem. The exozodi term is scaled by a factor:

$$f(I) = 2.44 - 0.0403I + 0.000269I^2 \quad (4)$$

where I is the target star system's inclination in degrees. This equation, first used by Don Lindler in his imaging simulations, is based on an empirical fit to the exozodi variation with inclination in the solar system (see Savransky, Kasdin, and Cady (2010) for further details).

EXOSIMS does not assume that exozodi values are determined from these observations, and continues to use the original exozodi assumptions when establishing integration times for all subsequent observations. If a mission concept assumes that exozodi levels can be established from the initial observation,

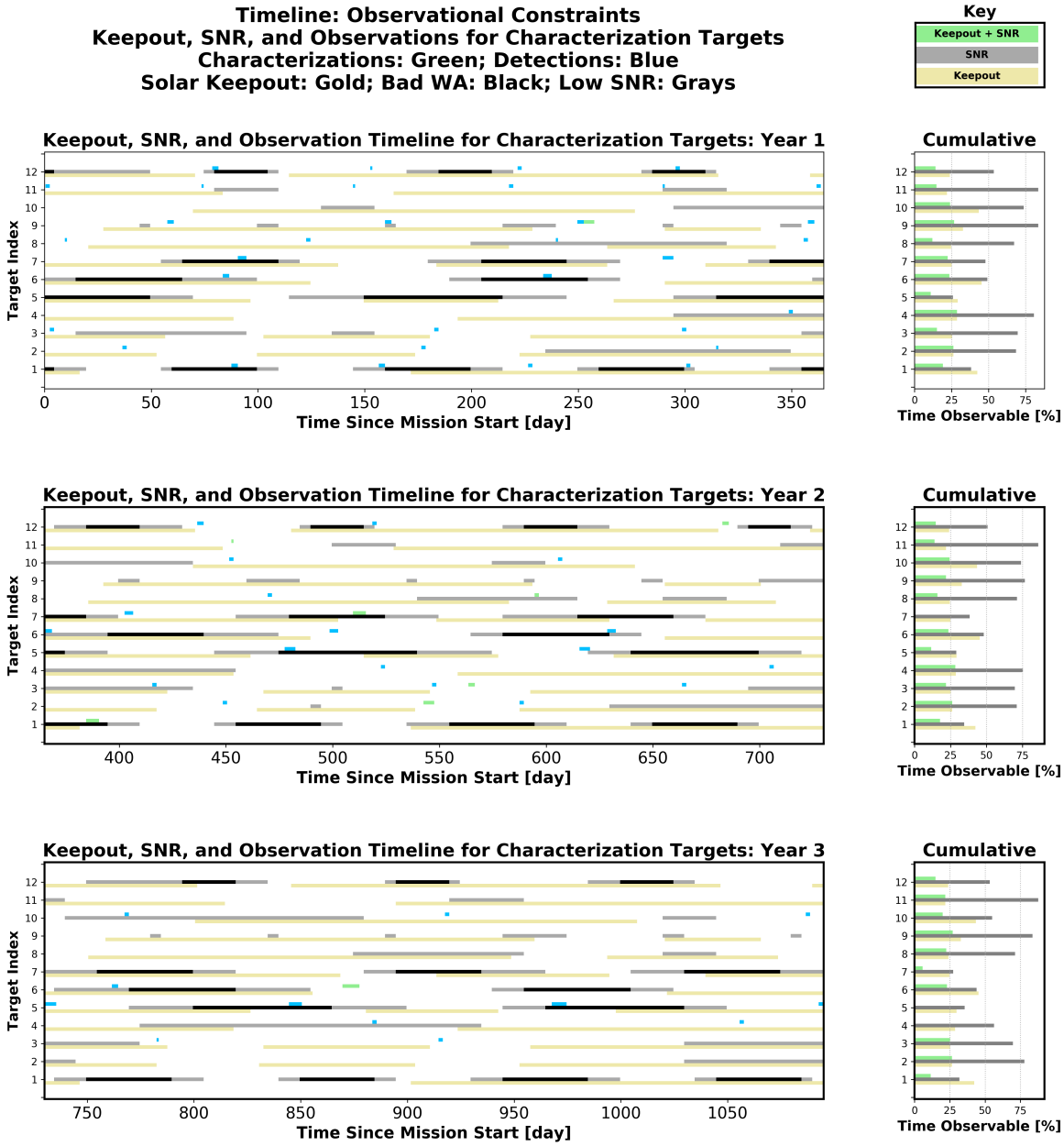

FIGURE 45. *Observing constraints due to solar system keepout and exosystem planet phase for a HabEx starshade scenario. The vertical axis shows a subset of target stars containing Earth twins. Blank regions correspond to times when a target is observable, while yellow stripes represent solar system keepout (Sun, Earth, Moon, and bright planets). Another stripe shows observing constraints due to working angle of the Earth twin in the exo-system. In black regions, the working angle is below the inner working angle (for this starshade, 43 mas at 5% transmission), while in gray regions, the SNR is insufficient for characterization (below 10). Detection observations are shown as small blue blocks, and attempted characterizations as green blocks. The right-hand bar charts summarize observability as a percentage of days in the year: larger numbers are better. The lower (yellow) bar shows the portion of time solar keepout constraints are satisfied, the middle (gray) bar shows the same for exo-system phase constraints, and the upper (green) bar shows the intersection of the two constraints. The intersection can be empty for an entire year (year 2, target 7; year 3, targets 4 and 5).*

the framework can be modified to update internal bookkeeping of exozodi as the mission progresses.

A.b.iv. *Starshade Slew Calculations.*
A.b.iv.1. **AYO.** The calculation of slew and fuel use with AYO is detailed in Stark et al. (2016b). An average slew time and fuel use is calculated and applied for each starshade slew.

A.b.iv.2. **EXOSIMS.** When simulating mission concepts including starshades, it is vital to model starshade slewing between targets and stationkeeping on target during observations. While slew times can be coarsely approximated by assuming an average slew duration for all transitions, there is no way to accurately represent the fuel use associated with these slews without actually modeling the relevant dynamics. It is incredibly important to have a running estimate on fuel use throughout the mission simulation as poor choices of slews can lead to early mission termination due to premature expenditure of volatiles on board the starshade.

Starshade dynamics in the vicinity of Sun-Earth L2 point orbits are explicitly non-Keplerian (as the very existence of the Lagrange points requires treating at least three bodies) and therefore require solutions in the three or four body system of the starsahde, Earth, Sun (and, if more exact solutions are required, the moon). Modeling the exact slew dynamics for each of the many thousands of transfers required to generate one EXOSIMS simulation ensemble would be prohibitively computationally expensive, so we need a good slew model that can approximate fuel use with low computational effort. We achieve this by parameterizing the space of slews by a small number of variables, solving the exact problem over a grid of these elements, and then generating an interpolant for use in subsequent slew calculations.

Following Soto et al. (2018, 2019), we define the equations of motion for the starshade as:

$$\ddot{x} - 2\dot{y} = \frac{\partial \Omega}{\partial x} + \mathbf{f}_{SRP} \cdot \hat{\mathbf{x}}, \tag{5}$$

$$\ddot{y} + 2\dot{x} = \frac{\partial \Omega}{\partial y} + \mathbf{f}_{SRP} \cdot \hat{\mathbf{y}}, \tag{6}$$

$$\ddot{z} = \frac{\partial \Omega}{\partial z} + \mathbf{f}_{SRP} \cdot \hat{\mathbf{z}}, \tag{7}$$

where x, y, z are Cartesian coordinates describing the starshade's center of mass in the rotating frame $\mathcal{R}$ from Figure 42 and the effective potential term is given by:

$$\Omega(x, y, z) = \frac{1}{2}(x^2 + y^2) + \frac{1-\mu}{r_1} + \frac{\mu}{r_2}, \tag{8}$$

$$r_1 = \sqrt{(\mu + x)^2 + y^2 + z^2}\,, \tag{9}$$

$$r_2 = \sqrt{(1 - \mu - x)^2 + y^2 + z^2}\,. \tag{10}$$

We include the effects of solar radiation pressure, which is expected to be the largest perturbing term on the starshade, as:

$$\mathbf{f}_{SRP} = 2PA\cos\alpha\big[b_1\hat{\mathbf{p}}_1 + (b_2\cos\alpha + b_3)\hat{\mathbf{n}}\big] \tag{11}$$

where b_1, b_2, and b_3 are optical coefficients with values taken from Glassman et al. (2011), and the starsahde normal unit vector is given by:

$$\hat{\mathbf{n}} = \cos\alpha\hat{\mathbf{p}}_1 + \sin\alpha\cos\delta\hat{\mathbf{p}}_2 + \sin\alpha\sin\delta\hat{\mathbf{p}}_3\,. \tag{12}$$

The pitch and clock angles α and δ are defined as spherical angles with respect to the starsahde-fixed reference frame, $\mathcal{P}$, shown in Figure 46, whose unit vectors are defined as:

$$\hat{\mathbf{p}}_1 = \frac{\mathbf{r}_1}{|\mathbf{r}_1|}, \quad \hat{\mathbf{p}}_2 = \frac{\hat{\mathbf{z}} \times \hat{\mathbf{p}}_1}{|\hat{\mathbf{z}} \times \hat{\mathbf{p}}_1|}, \quad \hat{\mathbf{p}}_3 = \hat{\mathbf{p}}_1 \times \hat{\mathbf{p}}_2\,. \tag{13}$$

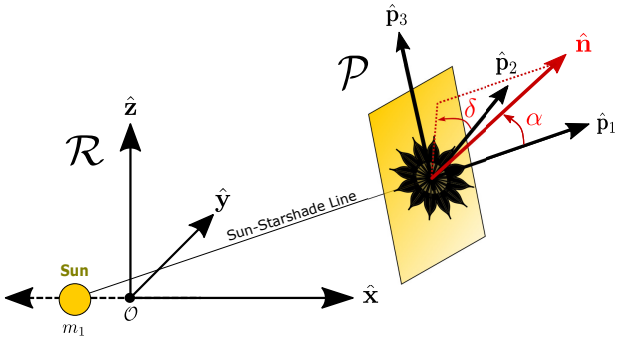

FIGURE 46. *Diagram of the $\mathcal{R}$ and $\mathcal{P}$ frames used in the starshade equations of motion. The $\mathcal{P}$-frame is defined perpendicular to the Sun-Starshade vector. Based on Dachwald et al. (2006). From Soto et al. (2019)*

The starshade positions are well defined at the endpoints of the retargeting trajectory but the corresponding velocities are not. This boundary value problem (BVP) is solved using Equations (5-7) using a collocation algorithm (for further details see Kolemen and Kasdin (2012) and Soto et al. (2018)). The final continuous trajectory from a position along the telescope line of sight (LOS) to star i to one along the LOS of star j is shown in Figure 47. Solutions to the BVP set the velocities at the start

and end of the slew, $\mathbf{v}_{RT}(t_i)$ and $\mathbf{v}_{RT}(t_j)$ respectively, allowing for a Δv and fuel use to be computed.

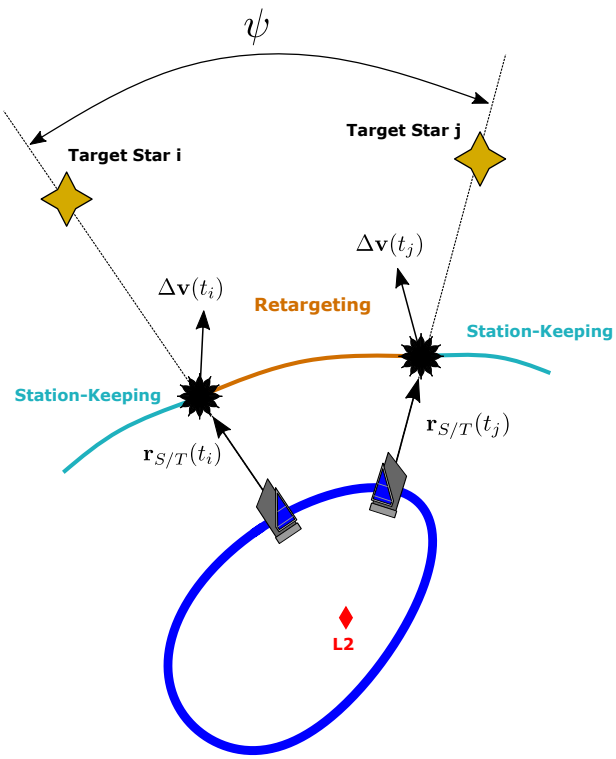

Figure 47. *Schematic of the two starshade flight modes: station-keeping with star i, retargeting to a star j, and station-keeping with star j. An angle ψ separates the LOS vectors to the two stars. From Soto et al. (2019).*

Currently, retargeting slews are modeled as strictly impulsive, meaning that total retargeting Δvs are given simply by the difference in the endpoint velocities provided by the BVP solution and the required stationkeeping velocities at those points (which must match the observatories rotation rates to maintain pointing on the target star. Fuel use is then calculated directly from the Δv via the Tsiolkovsky rocket equation. While future work includes incorporation of complete modelling for continuous-thrust slewing, in terms of fuel use, the current implementation can be viewed as a lower bound for a given system's thrust and specific impulse.

As a final step, we wish to parametrize all slews as a function of the slew time, Δt, and the angle between targets i and j, which is given by:

$$\psi = \mathrm{sgn}(\hat{\mathbf{r}}_{j/0} \cdot \hat{\mathbf{k}}) \arccos(\hat{\mathbf{r}}_{i/0} \cdot \hat{\mathbf{r}}_{j/0}) . \quad (14)$$

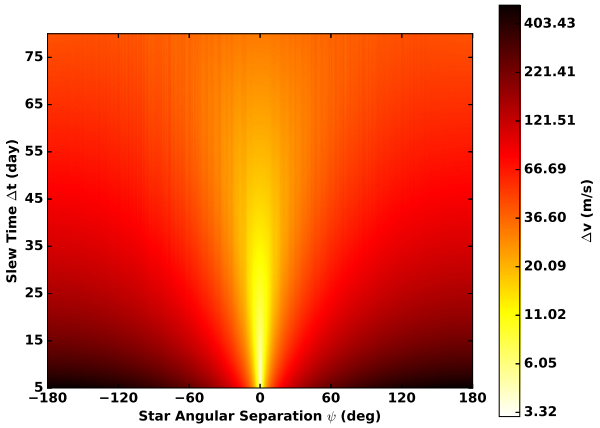

Figure 48. *Heatmap of Δv as a function of both star angular separation ψ and slew time Δt. Interpolated values are shown. Colorbar is shown in log-scale. From Soto et al. (2019).*

For a given starshade propulsion system, we generate a 2-dimensional map of fuel use as a function of transfer time and slew angle. Figure 48 shows an example of one such map, generated at a specific t_0 relative to a single reference star. From the map, it is clear that the relationship between the two parameters is nonlinear. At small values of ψ, fuel costs increase with slew time: quick flights at short distances require less fuel. At large ψ values, fuel costs decrease with slew time: traversing large distances is easier with longer flights. Basing this map on a single slew start time and with respect to a particular originating star introduces errors when this map is used to interpolate fuel use values for other slews. However, extensive characterization of the interpolants based on such maps demonstrates that the mean errors are all within 10%, and in most cases the interpolant yields values within 5% of the true solution, making this an excellent approximation for slew fuel use.

Appendix B. Table of selected target stars used in the discussed scenarios

In Table 8 we list the nearby target stars and mean integration times for exo-Earth detection and characterization for the nominal baseline HabEx 4H hybrid (starshade and coronagraph) case with EXOSIMS using yield metric C1, the metric used in the HabEx Final Report. The columns include (1) the Hipparcos ID (with component ID if system

is multiple), (2) the stellar bolometric luminosity in solar units, (3) distance in pc, (4) mean detection integration time in days, (5) mean number of exo-Earths detected, (6) mean characterization integration time in days, and (7) the mean number of exo-Earths characterized.

The AYO target list is available in the Habex Final report *Appendix D*.

In Table 9 we list the nearby target stars and mean integration times for exo-Earth detection and characterization for the nominal baseline LUVOIR B case with EXOSIMS using yield metric A, the metric used in the LUVOIR Final Report. The columns are the same as in Table 8.

Appendix C. Origins Space Telescope

In addition to LUVOIR and HabEx, the Origins Space Telescope (OST) is a third Large Mission Study that aims to characterize exoplanets. Origins will not search for planets via direct imaging like LUVOIR and HabEx, but instead it will characterize previously known transiting planets through transit spectroscopy in the mid-IR ∼3-20 μm. By achieving a precision of 5 ppm, the Origins final report https://asd.gsfc.nasa.gov/firs/docs/OriginsVolume1MissionConceptStudyReport.pdf notes the potential of detecting biosignatures from transit spectroscopy of terrestrial planets in the habitable zone around nearby mid-to-late M dwarfs. Since potential targets will already have been identified by ongoing transit surveys, especially TESS (Barclay, Pepper, and Quintana, 2018) and SPECULOOS (Delrez et al., 2018), there is no exoplanet discovery phase in the planned Origins Design Reference Mission. Furthermore, habitable zone planet yields around M dwarfs are relatively well constrained from Kepler data (e.g. Dressing and Charbonneau 2015) and will not be the limiting factor for Origins to achieve its exoplanet science goals. Since planet yield is not a pivotal metric when evaluating the proposed Origins mission, this report does not attempt to compare Origins to LUVOIR and HabEx by this metric. Full details on the transit spectroscopy science case with Origins, including predicted number of targets and simulated spectral retrievals, are available in the Origins final report.

Table 8. *HabEx 4H Hybrid, Metric C1, Target Star Data and Mean Detection and Characterization Times*

Target	L ($L_\odot$)	Distance (pc)	Mean Detection Int. Time	Mean # Earths Detected	Mean Characterization Int. Time	Mean # Earths Characterized
HIP 71683	1.61	1.34	0.82	0.11	2.17	0.25
HIP 108870	0.23	3.62	0.97	0.22	1.14	0.22
HIP 71681	0.52	1.34	0.09	0.18	0.42	0.20
HIP 3821 A	1.31	5.94	1.51	0.18	1.09	0.16
HIP 104214	0.13	3.50	0.33	0.15	0.49	0.15
HIP 12114	0.29	7.18	2.35	0.15	1.30	0.14
HIP 99461	0.28	6.01	2.37	0.16	0.96	0.14
HIP 8102	0.52	3.65	0.36	0.14	0.72	0.14
HIP 19849	0.42	4.98	1.42	0.16	0.54	0.13
HIP 37279	7.12	3.51	0.06	0.06	0.22	0.13
HIP 88601 A	0.68	5.10	2.17	0.15	0.98	0.12
HIP 15510	0.69	6.04	1.98	0.15	1.00	0.12
HIP 15457	0.88	9.14	2.56	0.13	1.78	0.11
HIP 7981	0.47	7.53	2.94	0.14	1.16	0.11
HIP 56997	0.65	9.61	3.07	0.13	1.61	0.11
HIP 96100	0.44	5.75	3.27	0.15	1.03	0.11
HIP 8362	0.55	10.07	3.97	0.11	2.36	0.10
HIP 99240	1.33	6.11	1.99	0.14	0.51	0.10
HIP 99825	0.42	8.91	4.13	0.13	1.28	0.10
HIP 3765	0.30	7.45	2.20	0.11	1.22	0.10
HIP 10644	1.21	10.78	4.41	0.15	1.77	0.10
HIP 13402	0.42	10.35	6.72	0.15	2.57	0.10
HIP 84720 A	0.52	8.80	3.19	0.11	1.40	0.10
HIP 105858	1.54	9.26	2.04	0.13	1.65	0.10
HIP 114622	0.31	6.54	1.64	0.10	0.82	0.10
HIP 27072	2.51	8.93	2.09	0.13	1.28	0.09
HIP 47080	0.85	11.37	6.79	0.14	1.89	0.09
HIP 64394	1.48	9.13	1.94	0.12	1.35	0.09
HIP 64924	0.87	8.56	2.34	0.11	1.55	0.09
HIP 23693	1.54	11.65	3.83	0.12	1.83	0.09
HIP 1599	1.33	8.59	2.36	0.12	1.11	0.09
HIP 29271	0.91	10.20	3.52	0.11	2.06	0.08
HIP 15371	1.03	12.03	5.85	0.13	2.16	0.08
HIP 57443	0.86	9.22	2.59	0.09	1.37	0.08
HIP 81300	0.47	9.75	3.89	0.10	1.17	0.08
HIP 80686	1.41	12.12	5.04	0.11	2.19	0.08
HIP 61317	1.27	8.44	1.97	0.09	0.95	0.07
HIP 15330	0.80	12.01	5.44	0.09	1.81	0.07
HIP 56452	0.62	9.56	6.98	0.11	1.63	0.06
HIP 84862	1.30	14.33	8.85	0.11	1.75	0.05
HIP 22263	1.01	13.28	8.02	0.07	1.46	0.04
HIP 22449	3.00	8.07	1.14	0.10	0.42	0.04
HIP 40693	0.63	12.49	10.34	0.12	1.22	0.04
HIP 42438	1.03	14.36	11.55	0.10	1.63	0.04
HIP 72848	0.54	11.51	7.59	0.08	1.48	0.04
HIP 12777	2.42	11.13	3.88	0.10	0.66	0.04
HIP 77257	2.22	12.12	6.49	0.10	0.71	0.04

Target	L ($L_\odot$)	Distance (pc)	Mean Detection Int. Time	Mean # Earths Detected	Mean Characterization Int. Time	Mean # Earths Characterized
HIP 80337	1.03	12.78	7.61	0.08	0.93	0.04
HIP 14632	2.36	10.54	3.85	0.08	0.57	0.03
HIP 51459	1.68	12.78	12.94	0.09	0.89	0.03
HIP 75181	1.09	14.81	13.65	0.12	1.13	0.03
HIP 43587	0.66	12.34	14.49	0.15	0.82	0.03
HIP 79672	1.11	13.90	12.09	0.11	0.83	0.03
HIP 107649	1.35	15.99	13.77	0.07	0.63	0.02
HIP 2021	3.70	7.46	0.60	0.06	0.07	0.02
HIP 3583	0.98	15.16	14.32	0.08	0.96	0.02
HIP 27435	0.85	15.18	16.21	0.08	0.70	0.02
HIP 34065	1.45	16.52	13.21	0.06	0.74	0.02
HIP 98767	1.20	15.86	14.94	0.06	0.60	0.01
HIP 17378	3.37	9.04	1.75	0.07	0.06	0.01
HIP 24813	1.89	12.63	11.25	0.07	0.15	0.01
HIP 38908	1.36	16.20	11.46	0.05	0.34	0.01
HIP 62207	1.12	17.38	22.21	0.10	0.48	0.01
HIP 78072	3.13	11.25	2.38	0.06	0.11	0.01
HIP 100017	1.18	17.57	19.11	0.06	0.36	0.01
HIP 35136	1.54	16.89	15.71	0.05	0.25	0.01
HIP 113357	1.45	15.61	12.80	0.06	0.17	0.01
HIP 5862	2.07	15.11	12.50	0.04	0.09	0.00
HIP 12653	1.78	17.17	3.06	0.01	0.05	0.00
HIP 19076	1.12	16.94	26.22	0.05	0.11	0.00
HIP 47592	2.11	15.01	11.06	0.04	0.06	0.00
HIP 57757	3.79	10.93	1.81	0.05	0.03	0.00
HIP 77358	0.87	15.35	20.00	0.10	0.08	0.00
HIP 95447	1.84	15.18	9.63	0.01	0.04	0.00
HIP 109176	3.63	11.73	1.99	0.05	0.02	0.00

Table 9. *LUVOIR B, Metric A (Water line), Target Star Data and Mean Detection and Characterization Times*

Target	L ($L_\odot$)	Distance (pc)	Mean Detection Int. Time	Mean # Earths Detected	Mean Characterization Int. Time	Mean # Earths Characterized
HIP 113576	0.10	8.22	1.23	0.00	14.12	0.37
HIP 12114	0.29	7.18	0.13	0.00	3.98	0.33
HIP 51459	1.68	12.78	0.00	0.00	5.65	0.30
HIP 72659 A	0.65	6.78	0.09	0.00	1.45	0.30
HIP 7981	0.47	7.53	0.11	0.00	0.72	0.28
HIP 27072	2.51	8.93	0.00	0.00	2.70	0.28
HIP 61317	1.27	8.44	0.12	0.00	2.66	0.28
HIP 105858	1.54	9.26	0.17	0.00	3.01	0.28
HIP 64924	0.87	8.56	0.16	0.00	2.48	0.26
HIP 88601 A	0.68	5.10	0.05	0.00	1.92	0.26
HIP 96100	0.44	5.75	0.03	0.00	0.53	0.26
HIP 3821 A	1.31	5.94	0.05	0.00	3.15	0.24
HIP 5336	0.46	7.55	0.15	0.00	2.54	0.24

Target	L ($L_\odot$)	Distance (pc)	Mean Detection Int. Time	Mean # Earths Detected	Mean Characterization Int. Time	Mean # Earths Characterized
HIP 19849	0.42	4.98	0.02	0.00	0.19	0.24
HIP 32984	0.24	8.71	0.37	0.00	3.26	0.24
HIP 54035	0.02	2.54	0.02	0.00	0.04	0.24
HIP 57443	0.86	9.22	0.15	0.00	2.62	0.24
HIP 58345	0.25	10.16	0.99	0.00	5.07	0.24
HIP 99240	1.33	6.11	0.07	0.00	0.41	0.24
HIP 104214	0.13	3.50	0.01	0.00	0.12	0.24
HIP 108870	0.23	3.62	0.01	0.00	0.12	0.24
HIP 113283	0.20	7.61	0.23	0.00	2.80	0.24
HIP 113296	0.06	6.83	0.16	0.00	6.05	0.24
HIP 117712	0.39	10.89	0.53	0.00	3.36	0.24
HIP 15457	0.88	9.14	0.18	0.00	2.02	0.22
HIP 15510	0.69	6.04	0.04	0.00	0.49	0.22
HIP 42808	0.32	11.14	0.58	0.00	4.63	0.22
HIP 45343	0.08	6.11	0.52	0.00	0.90	0.22
HIP 56997	0.65	9.61	0.19	0.00	3.25	0.22
HIP 64797 A	0.32	11.07	0.64	0.00	6.67	0.22
HIP 84405 B	0.69	5.95	0.34	0.00	3.93	0.22
HIP 99461	0.28	6.01	0.05	0.00	1.66	0.22
HIP 114046	0.04	3.28	0.07	0.00	0.15	0.22
HIP 1475	0.02	3.57	0.11	0.00	1.27	0.20
HIP 1599	1.33	8.59	0.15	0.00	1.59	0.20
HIP 7751 B	0.34	7.82	0.15	0.00	1.14	0.20
HIP 8362	0.55	10.07	0.25	0.00	2.14	0.20
HIP 12777	2.42	11.13	0.00	0.00	3.45	0.20
HIP 16537	0.35	3.21	0.01	0.00	0.20	0.20
HIP 23311	0.30	8.71	0.32	0.00	3.15	0.20
HIP 24813	1.89	12.63	0.00	0.00	3.05	0.20
HIP 49908	0.11	4.87	0.10	0.00	0.21	0.20
HIP 72848	0.54	11.51	0.45	0.00	3.07	0.20
HIP 81300	0.47	9.75	0.26	0.00	2.62	0.20
HIP 88972	0.36	11.02	0.43	0.00	4.64	0.20
HIP 99701	0.07	6.20	0.79	0.00	2.00	0.20
HIP 439	0.02	4.34	0.29	0.00	4.27	0.17
HIP 2021	3.70	7.46	0.02	0.00	3.23	0.17
HIP 17378	3.37	9.04	0.00	0.00	2.26	0.17
HIP 22263	1.01	13.28	0.57	0.00	2.49	0.17
HIP 25878	0.07	5.68	0.77	0.00	2.11	0.17
HIP 26394	1.64	18.32	0.00	0.00	3.97	0.17
HIP 29295	0.06	5.75	0.83	0.00	3.06	0.17
HIP 32439	1.87	17.87	0.00	0.00	6.44	0.17
HIP 42438	1.03	14.36	0.72	0.00	3.83	0.17
HIP 47080	0.85	11.37	0.44	0.00	0.99	0.17
HIP 56452	0.62	9.56	0.56	0.00	2.85	0.17
HIP 78072	3.13	11.25	0.00	0.00	3.20	0.17
HIP 85235	0.44	12.80	0.59	0.00	3.88	0.17
HIP 85295	0.12	7.70	0.91	0.00	1.31	0.17
HIP 86400	0.34	11.00	0.66	0.00	2.58	0.17
HIP 91768	0.01	3.52	0.03	0.00	2.65	0.17
HIP 94761	0.03	5.85	0.00	0.00	8.29	0.17

Target	L ($L_\odot$)	Distance (pc)	Mean Detection Int. Time	Mean # Earths Detected	Mean Characterization Int. Time	Mean # Earths Characterized
HIP 103096	0.06	7.05	1.11	0.00	4.26	0.17
HIP 104217	0.10	3.50	0.02	0.00	0.06	0.17
HIP 106440	0.03	4.95	0.66	0.00	0.92	0.17
HIP 112447	4.86	16.30	0.00	0.00	4.53	0.17
HIP 114622	0.31	6.54	0.08	0.00	0.41	0.17
HIP 116745	0.24	11.42	0.95	0.00	4.79	0.17
HIP 120005	0.08	6.11	0.56	0.00	1.64	0.17
HIP 3765	0.30	7.45	0.15	0.00	1.56	0.15
HIP 3909	1.85	15.75	0.00	0.00	5.65	0.15
HIP 10138	0.42	10.78	0.34	0.00	1.35	0.15
HIP 10644	1.21	10.78	0.32	0.00	3.61	0.15
HIP 13402	0.42	10.35	0.35	0.00	1.82	0.15
HIP 26779	0.50	12.28	0.71	0.00	2.91	0.15
HIP 69972	0.39	11.80	1.03	0.00	1.88	0.15
HIP 80686	1.41	12.12	0.42	0.00	3.08	0.15
HIP 84720 A	0.52	8.80	0.20	0.00	2.13	0.15
HIP 3583	0.98	15.16	0.83	0.00	2.71	0.13
HIP 7918	1.49	12.74	1.41	0.00	4.55	0.13
HIP 15371	1.03	12.03	0.35	0.00	3.41	0.13
HIP 22449	3.00	8.07	0.09	0.00	0.44	0.13
HIP 24186	0.01	3.91	0.05	0.00	6.48	0.13
HIP 40693	0.63	12.49	0.58	0.00	1.19	0.13
HIP 40843	2.56	18.27	0.00	0.00	3.19	0.13
HIP 48331	0.17	11.16	1.80	0.00	3.71	0.13
HIP 50954	5.62	16.22	0.00	0.00	2.53	0.13
HIP 57939	0.23	9.09	0.24	0.00	1.04	0.13
HIP 59199	4.56	14.94	0.00	0.00	3.92	0.13
HIP 65721	3.17	17.99	0.00	0.00	4.53	0.13
HIP 77257	2.22	12.12	0.00	0.00	1.47	0.13
HIP 77760	3.26	15.89	0.00	0.00	2.60	0.13
HIP 80337	1.03	12.78	0.52	0.00	2.54	0.13
HIP 84478	0.16	5.95	0.15	0.00	0.54	0.13
HIP 85523	0.02	4.54	0.00	0.00	3.58	0.13
HIP 95447	1.84	15.18	0.00	0.00	3.09	0.13
HIP 98698	0.23	12.86	2.41	0.00	3.46	0.13
HIP 99825	0.42	8.91	0.27	0.00	2.24	0.13
HIP 107556	8.38	11.87	0.00	0.00	3.17	0.13
HIP 109176	3.63	11.73	0.00	0.00	1.89	0.13
HIP 544	0.68	13.67	0.91	0.00	2.97	0.11
HIP 910	3.38	18.75	0.00	0.00	3.30	0.11
HIP 8102	0.52	3.65	0.01	0.00	0.25	0.11
HIP 15330	0.80	12.01	0.37	0.00	1.98	0.11
HIP 27887	0.27	13.00	1.41	0.00	3.60	0.11
HIP 29271	0.91	10.20	0.27	0.00	1.11	0.11
HIP 32480	1.95	16.72	0.00	0.00	4.06	0.11
HIP 43587	0.66	12.34	0.89	0.00	3.66	0.11
HIP 57757	3.79	10.93	0.00	0.00	1.40	0.11
HIP 58576	0.93	12.76	1.35	0.00	3.21	0.11
HIP 64792	2.29	17.56	0.00	0.00	3.96	0.11
HIP 67155	0.04	5.41	0.87	0.00	2.26	0.11

Target	L ($L_\odot$)	Distance (pc)	Mean Detection Int. Time	Mean # Earths Detected	Mean Characterization Int. Time	Mean # Earths Characterized
HIP 68184	0.33	10.06	0.54	0.00	0.73	0.11
HIP 71181	0.27	13.22	2.04	0.00	4.12	0.11
HIP 71284	3.42	15.83	0.00	0.00	3.88	0.11
HIP 76829	3.58	17.44	0.00	0.00	4.58	0.11
HIP 86162	0.02	4.54	0.16	0.00	4.69	0.11
HIP 86796	2.01	15.51	0.00	0.00	1.57	0.11
HIP 95319	0.70	15.76	1.65	0.00	3.80	0.11
HIP 98767	1.20	15.86	1.27	0.00	2.16	0.11
HIP 98819	1.35	17.77	1.65	0.00	3.35	0.11
HIP 109422	3.04	18.28	0.00	0.00	4.40	0.11
HIP 116085	0.58	16.93	2.22	0.00	4.99	0.11
HIP 117473	0.03	5.95	0.00	0.00	3.23	0.11
HIP 4151	3.66	18.74	0.00	0.00	3.32	0.09
HIP 5862	2.07	15.11	0.00	0.00	2.19	0.09
HIP 7978	1.64	17.43	0.00	0.00	2.56	0.09
HIP 12653	1.78	17.17	0.00	0.00	3.93	0.09
HIP 14632	2.36	10.54	0.00	0.00	0.85	0.09
HIP 16852	3.29	13.96	0.00	0.00	1.45	0.09
HIP 28103	6.02	14.88	0.00	0.00	3.37	0.09
HIP 33817	0.47	14.65	1.63	0.00	2.98	0.09
HIP 38908	1.36	16.20	1.07	0.00	2.29	0.09
HIP 45333	2.87	19.57	0.00	0.00	4.25	0.09
HIP 53721	1.71	14.06	0.00	0.00	2.93	0.09
HIP 64394	1.48	9.13	0.20	0.00	0.40	0.09
HIP 67275	3.35	15.62	0.00	0.00	2.30	0.09
HIP 71681	0.52	1.34	0.00	0.00	0.00	0.09
HIP 77801	1.00	17.35	1.23	0.00	2.29	0.09
HIP 79248	0.70	17.57	2.56	0.00	3.69	0.09
HIP 88694	1.15	17.55	1.90	0.00	2.45	0.09
HIP 89042	1.78	17.61	0.00	0.00	3.00	0.09
HIP 90790	0.35	13.25	1.45	0.00	2.92	0.09
HIP 97944	0.80	14.05	2.32	0.00	2.24	0.09
HIP 100017	1.18	17.57	1.39	0.00	2.67	0.09
HIP 105090	0.08	3.95	0.08	0.00	0.48	0.09
HIP 107350	1.18	17.89	1.93	0.00	3.66	0.09
HIP 113357	1.45	15.61	1.20	0.00	1.98	0.09
HIP 1292	0.67	17.50	2.31	0.00	4.88	0.07
HIP 7513	3.64	13.49	0.00	0.00	0.65	0.07
HIP 17651	5.39	17.63	0.00	0.00	1.79	0.07
HIP 18859	2.17	18.83	0.00	0.00	2.37	0.07
HIP 19076	1.12	16.94	1.99	0.00	2.31	0.07
HIP 19893	6.90	20.46	0.00	0.00	3.08	0.07
HIP 23693	1.54	11.65	0.40	0.00	1.11	0.07
HIP 27435	0.85	15.18	1.04	0.00	1.59	0.07
HIP 29525	0.79	17.95	2.49	0.00	3.19	0.07
HIP 34017	1.37	19.13	1.96	0.00	3.23	0.07
HIP 41926	0.41	12.21	0.62	0.00	1.32	0.07
HIP 43726	1.09	17.39	2.11	0.00	2.36	0.07
HIP 45038 A	4.33	20.38	0.00	0.00	2.03	0.07
HIP 46853	8.45	13.48	0.00	0.00	1.35	0.07

Target	L ($L_\odot$)	Distance (pc)	Mean Detection Int. Time	Mean # Earths Detected	Mean Characterization Int. Time	Mean # Earths Characterized
HIP 48113	2.78	18.37	0.00	0.00	1.64	0.07
HIP 49081	1.47	15.05	1.37	0.00	1.72	0.07
HIP 57507	0.73	17.47	1.88	0.00	3.16	0.07
HIP 58910	0.03	5.52	0.09	0.00	5.64	0.07
HIP 61291	0.38	16.18	2.08	0.00	2.83	0.07
HIP 70319	0.86	17.19	2.01	0.00	2.60	0.07
HIP 70497	4.42	14.53	0.00	0.00	0.63	0.07
HIP 77358	0.87	15.35	1.46	0.00	3.32	0.07
HIP 78775	0.46	14.52	1.20	0.00	2.45	0.07
HIP 79672	1.11	13.90	0.95	0.00	0.93	0.07
HIP 79755	0.10	10.69	0.00	0.00	3.19	0.07
HIP 82860	2.26	15.26	0.00	0.00	2.28	0.07
HIP 83591	0.16	10.71	1.88	0.00	2.93	0.07
HIP 84862	1.30	14.33	0.76	0.00	1.62	0.07
HIP 96441	4.51	18.34	0.00	0.00	2.38	0.07
HIP 98036	6.29	13.70	0.00	0.00	0.47	0.07
HIP 101997	0.56	14.38	1.45	0.00	2.37	0.07
HIP 107649	1.35	15.99	1.29	0.00	1.74	0.07
HIP 116771	3.70	13.71	0.00	0.00	1.71	0.07
HIP 4148	0.31	14.17	2.09	0.00	1.44	0.04
HIP 10798	0.45	12.67	0.64	0.00	1.14	0.04
HIP 14879 A	5.30	14.24	0.00	0.00	1.10	0.04
HIP 19921	6.88	18.24	0.00	0.00	0.43	0.04
HIP 25110	3.45	20.89	0.00	0.00	2.04	0.04
HIP 25278	1.80	14.39	0.00	0.00	1.74	0.04
HIP 29650	3.05	20.82	0.00	0.00	1.90	0.04
HIP 32765	4.80	25.26	0.00	0.00	2.01	0.04
HIP 34065	1.45	16.52	1.29	0.00	1.35	0.04
HIP 36366	5.84	18.05	0.00	0.00	1.14	0.04
HIP 47592	2.11	15.01	0.00	0.00	0.93	0.04
HIP 51523	4.54	21.81	0.00	0.00	1.69	0.04
HIP 54211	0.02	4.86	0.23	0.00	1.34	0.04
HIP 66765	0.43	15.65	2.20	0.00	2.28	0.04
HIP 74975	5.34	25.38	0.00	0.00	1.89	0.04
HIP 75181	1.09	14.81	1.02	0.00	0.93	0.04
HIP 76074	0.03	5.93	0.00	0.00	6.19	0.04
HIP 79190	0.33	14.67	2.11	0.00	1.71	0.04
HIP 79607 A	2.19	21.08	0.00	0.00	2.58	0.04
HIP 93858	0.94	16.95	2.03	0.00	1.25	0.04
HIP 96895	1.70	21.08	0.00	0.00	1.98	0.04
HIP 97675	2.88	19.19	0.00	0.00	1.45	0.04
HIP 98921	1.08	18.79	1.96	0.00	1.82	0.04
HIP 102485	4.06	14.68	0.00	0.00	0.78	0.04
HIP 110109	1.23	13.79	1.35	0.00	1.15	0.04
HIP 110649	2.91	20.56	0.00	0.00	1.04	0.04
HIP 950	3.07	21.28	0.00	0.00	1.64	0.02
HIP 3497	1.07	22.06	2.47	0.00	1.00	0.02
HIP 3810	4.49	23.45	0.00	0.00	0.75	0.02
HIP 12444	1.97	21.76	0.00	0.00	1.23	0.02
HIP 12843	2.83	14.22	0.00	0.00	0.09	0.02

Target	L ($L_\odot$)	Distance (pc)	Mean Detection Int. Time	Mean # Earths Detected	Mean Characterization Int. Time	Mean # Earths Characterized
HIP 14954	4.23	22.58	0.00	0.00	0.93	0.02
HIP 15799	0.56	17.42	2.64	0.00	2.37	0.02
HIP 17420	0.31	13.95	2.06	0.00	0.58	0.02
HIP 20917	0.13	11.39	0.00	0.00	1.84	0.02
HIP 21553	0.08	10.11	0.00	0.00	1.55	0.02
HIP 29860	1.73	19.25	0.00	0.00	1.00	0.02
HIP 33277	1.32	17.24	2.24	0.00	0.87	0.02
HIP 35136	1.54	16.89	1.66	0.00	0.42	0.02
HIP 37349	0.31	14.21	2.14	0.00	0.67	0.02
HIP 38423 A	2.63	17.94	0.00	0.00	0.91	0.02
HIP 39157	0.45	16.77	2.43	0.00	1.29	0.02
HIP 39903	4.29	19.98	0.00	0.00	0.89	0.02
HIP 40702	7.74	19.56	0.00	0.00	0.94	0.02
HIP 44897	1.38	19.19	2.50	0.00	0.93	0.02
HIP 46509	3.72	17.33	0.00	0.00	1.27	0.02
HIP 46580	0.27	12.91	2.08	0.00	0.70	0.02
HIP 51502	3.08	21.50	0.00	0.00	1.13	0.02
HIP 54646	0.13	11.87	0.00	0.00	2.58	0.02
HIP 54745	1.17	21.93	2.04	0.00	1.03	0.02
HIP 54952 A	0.23	14.65	0.05	0.00	1.01	0.02
HIP 55779	5.46	27.22	0.00	0.00	1.24	0.02
HIP 61174	5.24	18.28	0.00	0.00	0.62	0.02
HIP 62145	0.38	14.88	2.76	0.00	1.07	0.02
HIP 62207	1.12	17.38	1.64	0.00	0.98	0.02
HIP 62523	0.81	16.93	1.92	0.00	0.55	0.02
HIP 64408	4.48	20.67	0.00	0.00	0.32	0.02
HIP 64583	3.13	18.20	0.00	0.00	0.71	0.02
HIP 65859	0.04	7.66	0.00	0.00	0.97	0.02
HIP 67153	6.36	19.40	0.00	0.00	0.61	0.02
HIP 69965	1.27	18.03	1.78	0.00	1.26	0.02
HIP 69989	3.93	26.10	0.00	0.00	1.24	0.02
HIP 70873	1.48	23.74	0.00	0.00	1.28	0.02
HIP 73996	4.42	19.55	0.00	0.00	1.06	0.02
HIP 78459	1.83	17.24	0.00	0.00	0.41	0.02
HIP 82003	0.11	9.81	1.04	0.00	0.73	0.02
HIP 82020	6.60	26.11	0.00	0.00	2.44	0.02
HIP 82588	0.63	17.25	2.67	0.00	1.17	0.02
HIP 83541	0.72	17.84	3.01	0.00	0.90	0.02
HIP 83990	0.23	13.62	1.91	0.00	1.15	0.02
HIP 84893	4.42	17.36	0.00	0.00	0.53	0.02
HIP 88745 A	2.05	15.64	0.00	0.00	1.03	0.02
HIP 93966	1.58	21.43	0.18	0.00	1.07	0.02
HIP 98959	1.06	17.73	1.59	0.00	1.22	0.02
HIP 100925	0.81	19.52	2.89	0.00	0.87	0.02
HIP 102333	7.61	24.17	0.00	0.00	0.89	0.02
HIP 103389	2.21	21.97	0.00	0.00	1.24	0.02
HIP 106696	0.32	14.62	2.07	0.00	0.55	0.02
HIP 111960	0.20	13.55	0.00	0.00	1.12	0.02
HIP 114948	2.00	20.54	0.00	0.00	0.42	0.02

Appendix D. References

[1] Thomas Barclay, Joshua Pepper, and Elisa V. Quintana. "A Revised Exoplanet Yield from the Transiting Exoplanet Survey Satellite (TESS)". Astrophys. J. Supp. 239.1, 2 (2018), p. 2. DOI: 10.3847/1538-4365/aae3e9. arXiv: 1804.05050 [astro-ph.EP].

[2] Natasha E. Batalha, Mark S. Marley, Nikole K. Lewis, and Jonathan J. Fortney. "Exoplanet Reflected-light Spectroscopy with PICASO". *The Astrophysical Journal* 878.1, 70 (June 2019), p. 70. DOI: 10.3847/1538-4357/ab1b51. arXiv: 1904.09355 [astro-ph.EP].

[3] Ruslan Belikov, Christopher Stark, Natalie Batalha, Chris Burke, and SAG13. *Exoplanet Occurence Rates and Distributions - Closeout*. 2016. URL: https://exoplanets.nasa.gov/system/presentations/files/67_Belikov_SAG13_ExoPAG16_draft_v4.pdf.

[4] Ruslan Belikov, Eugene Pluzhnik, Eduardo Bendek, and Dan Sirbu. "High-contrast imaging in multi-star systems: progress in technology development and lab results". *Techniques and Instrumentation for Detection of Exoplanets VIII*. Vol. 10400. International Society for Optics and Photonics. 2017, 104000W.

[5] Sarah Blunt, Eric L. Nielsen, Robert J. De Rosa, Quinn M. Konopacky, Dominic Ryan, Jason J. Wang, Laurent Pueyo, Julien Rameau, Christian Marois, and Franck Marchis. "Orbits for the Impatient: A Bayesian Rejection-sampling Method for Quickly Fitting the Orbits of Long-period Exoplanets". *The Astronomical Journal* 153.5, 229 (May 2017), p. 229. DOI: 10.3847/1538-3881/aa6930. arXiv: 1703.10653 [astro-ph.EP].

[6] R. A. Brown. "Obscurational completeness". *The Astrophysical Journal* 607 (2004), pp. 1003–1017.

[7] R. A. Brown. "Single-visit photometric and obscurational completeness". *The Astrophysical Journal* 624 (2005), pp. 1010–1024.

[8] R.A. Brown and R. Soummer. "New Completeness Methods for Estimating Exoplanet Discoveries by Direct Detection". *The Astrophysical Journal* 715 (2010), p. 122.

[9] Marta L Bryan, Heather A Knutson, Andrew W Howard, Henry Ngo, Konstantin Batygin, Justin R Crepp, BJ Fulton, Sasha Hinkley, Howard Isaacson, John A Johnson, et al. "Statistics of Long Period Gas Giant Planets in Known Planetary Systems". *The Astrophysical Journal* 821.2 (2016), p. 89.

[10] Christopher J Burke, Jessie L Christiansen, F Mullally, Shawn Seader, Daniel Huber, Jason F Rowe, Jeffrey L Coughlin, Susan E Thompson, Joseph Catanzarite, Bruce D Clarke, et al. "Terrestrial planet occurrence rates for the Kepler GK dwarf sample". *The Astrophysical Journal* 809.1 (2015), p. 8.

[11] J. Chen and D. Kipping. "Probabilistic Forecasting of the Masses and Radii of Other Worlds". Astrophys. J. 834, 17 (Jan. 2017), p. 17. DOI: 10.3847/1538-4357/834/1/17. arXiv: 1603.08614 [astro-ph.EP].

[12] Jingjing Chen and David M Kipping. "Probabilistic Forecasting of the Masses and Radii of Other Worlds". *arXiv preprint arXiv:1603.08614* (2016).

[13] A. Cumming, R. P. Butler, G. W. Marcy, S. S. Vogt, J. T. Wright, and D. A. Fischer. "The Keck planet search: detectability and the minimum mass and orbital period distribution of extrasolar planets". *Publications of the Astronomical Society of the Pacific* 120 (2008), pp. 531–554.

[14] Bernd Dachwald, Giovanni Mengali, Alessandro A. Quarta, and Malcolm Macdonald. "Parametric Model and Optimal Control of Solar Sails with Optical Degradation". *Journal of Guidance, Control, and Dynamics* 29.5 (2006), pp. 1170–1178. URL: https://doi.org/10.2514/1.20313.

[15] D. Defrère, P. M. Hinz, B. Mennesson, W. F. Hoffmann, R. Millan-Gabet, A. J. Skemer, V. Bailey, W. C. Danchi, E. C. Downey, O. Durney, P. Grenz, J. M. Hill, T. J. McMahon, M. Montoya, E. Spalding, A. Vaz, O. Absil, P. Arbo, H. Bailey, G. Brusa, G. Bryden, S. Esposito, A. Gaspar, C. A. Haniff, G. M. Kennedy, J. M. Leisenring, L. Marion, M. Nowak, E. Pinna, K. Powell, A. Puglisi, G. Rieke, A. Roberge, E. Serabyn, R. Sosa, K. Stapeldfeldt, K. Su, A. J. Weinberger, and M. C. Wyatt. "Nulling Data Reduction and On-sky Performance of the Large Binocular Telescope Interferometer". Astrophys. J. 824, 66 (June 2016), p. 66. DOI: 10.3847/0004-637X/824/2/66. arXiv: 1601.06866 [astro-ph.EP].

[16] Laetitia Delrez, Michaël. Gillon, Didier Queloz, Brice-Olivier Demory, Yaseen Almleaky, Julien de Wit, Emmanuël. Jehin, Amaury H. M. J. Triaud, Khalid Barkaoui, Artem Burdanov, Adam J. Burgasser, Elsa Ducrot, James McCormac, Catriona Murray, Catarina Silva Fernandes, Sandrine Sohy, Samantha J. Thompson, Valérie Van Grootel, Roi Alonso, Zouhair Benkhaldoun, and Rafael Rebolo.

"SPECULOOS: a network of robotic telescopes to hunt for terrestrial planets around the nearest ultracool dwarfs". Proc. SPIE. Vol. 10700. Society of Photo-Optical Instrumentation Engineers (SPIE) Conference Series. 2018, p. 107001I. DOI: 10.1117/12.2312475. arXiv: 1806.11205 [astro-ph.IM].

[17] Courtney D Dressing and David Charbonneau. "The occurrence of potentially habitable planets orbiting M dwarfs estimated from the full Kepler dataset and an empirical measurement of the detection sensitivity". *The Astrophysical Journal* 807.1 (2015), p. 45.

[18] S. Dulz, P. Plavchan, J. R. Crepp, C. Stark, R. Morgan, S. Kane, P. Newman, W. Matzko, and G. Mulders. "Joint Radial Velocity and Direct Imaging Planet Yield Calculations: I. Self-consistent Planet Population Demographics" (2019). In preparation.

[19] Ertal2018Report. *Report on HOSTS survey return*. http://nexsci.caltech.edu/missions/LBTI/report_hosts_dec2018_v1.2.pdf. 2018.

[20] S. Ertel, D. Defrère, P. Hinz, B. Mennesson, G. M. Kennedy, W. C. Danchi, C. Gelino, J. M. Hill, W. F. Hoffmann, G. Rieke, A. Shannon, E. Spalding, J. M. Stone, A. Vaz, A. J. Weinberger, P. Willems, O. Absil, P. Arbo, V. P. Bailey, C. Beichman, G. Bryden, E. C. Downey, O. Durney, S. Esposito, A. Gaspar, P. Grenz, C. A. Haniff, J. M. Leisenring, L. Marion, T. J. McMahon, R. Millan-Gabet, M. Montoya, K. M. Morzinski, E. Pinna, J. Power, A. Puglisi, A. Roberge, E. Serabyn, A. J. Skemer, K. Stapelfeldt, K. Y. L. Su, V. Vaitheeswaran, and M. C. Wyatt. "The HOSTS Survey—Exozodiacal Dust Measurements for 30 Stars". Astron. J. 155, 194 (May 2018), p. 194. DOI: 10.3847/1538-3881/aab717. arXiv: 1803.11265 [astro-ph.SR].

[21] Rachel B. Fernandes, Gijs D. Mulders, Ilaria Pascucci, Christoph Mordasini, and Alexandre Emsenhuber. "Hints for a Turnover at the Snow Line in the Giant Planet Occurrence Rate". *The Astrophysical Journal* 874.1 (2019), p. 81. DOI: 10.3847/1538-4357/ab0300. URL: https://doi.org/10.3847%2F1538-4357%2Fab0300.

[22] Rachel B. Fernandes, Gijs D. Mulders, Ilaria Pascucci, Christoph Mordasini, and Alexandre Emsenhuber. "Hints for a Turnover at the Snow Line in the Giant Planet Occurrence Rate". *The Astrophysical Journal* 874.1 (2019), p. 81.

[23] T. Glassman, L. Newhart, W. Voshell, A. Lo, and G. Barber. "Creating optimal observing schedules for a starshade planet-finding mission". *Aerospace Conference, 2011 IEEE*. IEEE. 2011, pp. 1–19.

[24] Claire Marie Guimond and Nicolas B Cowan. "The direct imaging search for Earth 2.0: Quantifying biases and planetary false positives". *The Astronomical Journal* 155.6 (2018), p. 230.

[25] T. J. Henry and D. W. McCarthy Jr. "The Mass-Luminosity Relation for stars of mass 1.0 to $0.08 M_{\odot}$". *AJ* 106 (1993), pp. 773–789.

[26] Andrew Horning, Rhonda Morgan, and Eric Nielsen. "Minimum number of observations for exoplanet orbit determination". *Techniques and Instrumentation for Detection of Exoplanets IX*. Vol. 11117. *Proc. SPIE*. International Society for Optics and Photonics. 2019.

[27] Stephen R. Kane, Michelle L. Hill, James F. Kasting, Ravi Kumar Kopparapu, Elisa V. Quintana, Thomas Barclay, Natalie M. Batalha, William J. Borucki, David R. Ciardi, Nader Haghighipour, Natalie R. Hinkel, Lisa Kaltenegger, Franck Selsis, and Guillermo Torres. "A CATALOG OF KEPLER HABITABLE ZONE EXOPLANET CANDIDATES". *Astrophys. J.* 830.1 (2016), p. 1.

[28] G. M. Kennedy and M. C. Wyatt. "The bright end of the exo-Zodi luminosity function: disc evolution and implications for exo-Earth detectability". MNRAS 433 (Aug. 2013), pp. 2334–2356. DOI: 10.1093/mnras/stt900.

[29] D. M. Kipping. "Parametrizing the exoplanet eccentricity distribution with the beta distribution." MNRAS 434 (2013), pp. L51–L55. DOI: 10.1093/mnrasl/slt075. arXiv: 1306.4982 [astro-ph.EP].

[30] Egemen Kolemen and N Jeremy Kasdin. "Optimization of an Occulter-Based Extrasolar-Planet-Imaging Mission". *Journal of Guidance, Control, and Dynamics* 35.1 (2012), pp. 172–185. URL: https://doi.org/10.2514/1.53479.

[31] R. K. Kopparapu, R. Ramirez, J. F. Kasting, V. Eymet, T. D. Robinson, S. Mahadevan, R. C. Terrien, S. Domagal-Goldman, V. Meadows, and R. Deshpande. "Habitable Zones around Main-sequence Stars: New Estimates". Astrophys. J. 765, 131 (Mar. 2013), p. 131. DOI: 10.1088/0004-637X/765/2/131. arXiv: 1301.6674 [astro-ph.EP].

[32] Ravi Kumar Kopparapu, Eric Hébrard, Rus Belikov, Natalie M Batalha, Gijs D Mulders, Chris Stark, Dillon Teal, Shawn Domagal-Goldman, and Avi Mandell. "Exoplanet Classification and Yield Estimates for Direct Imaging Missions". *The Astrophysical Journal* 856.2 (2018), p. 122.

[33] D. Lafreniere, R. Doyon, C. Marois, D. Nadeau, B.R. Oppenheimer, P.F. Roche, F. Rigaut, J.R. Graham, R. Jayawardhana, D. Johnstone, et al. "The Gemini Deep Planet Survey–GDPS". *Arxiv preprint arXiv:0705.4290* (2007).

[34] C. Leinert, S. Bowyer, LK Haikala, MS Hanner, MG Hauser, A.C. Levasseur-Regourd, I. Mann, K. Mattila, WT Reach, W. Schlosser, et al. "The 1997 reference of diffuse night sky brightness". *Astronomy and Astrophysics Supplement Series* 127.1 (1998), pp. 1–99.

[35] Eric Mamajek. *A Modern Mean Dwarf Stellar Color and Effective Temperature Sequence*. http://www.pas.rochester.edu/~emamajek/EEM_dwarf_UBVIJHK_colors_Teff.txt. 2019.

[36] B. Mennesson, R. Millan-Gabet, E. Serabyn, M. M. Colavita, O. Absil, G. Bryden, M. Wyatt, W. Danchi, D. Defrère, O. Doré, P. Hinz, M. Kuchner, S. Ragland, N. Scott, K. Stapelfeldt, W. Traub, and J. Woillez. "Constraining the Exozodiacal Luminosity Function of Main-sequence Stars: Complete Results from the Keck Nuller Mid-infrared Surveys". Astrophys. J. 797, 119 (Dec. 2014), p. 119. DOI: 10.1088/0004-637X/797/2/119.

[37] E. L. Nielsen, L. M. Close, B. A. Biller, E. Masciadri, and R. Lenzen. "Constraints on extrasolar planet populations from VLT NACO/SDI and MMT SDI and direct adaptive optics imaging surveys: giant planets are rare at large separations". *The Astrophysical Journal* 674 (2008), p. 466.

[38] Leslie A Rogers. "Most 1.6 Earth-radius planets are not rocky". *The Astrophysical Journal* 801.1 (2015), p. 41.

[39] D. Savransky, C. Delacroix, and D. Garrett. *EXOSIMS: Exoplanet Open-Source Imaging Mission Simulator*. Astrophysics Source Code Library. June 2017.

[40] D. Savransky, N. J. Kasdin, and E. Cady. "Analyzing the designs of planet finding missions". *Publications of the Astronomical Society of the Pacific* 122.890 (Apr. 2010), pp. 401–419.

[41] Dmitry Savransky, Christian Delacroix, and Daniel Garrett. "Multi-mission modeling for space-based exoplanet imagers". *Society of Photo-Optical Instrumentation Engineers (SPIE) Conference Series*. Vol. 10400. Sept. 2017, p. 104001L.

[42] Dmitry Savransky and Daniel Garrett. "WFIRST-AFTA coronagraph science yield modeling with EXOSIMS". *Journal of Astronomical Telescopes, Instruments, and Systems* 2.1 (2015), p. 011006.

[43] Dan Sirbu, Ruslan Belikov, Eduardo Bendek, Chris Henze, AJ Eldorado Riggs, and Stuart Shaklan. "Multi-star wavefront control for the wide-field infrared survey telescope". *Space Telescopes and Instrumentation 2018: Optical, Infrared, and Millimeter Wave*. Vol. 10698. International Society for Optics and Photonics. 2018, 106982F.

[44] Dan Sirbu, Sandrine Thomas, Ruslan Belikov, and Eduardo Bendek. "Techniques for high-contrast imaging in multi-star systems. II. Multi-star wavefront control". *The Astrophysical Journal* 849.2 (2017), p. 142.

[45] Gabriel J. Soto, Dean Keithly, Daniel Garrett, Christian Delacroix, and Dmitry Savransky. "Optimal starshade observation scheduling". *Space Telescopes and Instrumentation 2018: Optical, Infrared, and Millimeter Wave*. Vol. 10698. International Society for Optics and Photonics. 2018, p. 106984M.

[46] Gabriel J. Soto, Dmitry Savransky, Daniel Garrett, and Christian Delacroix. "Parameterizing the Search Space of Starshade Fuel Costs for Optimal Observation Schedules". *JGCD* (2019).

[47] R. Soummer, L. Pueyo, and J. Larkin. "Detection and Characterization of Exoplanets and Disks using Projections on Karhunen-Loeve Eigenimages". *The Astrophysical Journal Letters* 755.2 (2012), p. L28.

[48] Christopher C. Stark, Eric J. Cady, Mark Clampin, Shawn Domagal-Goldman, Doug Lisman, Avi M. Mandell, Michael W. McElwain, Aki Roberge, Tyler D. Robinson, Dmitry Savransky, Stuart B. Shaklan, and Karl R. Stapelfeldt. "A direct comparison of exoEarth yields for starshades and coronagraphs". *Proc. SPIE*. Vol. 9904. SPIE. 2016, 99041U–99041U–13.

[49] Christopher C. Stark, Rus Belikov, Matthew R Bolcar, Eric Cady, Brendan P Crill, Steve Ertel, Tyler Groff, Sergi Hildebrandt, John Krist, P Douglas Lisman, et al. "ExoEarth yield landscape for future direct imaging space telescopes". *Journal of Astronomical Telescopes, Instruments, and Systems* 5.2 (2019), p. 024009.

[50] Christopher C. Stark, Aki Roberge, Avi Mandell, Mark Clampin, Shawn D Domagal-Goldman, Michael W McElwain, and Karl R Stapelfeldt. "Lower Limits on Aperture Size for an ExoEarth Detecting Coronagraphic Mission". *The Astrophysical Journal* 808.2 (2015), p. 149.

[51] Christopher C. Stark, Stuart Shaklan, Doug Lisman, Eric Cady, Dmitry Savransky, Aki Roberge, and Avi M. Mandell. "Maximized exoEarth candidate yields for starshades". *Journal of Astronomical Telescopes, Instruments, and Systems* 2.4 (2016), p. 041204.

[52] Christopher C. Stark, Aki Roberge, Avi Mandell, and Tyler D Robinson. "Maximizing the ExoEarth Candidate Yield from a Future Direct Imaging Mission". *The Astrophysical Journal* 795.2 (2014), p. 122.

[53] S Thomas, Ruslan Belikov, and Eduardo Bendek. "Techniques for high-contrast imaging in multi-star systems. I. super-nyquist wavefront control". *The Astrophysical Journal* 810.1 (2015), p. 81.

[54] Margaret C Turnbull. "ExoCat-1: The Nearby Stellar Systems Catalog for Exoplanet Imaging Missions". *arXiv preprint arXiv:1510.01731* (2015).

[55] Kevin J. Zahnle and David C. Catling. "The Cosmic Shoreline: The Evidence that Escape Determines which Planets Have Atmospheres, and what this May Mean for Proxima Centauri B". *The Astrophysical Journal* 843.2 (2017), p. 122.